Final Report

Sustainability of Hydraulic Fracture Conductivity in Ductile and Expanding Shales

FWP ESD 14084

Principal Investigator: Seiji Nakagawa, (510) 486-7894, snakagawa@lbl.gov

Co.-PI: Jonny Rutqvist
Tim Kneafsey
Kunhwi Kim
Sharon Borglin
Marco Voltolini
Hele Prieto
Lawrence Berkeley National Laboratory

Submitted to:
U.S. Department of Energy
National Energy Technology Laboratory
DOE Project Manager: Stephen Henry
Phone: (304) 285-2083
Email Stephen.Henry@netl.doe.gov

Table of Contents

List of Figures

List of Tables

1. Executive Summary

Hydraulic fracturing is an indispensable tool for enhancing permeability of otherwise very impermeable shales containing oil and gas. However, clay-rich, ductile shales are difficult to fracture, and the hydraulic fractures created in the rock tend to be short and have a smaller surface area. Also, proppant placed in these fractures tends to be embedded in the soft fracture walls, and the open space created by the fracture can be filled by mobilized clay minerals and by the expanded fracture walls if swelling clays (e.g., smectites, mixed-layer illites) are present in the rock. The primary goals of this research project are to investigate and understand (1) how hydraulic fractures produced in ductile shale behave over time to reduce in aperture and permeability, (2) how the proppant deposition characteristics (e.g., monolayer vs multilayer), grain size, and spatial distribution (isolated patches vs. connected strings and networks) affect the sustainability of the fracture conductivity impacted by fracture aperture reduction resulting from rock deformation and clay mobilization, and (3) how the near-fracture shale-matrix fluid transport is affected by the evolving conductivity of the fracture.

To meet these objectives, we conducted core-scale laboratory experiments under controlled temperature and stress, using several available natural shale samples with different ductility and clay compositions. These experiments include baseline shale property characterization, micro-indentation tests, and optical (and some X-ray CT) visualization of shale fracture compaction, with and without proppants. Concurrently, numerical modeling of shale deformation and fracturing were performed, and prediction accuracy checked against the laboratory experiments. The modeling employed either a discrete modeling method (TOUGH-RBSN) or a continuum modeling method (TOUGH-FLAC), depending upon the laboratory experiment being modeled and the involved physical processes.

This 2-year-long project produced new laboratory tools for investigating time-dependent deformation of shale fractures with and without proppant. An in-house instrumented indentation test system was developed for single-proppant-scale study of shale mechanical properties including short-duration visco-elastic deformation. A core-scale in-situ optical visualization test system was developed for studying long-duration (weeks to a month) shale fracture closure and proppant embedment, with concurrent direct deformation and hydrological (permeability) measurements. A new visualization technique using UV-induced fluorescence was developed, which allowed us to obtain (quasi-) 3D images of fracture aperture distribution and proppant crushing. Using heavy krypton gas, invasion/migration of gas in partially saturated shale core was imaged using X-ray CT. Continuum-based TOUGH-FLAC was successfully applied to model multi-grain proppant embedment in ductile shale, using a special interface element. The method was also applied to determine failure model parameters (Mohr-Coulomb) of shale from laboratory indentation experiments. Discrete-element-based TOUGH-RBSN was successfully used to examine proppant-shale interaction involving brittle fracturing. Although relative strengths of the shale and the proppant resulted in different fracturing behavior as expected, shale matrix failure always seemed to occur regardless of the proppant strength, possibly because of small tensile strength of rock compared to proppant grains.

In this final report, we provide descriptions of the laboratory and numerical modelling tools and methodologies developed in this project. The results of the experiments and simulations, and the knowledge gained from them, particularly the time-dependent behavior of shale fractures, are reported.

2. Project Accomplishments

In the following, we will describe the experimental and numerical methods and tools developed in this project, and the obtained results. Although most of these results have been previously reported in the quarterly and annual reports, we will include them here for completeness. Newly obtained results during the final reporting period (FY2018 Q4 July 1 through September 30) are also included.

2.1 Task 2.0 Laboratory Experiments

The laboratory tasks determined the baseline properties of brittle and ductile shale samples (Year 1), and conducted long-term (weeks) core-scale fracture compaction and proppant embedment experiments (Year 2). These tasks involved development of new laboratory tools, a grain-scale, instrumented indentation test system, and a fracture compaction test system which allowed us to capture optical images of shale fracture compaction and proppant embedment in situ. Using this unique visualization tool, we correlated time-lapse images of the fracture/proppant to their mechanical (compaction) and hydrological (permeability) changes.

2.1.1 Subtask 2.1–Designing and fabrication of shale fracture test cell (Year 1)

In this task, we designed a pressure vessel for the shale fracture compaction experiment planned in Subtasks 2.4 and 2.5 (Year 2). The cell was designed so that the closure of a shale fracture can be visualized both optically through a view window and via X-ray CT through aluminum vessel walls.

2.1.1.1 In-situ optical visualization mechanism

The optical visualization required a large sapphire window attached to the vessel. We used a 2.00-inch diameter, 1.00-inch thick window from Guild Optical Associates, which gave us a window with necessary strength with a high design safety factor (SF=8) which is required for brittle pressure vessel components. During core-scale fracture/proppant compaction experiments (Subtasks 2.4 and 2.5), a disk-shaped rock core sample (diameter 2 inches, height ~0.75 inches) was pressed against a transparent similarly shaped glass disk to simulate a shale fracture subjected to compaction stress. The initial vessel design included internal illumination using an electroluminescent wire installed at the top edge of the thick sapphire window. This function, however, was not used in the actual core-scale fracture compaction experiment.

2.1.1.2 Mechanical design

The design drawings of the shale fracture compaction view cell (milestone M1) are shown in Figure 2-1. The pressure vessel consists of two pressure chambers separated by an internal piston. The upper chamber holds a shale core with an exposed fracture surface which is pressed against a transparent replica of the other half of the fracture. The flat top of the replica is pressed against an optical window (sapphire) so that the time-dependent changes in the fracture aperture distribution (with and without proppant) can be observed. The lower chamber contains hydraulic fluid which applies compaction pressure to the shale core/fracture through the piston. The displacement of the piston (and the compaction of the fracture/sample) can be monitored via an LVDT attached to a tubing extending from the piston, which also is used to inject pore fluid into the sample from the bottom center of the shale core.

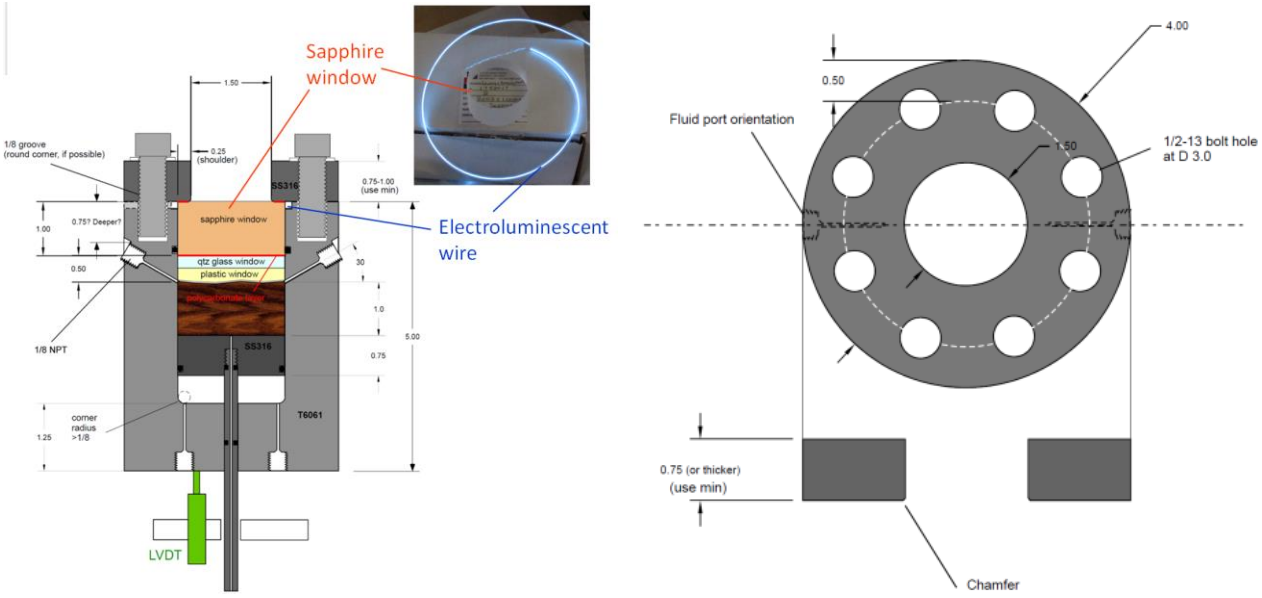

a. Overall view

b. Top flange design (SS 316)

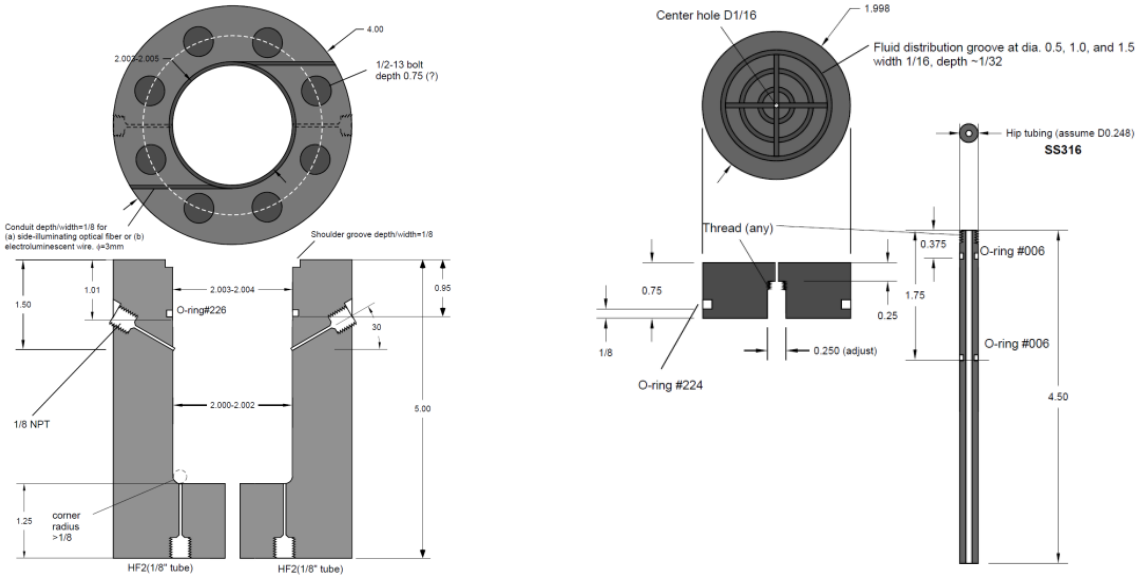

c. Main body design (T6061T6 aluminum)

d. Internal piston design (SS 316)

Figure 2-1. Design for X-ray transparent, fracture-compaction optical visualization cell.

2.1.1.3 Pressure/stress ratings

An analysis conducted by both LBNL and Vindum Engineering engineers indicated that the weakest link of this test vessel was not the optical view window as initially anticipated, but the aluminum vessel wall. In order to ensure sufficient X-ray transparency, the vessel wall needs to be kept relatively thin (~1 inch) and the material need to be selected carefully (low-copper-content, medium-strength aluminum such as T6061T6). For this reason, our originally planned 6,000 psi compaction maximum allowable working pressure (stress) on a 2-inch diameter sample was reduced to 4,500 psi, to assure the LBNL-required safety factor of 4 (Note that for the sapphire window, a safety factor of 8 is required). The planned pore pressure (fluid pressure in the fracture) was 1,500 psi.

These pressure ratings, however, assumed an ultimate strength of the aluminum to be the nominal design value of 42,000 psi. Because the strength of the actual material used for fabrication was ~16% stronger (based upon the values reported in the material certificate), we were able to increase the compaction stress rating (lower-chamber pressure) to MAWP of 5,220 psi. Also, to reduce the impact of corrosion, the wetted aluminum parts were anodized.

2.1.1.4 Completed pressure vessel and vessel performance confirmation

The completed shale-fracture compaction visualization test cell (milestone M3) is shown in Figure 2-2. We conducted a preliminary test to confirm the cell's optical and X-ray CT visualization capability for rock/fracture samples undergoing compaction (Year 1 Success Criterion). A cylindrical, 2-inch-diameter rock core (Stripa granite) was split across the core axis to produce a through-going tensile fracture. A half of this core was used to produce an optically transparent replica of the fracture using low-viscosity (visocosity~200 cP), optically transparent epoxy, with a slight mismatch with the fracture surface of the other half (Figure 2-3). Subsequently, the pair (the rock and epoxy replica samples) was introduced into the compaction visualization cell, and small axial stress was applied via an internal piston.

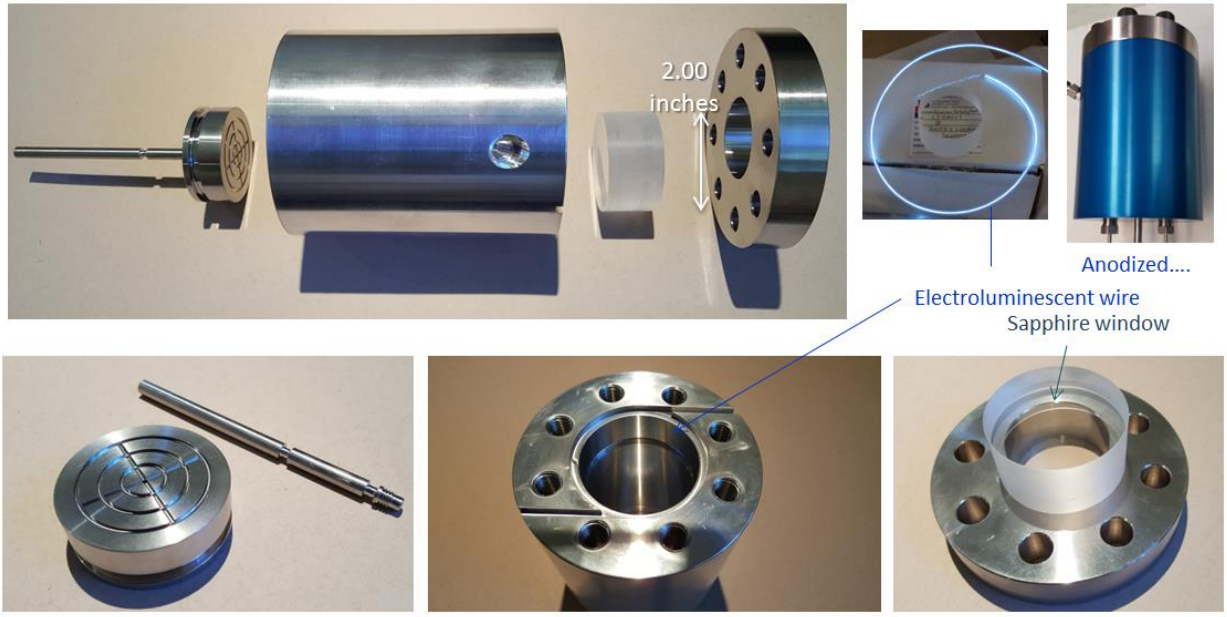

Figure 2-2. Completed shale fracture compaction visualization cell.

Optical visualization of the fracture surface was conducted through a thick sapphire window. The fracture surface was illuminated by a ring-shaped, internal, electroluminescent wire which applied even light on the surface. Subsequently, the test cell containing the sample was scanned by medical X-ray CT machine to verify the visibility of the sample through a 1 inch thick aluminum cell wall. This test demonstrated that the CT scans was able to image the density differences within the rock (quartz/feldspar and biotite mica), epoxy-rock boundaries, and thin (a few hundred microns thick) gap (or, a fracture) at the boundaries (Figure 2-4).

These tests conducted near the end of Year 1, however, revealed several problems. The optical images of a fracture illuminated by the internal lamp were somewhat degraded by multiple reflections at the

window and transparent sample surfaces. Also, from the captured two-dimensional images of a fracture, fracture aperture and contacting asperities were difficult to determine. Although X-ray CT scan images were able to provide three-dimensional aperture distribution, they were difficult to resolve very thin apertures (<~100 microns). Additionally, logistically, we could not keep the experimental setup on the CT examination table for extended durations (weeks to a month) without disturbing the system.

For these reasons, a decision was made that we did, not use X-ray CT imaging for monitoring time-lapse fracture/proppant compaction. Instead, we developed a new optical imaging technique which allowed us to determine (somewhat) quantitatively the aperture distribution within a fracture. The details of this new imaging method will be described in section 2.1.4

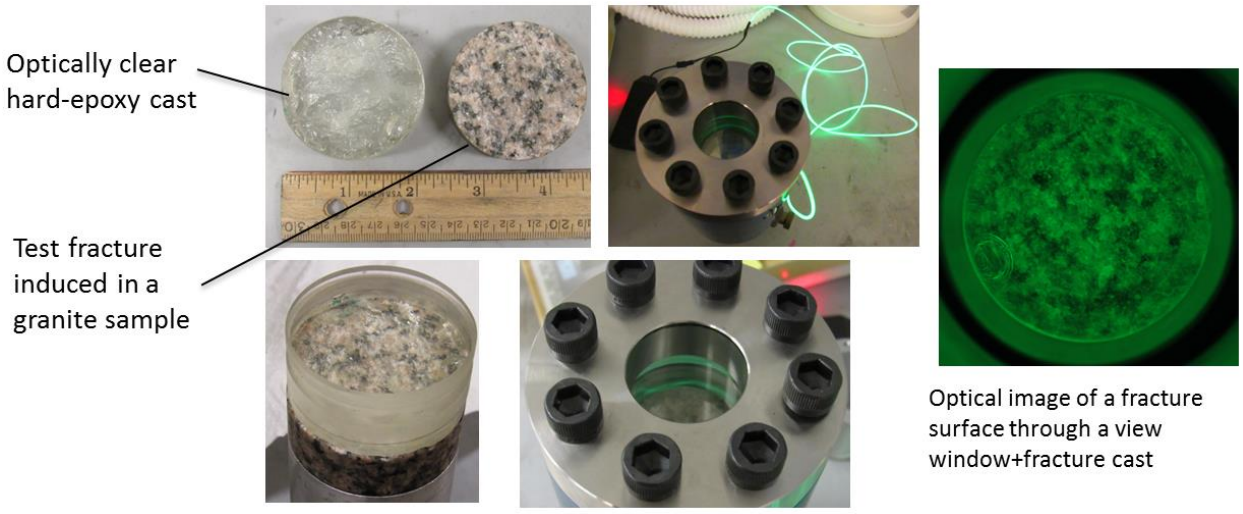

Figure 2-3. Optical visibility check for a rock fracture within a compaction visualization cell.

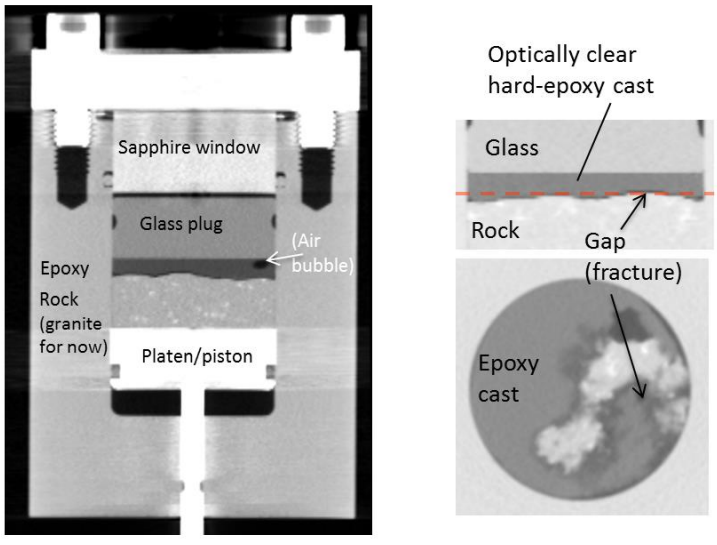

Figure 2-4. X-ray CT visibility check for a rock fracture within a compaction visualization cell.

2.1.2 Subtask 2.2– Test sample acquisition and preparation

2.1.2.1 Obtained shale samples I (Year 1)

We initially obtained five kinds of outcrop shale cores and small chips for baseline material characterization. The commercial source (vendor) which provided these samples was Kocureck Industries (TX). These shales were Mancos, Marcellus, Eagle Ford, and Barnett. Additionally, Niobrara shale which we already had at LBNL was also sent to the vendor for core shaping (2" diameter, 2" height) with the other types of shale (Figure 2-5). Of these, Mancos, Barnett, and Niobrara shale samples were cut and prepared with odorless mineral spirits (OMS), and Marcellus and Eagle Ford with water. Small subcores (diameter 0.55", height ~0.5") were also produced from the chip samples, which were used in the XRD analysis and micro-indentation experiments in Subtask 2.3.

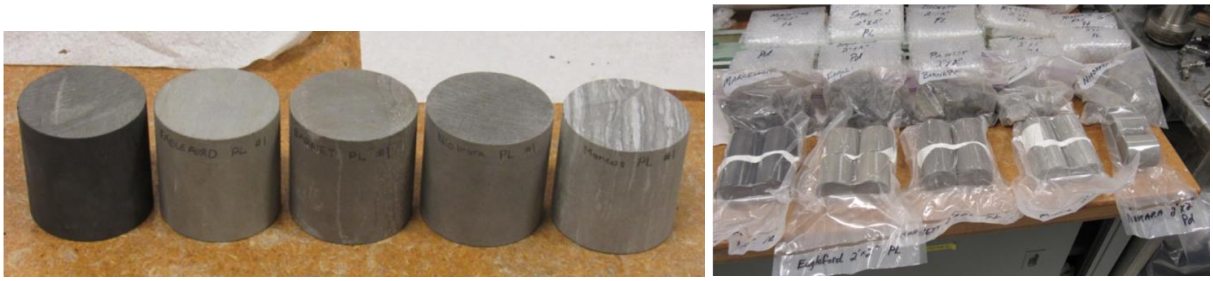

Figure 2-5. Initially obtained five types of shale samples (From the left, Barnett, Niobrara, Eagleford, Marcellus, and Mancos Shales) used in our current experiments.

2.1.2.2 Obtained shale samples II (Year 2)

During the core-scale shale fracture/proppant compaction experiments conducted in Year 2, we realized that, in spite of the initial analyses conducted in Year 1 (Subtask 2.3), which were used to select ductile shale samples, the initially obtained samples actually exhibited brittle behavior. For this reason, we added two additional types of shale. One of these was a down-hole core sample from the MSEEL laboratory (Marcellus shale), and the other was an outcrop Pierre shale core which we previously obtained from TerraTek/Schlumberger (UT). Both samples were cut with tap water.

Figure 2-6. Additional core samples exhibiting ductile and swelling behavior. A Marcellus shale core (MSEEL, depth 7,445.4-7,446 ft) (LEFT) and a Pierre shale core (RIGHT). The latter sample exhibited strongly water sensitive behavior, fracturing and losing integrity when descicated.

2.1.3 Subtask 2.3– Shale property characterization and ductility measurements (Year 1)

2.1.3.1 Modification of grain-scale instrumented indentation test system

In this task, we made several modifications to our existing micro-indentation test setup. Previously, the system had issues of (1) slow loadcell readout and (2) inaccurate displacement measurement due to system deflections (compliance). Because of these problems, we could not determine the stiffness parameters of tested materials accurately (only hardness measurements were done). A compliant, "S"-style loadcell of the old system was replaced with a fast-responding higher-stiffness force sensor [Transducer Techniques. MDB-2.5 (2.5lb max) or MLP-75 (75lb max)]. Also, a new, high-sensitivity capacitive sensor (Polytech PI, PISeca capacitive sensor) was installed to reduce the impact of the deflections in the test system, which allowed us to measure the indentation displacement separately from the indentation column driver's encoder readings (Figure 2-7). Additionally, the previous slow data readout was improved by using a National Instrument multifunction I/O device (NI USB 6003).

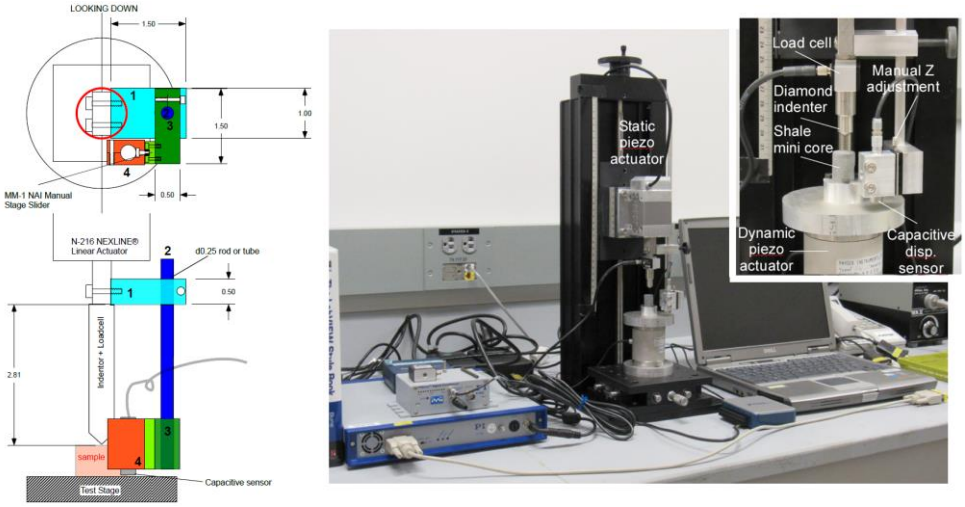

Figure 2-7. Modified grain-scale indentation test setup for high-resolution displacement measurement using a capacitive sensor

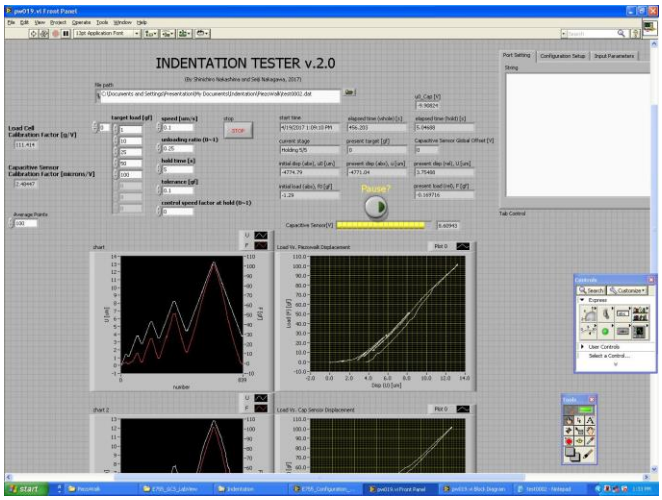

Figure 2-8. LabView code front panel

Finally, we developed a new LabView code for executing indentation tests following a programmed loading schedule, and for data acquisition (Fig.2-8). With this code, because the system's capacitive sensor's measurement range is rather limited (currently set at 50 microns) for proppant grain embedment studies, the loading automatically pauses when the range limits are reached so that the sensor position can be offset manually (using the "manual Z adjustment" in Fig.2-8).

With these changes, the indentation behavior can be determined accurately. We also planned to measure the stiffness changes during indentation continuously (e.g. Oliver & Pharr, 2004) by applying small cyclic loading to the sample, using an additional piezoelectric stage attached to the sample holder. Unfortunately, however, this additional capability was not achieved because of rather strong noise in the measurement (primarily due to cross talks between the electronics) and the lowered sampling rate due to required temporal averaging of the measurements.

An example of a preliminary, low-load, small-displacement indentation test on room-dry Opallinus Clay sample (Mont Terri, Switzerland) is shown in Fig. 2-9. Note that this system allows measurements for indentation load less than 1 gf, with less than 1 μm of displacement. The main loading curves are used to evaluate the hardness of the tested material, in combination with measurements of the smaller excursion curves which are used to determine the elastic deformation (or reduced Young's modulus).

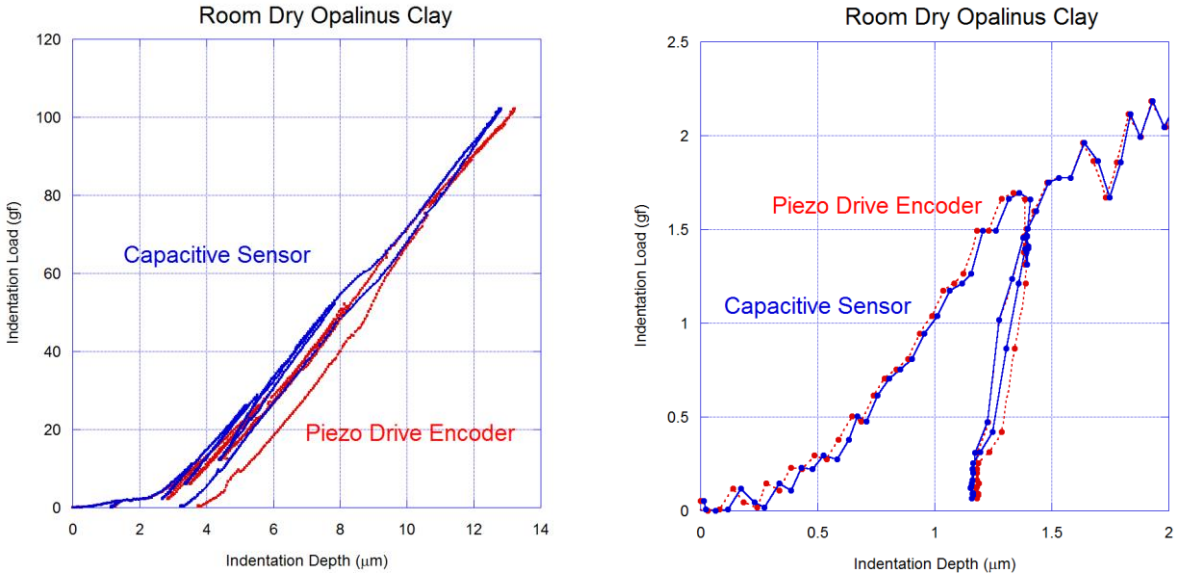

a. Indentation load-displacement curves

b. The initial part of a.

Figure 2-9. A preliminary test on a small (~0.55" diameter) Opalinus Clay core. Compared to the capacitive sensor measurement, encoder readings from the piezo drive which moves the indenter show excess deflections of the system for high load (a). The test system is capable of measuring small loads and displacements, less than 1gf and 1 μm.

2.1.3.2 Baseline sample characterization (Year 1)

a. Material Density

The mass density of as-received, room-dry samples was measured using cylindrical, 2-inch diameter samples (cored both normal and parallel to the bedding plane). The results are shown in Figure 2-10. Barnett and Marcellus shales have the highest densities at ~2.6 g/cc, followed by Mancos and Niobrara shales (~2.5 g/cc). Eagleford shale samples showed rather strange results, with bedding-normal cores exhibiting anomalously small density (~2.2 g/cc). We suspect that the provided samples were either mixed up by the supplier with other type of shales, or obtained from very different part of the host block in spite of our instructions.

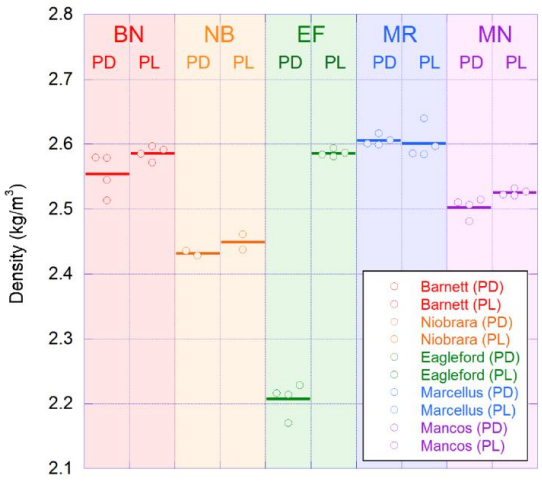

Figure 2-10. Determined mass density of the five cores (BN=Barnett, NB=Niobrara, EF=Eagleford, MR=Marcellus, MN=Mancos).

b. Anisotropic seismic velocity and TI (transversely isotropic) elastic moduli determination

Seismic velocities and dynamic elastic moduli of the shale samples were determined via ultrasonic P and S-wave velocity measurements. The measurements were performed using Panametrics 1 MHz contact transducers. The coupling between the sample surface and the transducers was established by applying small clamping force using a hand vise, mediated by a pair of thin lead foils.

For bedding-perpendicular cores, only core-axis-parallel P-wave velocity and S-wave (SH-wave) velocity were measured. In contrast, for bedding-parallel cores, velocities were determined for P-waves propagating at 0°, 45°, and 90° angles to the bedding planes and S waves with the particle motions polarized normal (SV waves) and parallel (SH waves) to the bedding planes.

Velocities measured for both types of the cores are shown in Figure 2-11. Consistent with the density measurements, bedding-perpendicular (PD) Eagleford (EF) shale cores exhibited anomalously small velocities. For the bedding-perpendicular (PD) Mancos (MN) cores, possible fracturing along the bedding planes is suspected, which resulted in very small S-wave velocities (Note that this was not the case for SV waves measured in the bedding-parallel cores).

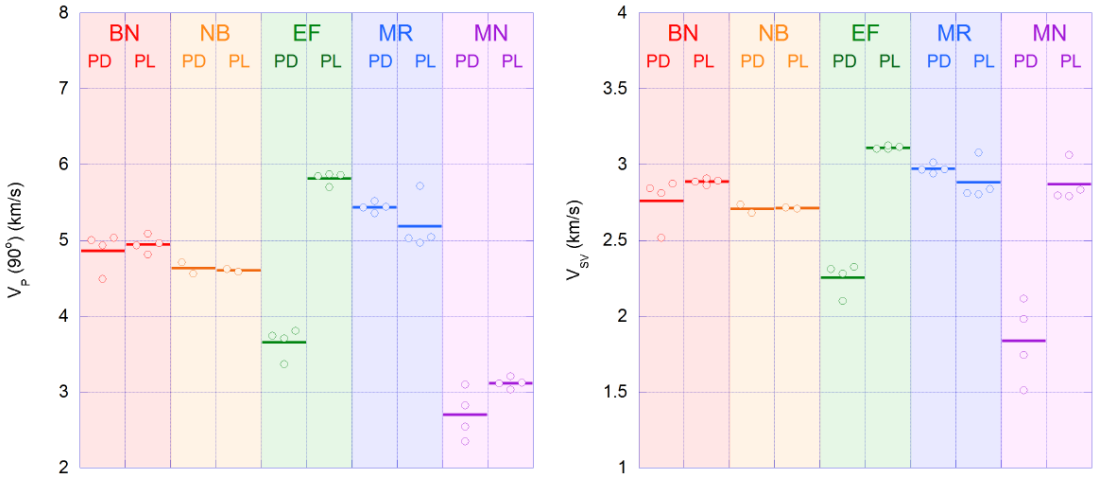

Figure 2-11. P and S-wave velocities commonly measured for bedding-perpendicular (PD) and parallel (PL) cores. (BN=Barnett, NB=Niobrara, EF=Eagleford, MR=Marcellus, MN=Mancos).

From sets of five P and S-wave velocities measured for the bedding-perpendicular cores, the five elastic constants of transversely isotropic (TI) shales were determined (e.g., Hornby, 1998). With the 3 axis designated as the axis of symmetry in Cartesian coordinates, the components of the symmetric elastic tensor (in the Voigt notation) are obtained by (Lo et al, 1986)

$$C_{11} = C_{22} = \rho V_{P0^\circ}^2,\ C_{33} = \rho V_{P90^\circ}^2,\ C_{44} = C_{55} = \rho V_{SV}^2,\ C_{66} = \rho V_{SH}^2,$$

$$C_{13} = -C_{44} + \sqrt{4\rho^2 V_{P45^\circ}^4 - 2\rho V_{P45^\circ}^2 (C_{11} + C_{33} + 2C_{44}) + (C_{11} + C_{44})(C_{33} + C_{44})},$$

$$C_{12} = C_{11} - 2C_{66}.$$

The results are presented in Table 2-1. Additionally, the dimensionless TI parameters (Thompsen parameters, Thompsen, 1986) computed from the elastic constants are also shown in Table 2-2. In these tables, C_{13} and correspondingly δ of Mancos shale are not physical and not valid. This is possibly attributed to the measurement errors (i.e., wrong wave arrival picks) due to the strongly scattered and attenuated waves by the bedding planes of the samples.

Table 2-1. Dynamic elastic moduli

	# samples	C11	C33	C44	C66	C13
Barnett (PL)	4	71.1 (1.58)	63.4 (3.04)	21.8 (0.41)	21.6 (0.35)	25.4 (2.94)
Niobrara (PL)	2	62.6 (0.26)	51.9 (0.19)	20.0 (0.01)	18.0 (0.06)	17.2 (0.65)
Eagleford (PL)	4	89.5 (1.02)	87.6 (2.51)	25.4 (0.49)	25.1 (0.15)	41.7 (1.82)
Marcellus (PL)	4	78.9 (7.10)	70.4 (10.6)	23.7 (1.48)	21.7 (2.24)	30.5 (4.97)
Mancos (PL)	4	35.7 (0.77)	24.5 (1.11)	22.8 (1.15)	20.8 (1.89)	-17.6 (5.09)

NOTE: The number in the parenthesis is the standard deviation

Table 2-2. Thompsen anisotropy parameters

	ε	γ	δ
Barnett (PL)	0.062	0.006	0.088
Niobrara (PL)	0.100	0.053	0.027
Eagleford (PL)	0.011	0.008	0.051
Marcellus (PL)	0.064	0.048	0.054
Mancos (PL)	0.230	0.048	-

c. X-ray diffraction (XRD) tests

XRD analyses were conducted in collaboration with Marco Voltilini (LBNL) who was also a team member of the Reagan (LBNL)/Moridis (LBNL/Texas A&M) project. The analysis was performed on chip samples from the same shale blocks from which the aforementioned 2-inch core samples were taken. Both mineral and clay composition are shown in Figure 2-12. Generally, the shale samples contained rather large amounts of carbonates, except for the quartz-rich Mancos shale sample and the clay-rich Barnett shale. All the samples contained very little smectite which generally can result in strongly swelling behavior.

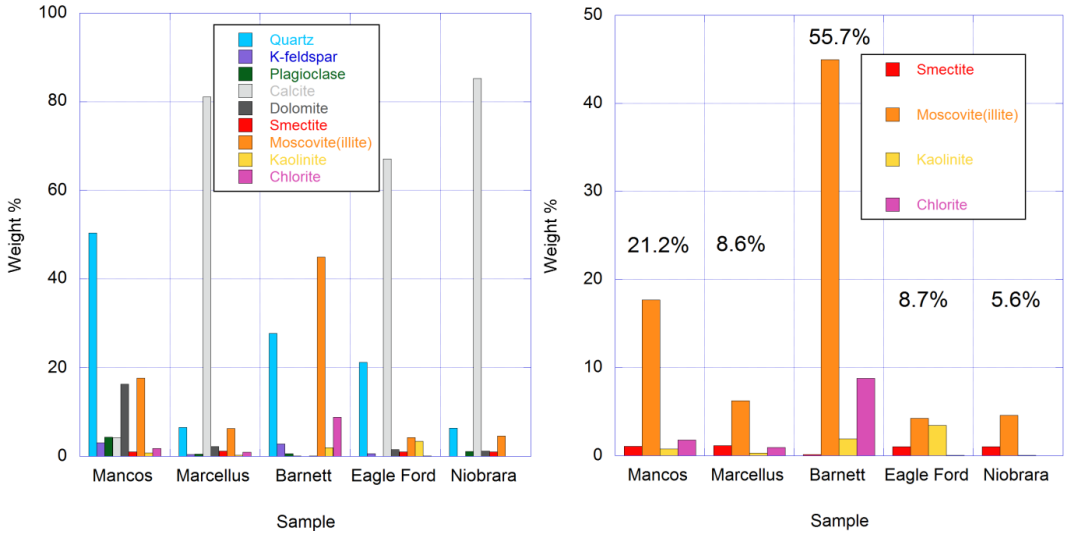

a. Mineral composition

b. Clay composition (the numbers indicate clay total %)

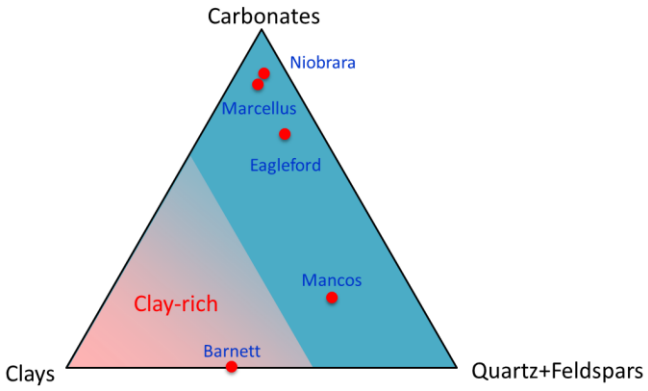

c. Ternary diagram

Figure 2-12. Mineral composition analysis via XRD

d. Grain-scale indentation experiment

Grain-scale indentation experiments were conducted using the instrumented indentation test system which has been developed at LBNL by the current project (Figure 2-13a). Small shale samples (diameter 0.55 inches) cored parallel to the bedding plane were glued to an aluminum substrate (Figure 2-13b) which was then bolted down to a test table. The samples were first oven dried at 60°C for 1 week, then tested under ambient temperature and humidity. Subsequently, the same samples were exposed to 100% relative humidity air for 10 days at room temperature, and the test was repeated. During the latter experiment, the sample surface was immersed in odorless mineral spirits (Sigma Aldrich, CAS68551-17-7) to avoid evaporation loss of the water in the samples.

Each indentation experiment was conducted using a constant displacement rate of 0.5 μm/s (indenter displacement rate) except for calibration tests using aluminum and optically transparent epoxy (0.1 μm/s). The maximum applied force was 5,000 gf (=49 N), and 50% unloading was conducted at 100 gf, 250gf, 500 gf, 1,000 gf and 2,000 gf (Figure 2-14). For a wet Barnett Shale sample, however, very large indentation resulted in splitting of the sample under 2,500 gf and 5, 000 gf forces. For this reason, the maximum force was reduced to 1,000 gf.

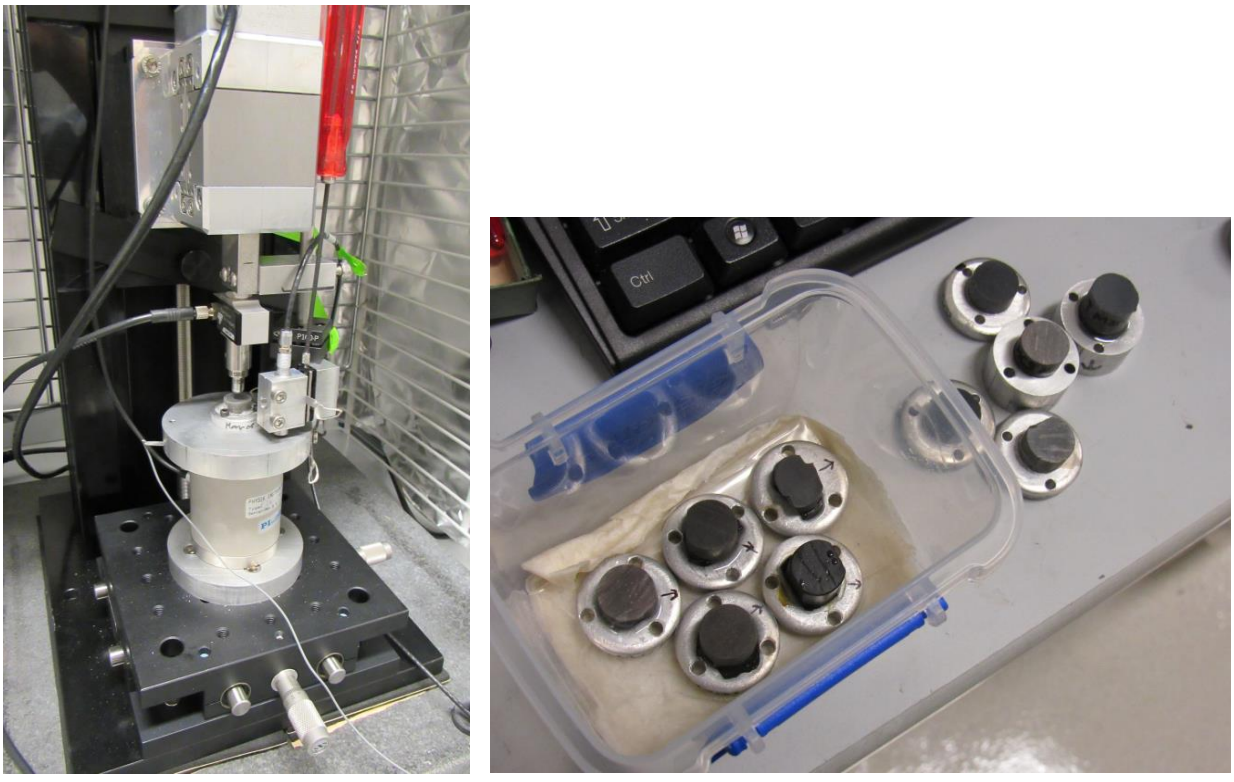

a. Test in progress

b. Indentation test samples

Figure 2-13. Micro-indentation experiments on shale subcores

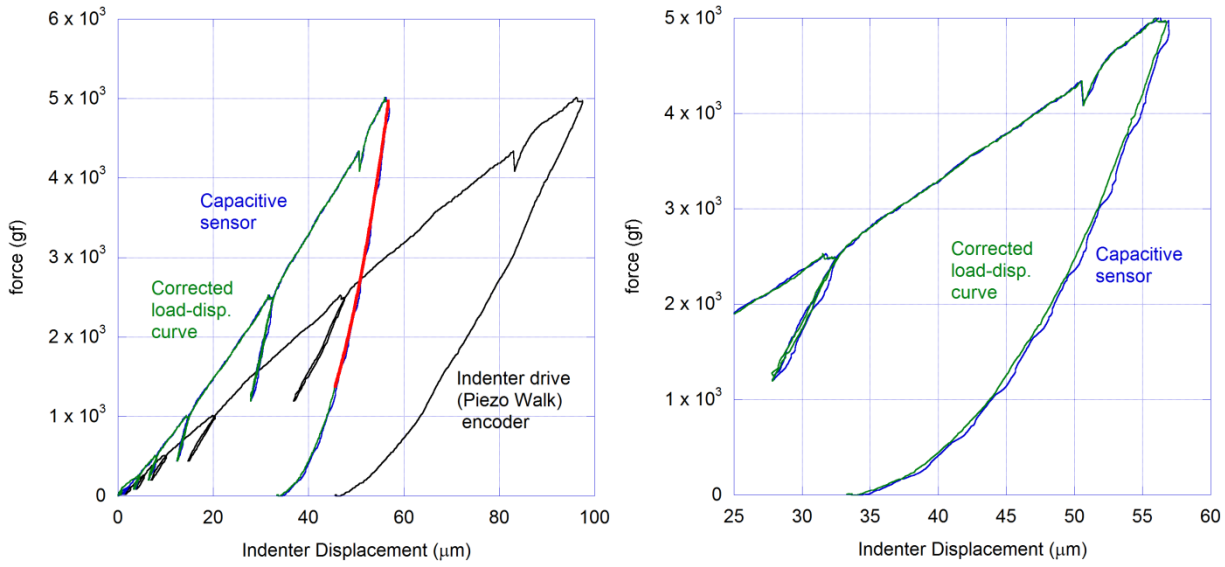

a. Indentation load-displacement curves

b. Correction of capacitive sensor cross-talk noise

Figure 2-14. Force-displacement measurements during indentation tests. An example for a dry Barnett Shale sample is shown here. An output from an indenter drive displacement encoder including large system deflections (a) and an output from a capacitive sensor exhibiting electrical cross talk noise (b) were combined to eliminate the undesired errors and noise from the indentation displacement data. The red curve in (a) is a fitted curve use for determining the elastic stiffness of the sample.

Because of excessive system deflections included in displacement encoder output, we employed a high-sensitivity capacitive sensor attached directly to the indentation column (loadcell+indenter holder+indenter+sample+sample holder). Unfortunately, to this date, we have not been successful in eliminating unwanted electrical cross-talk between the piezoelectric drive (Piezo Walk) and the capacitive sensor. Currently, this problem is mitigated by combining the smooth (but containing the system deflections) output from the encoder and low-deflection (but containing semi-periodic electrical noise) output from the capacitive sensor to produce “correct” displacement data (Figure 2-14).

Once the measurements were completed, the geometry of the indentations was quantified via both high-resolution optical surface profilometry and optical microscopy. Indentation diameter in particular is a critical parameter that is needed to determine the (reduced) Young’s modulus and the hardness parameter from an indentation test. The optical profilometry can provide three-dimensional geometry while the observations and photo images through a microscope provide only the diameter and area of indentations (Figures 2-15 and 2-16). We found, however, that microscope observation was sometimes more accurate and efficient, when an indentation was shallow and the surface of the sample was not very smooth. In these cases, plane laser beam projected on the surface at a shallow angle can enhance the image for improved quantification of the indentation diameter (Fig.2-16b).

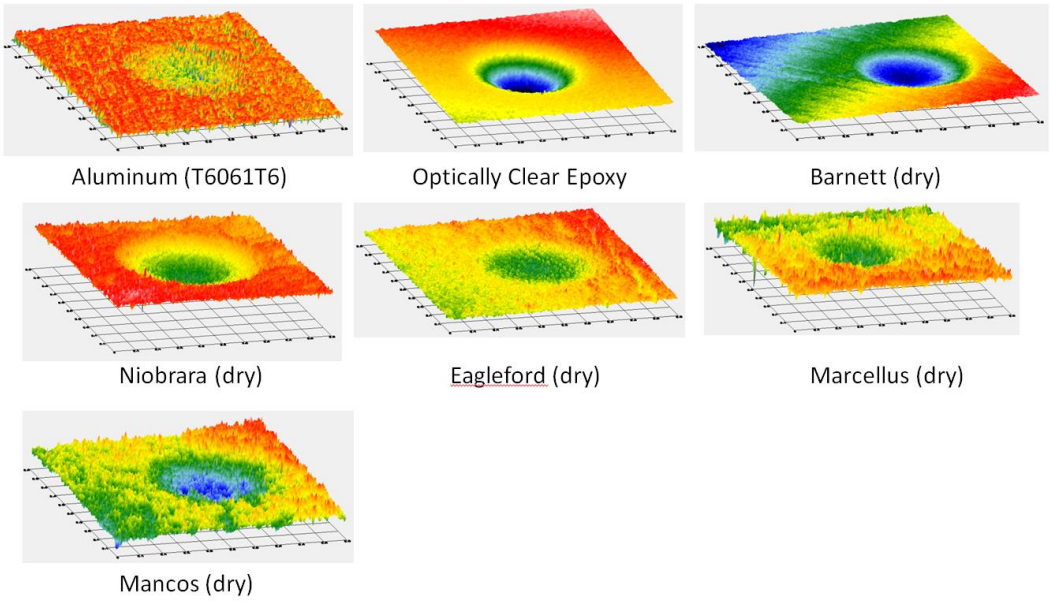

a. Bird's eye view of indentation topography

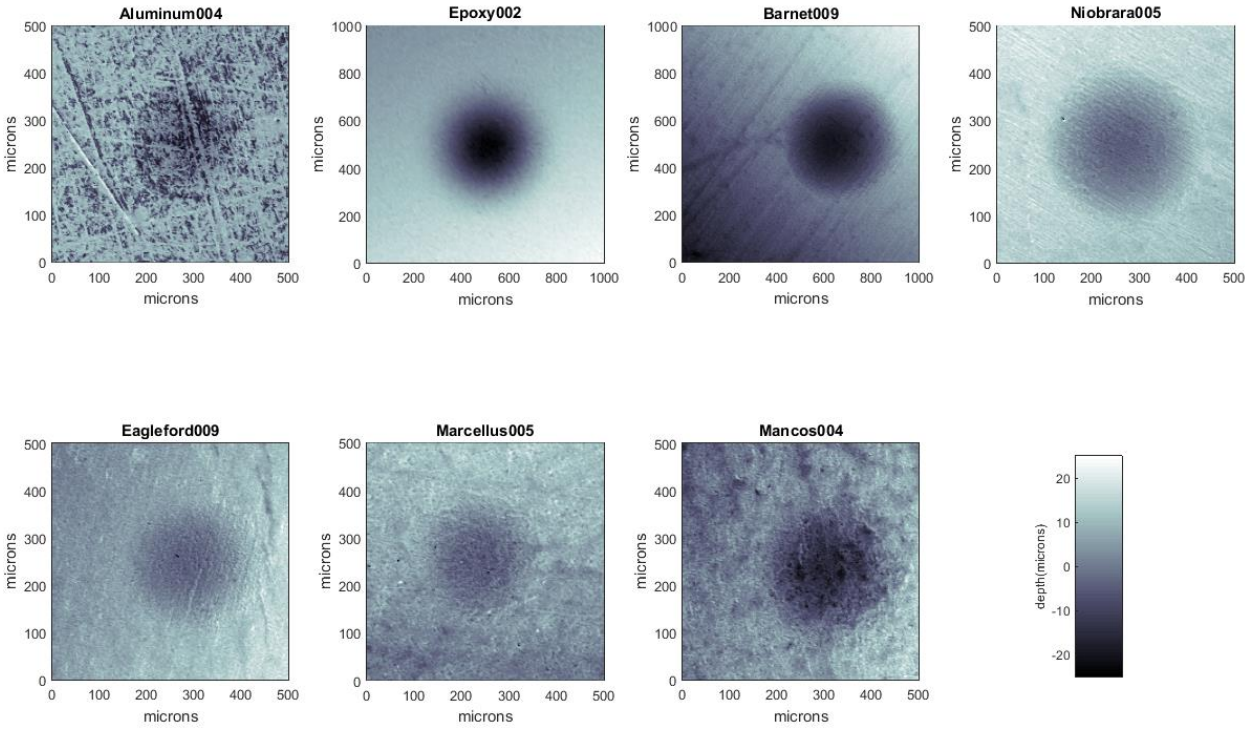

b. Plane view of indentation geometry. The gray scale indicates the depth.

Figure 2-15. 3-D surface profile measurements of indentations. For small indentation depths and rough surface geometry, obtaining the indentation depth and diameter accurately can be difficult.

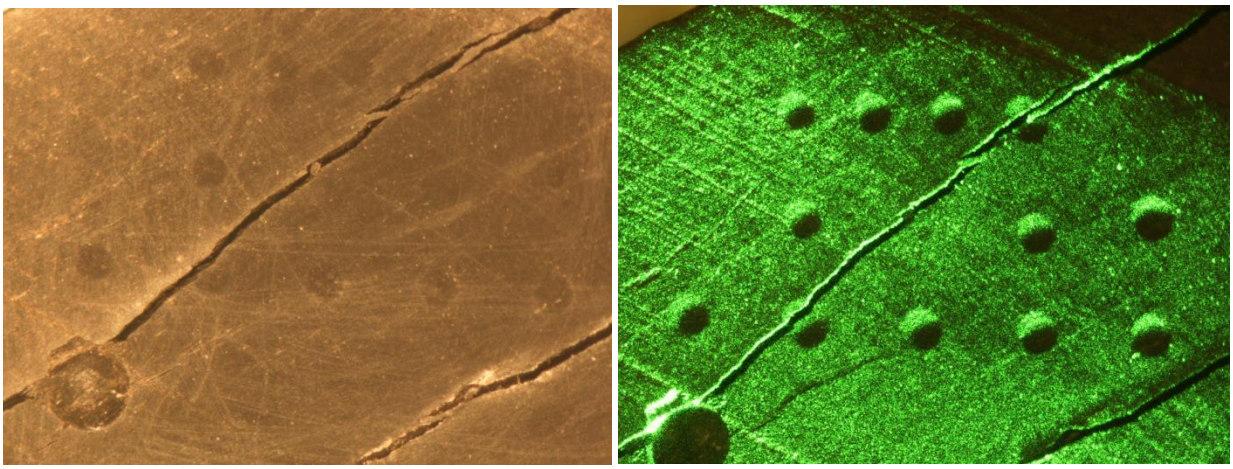

a. Indentations in normal light

b. Indentations in shallow-angle laser beam

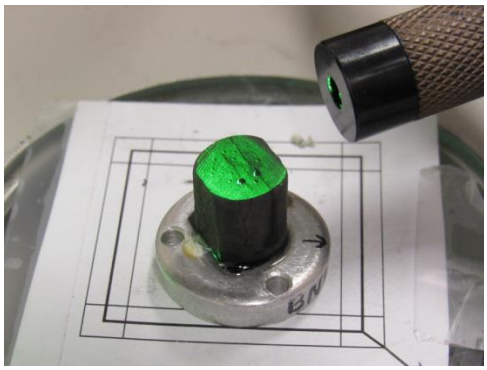

Figure 2-16. Optical microscope measurement of indentations. The test results for a Barnett Shale sample under dry and wet conditions are shown here. For difficult-to-image, shallow indentations, a small-angle projection of plane laser beam can enhance indentation images.

In our experiments, each indentation test curve produces three key parameters characterizing mechanical properties of shale: (1) reduced Young's modulus (E_R), (2) hardness (H), and (3) ductility index (I_D). E_R is computed from

$$\frac{1}{E_{apparent}} = \frac{1}{E_R} + \frac{1-\nu_{indenter}^2}{E_{indenter}} + C_{system} \ , \ \frac{1}{E_R} \equiv \frac{1-\nu_{sample}^2}{E_{sample}} .$$

Where $E_{apparent}$ is the apparent moduli from the experiment, E_{sample} and ν_{sample} are the sample's Young's modulus and Poisson ratio (Note that isotropy is assumed here), and $E_{indenter}$ and $\nu_{indenter}$ are the indenter's Young's modulus and Poisson ratio, respectively. C_{system} is the contribution from the compliance of the loading system. $E_{apparent}$ is related to the experimentally measured elastic stiffness $S_{apparent}$ determined from the slope of the initial unloading part of the force-displacement curve as in Figure 2-8a (e.g., Oliver and Pharr, 2004), via

$$E_{apparent} = \frac{S_{apparent}}{2\beta}\sqrt{\frac{\pi}{A}} = \frac{S_{apparent}}{\beta D} .$$

A is the area of indentation, *D* is the diameter, and β is the indenter shape function (a value of 1.05 is recommended by Oliver and Pharr). In our experiment, $S_{apparent}$ was determined by fitting a 2nd-order polynomial to the final unloading curve from the maximum indentation load (5,000 gf in most cases), and evaluating its slope (stiffness) at the maximum load. Assuming indenter's Young's modulus and Poisson ratio ($E_{indenter}$ =600 GPa and $\nu_{indenter}$ =0.31 for tungsten carbide) and for an aluminum sample (E_{sample} =72 GPa and ν_{sample} =0.33), the measured average indentation diameter *D*=246.78 μm and average stiffness $S_{apparent}$ =587 gf/μm yield

$$C_{system} = \frac{1}{E_{apparent}} - \frac{1-\nu_{sample}^2}{E_{sample}} - \frac{1-\nu_{indenter}^2}{E_{indenter}} = 3.1163 \text{ (1/Pa)}.$$

Note that the system stiffness in more appropriate unit is defined via $S_{system} = \beta D / C_{system}$. This value is used to compute $E_R = E_{sample} / (1-\nu_{sample}^2)$ for shale samples.

The indentation stiffness for a spherical indenter is simply given by the maximum applied force *P* devided by the area of indentation, with a correction by the indenter's diameter *d*. In typical Brinell indentation tests, this is given in kg/mm unit as

$$H = \frac{2P}{\pi D\left(D - \sqrt{D^2 - d^2}\right)}.$$

Lastly we define a ductility index as a ratio between the permanently consumed energy including plastic and viscoelastic work ($W_{permanent}$) against the maximum work during the experiment W_{total} (e.g., Hay and Sondergeld, 2010)

$$I_D = \frac{W_{permanent}}{W_{total}} = 1 - \frac{W_{elastic}}{W_{total}}.$$

Note that the elastic energy stored in the system is subtracted from the above using the determined system compliance C_{system}, assuming a linear-elastic response. In Figure 2-17, the three parameters are presented, for the five types of shale before and after the exposure to 100%RH air. For comparison, the results for aluminum (AL) and the optically transparent epoxy (EP) are also shown. Note that the experiments on wet Barnett Shale sample involved maximum indentation force only up to 1,000 gf, because higher loads resulted in fracturing of the sample. The clay-rich Barnet Shale sample exhibited smaller modulus and hardness, and larger ductility than other samples. The small reduced Young's modulus is interesting, however, because the dynamic modulus was not very different from the others, indicating a frequency-dependent stiffening effect. Niobrara Shale showed very little sensitivity to water. Other types of shale show a varying degree of sensitivity to water. However, the ductility parameter did not show large changes (particularly Marcellus Shale), which seems to indicates that the increases in the ductile deformation is accompanied by the same degree of increases in the elastic compliance.

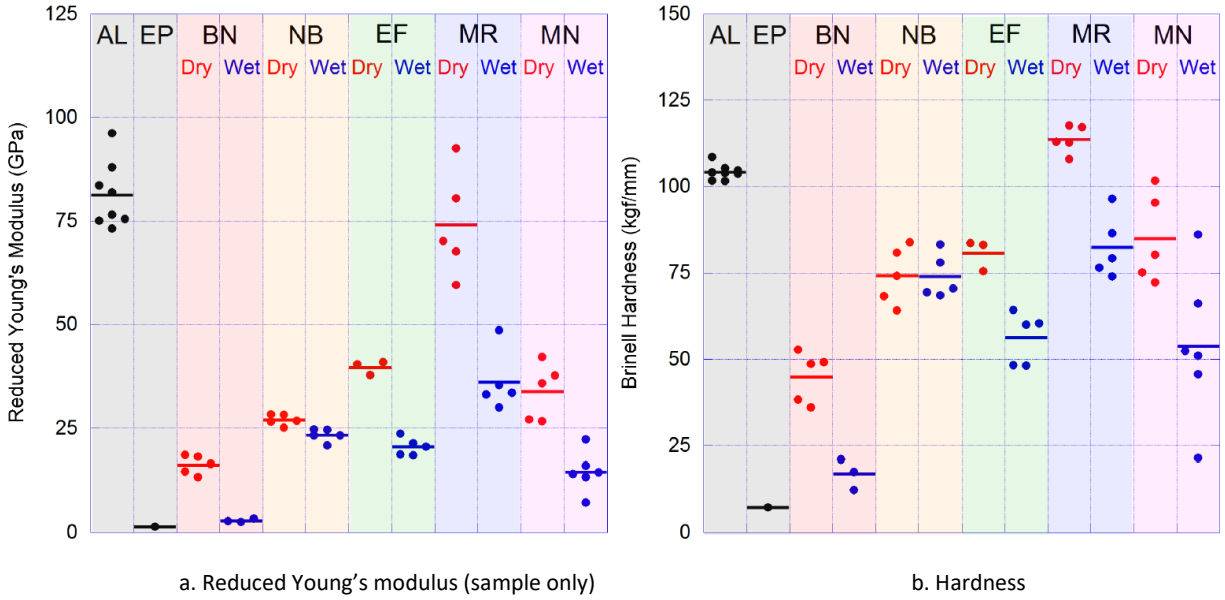

a. Reduced Young's modulus (sample only)

b. Hardness

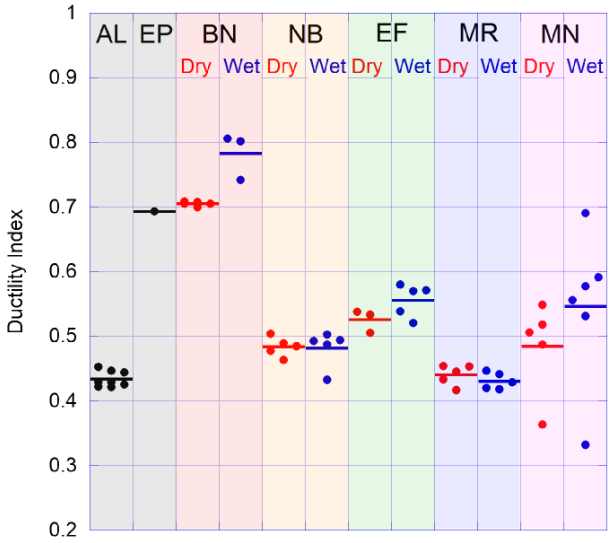

c. Ductility index

Figure 2-17. Reduced Young modulus (a), hardness (b), and ductility index (c) for five types of shale samples. For comparison, results for aluminum (AL) and optically transparent epoxy (EP) are also shown.

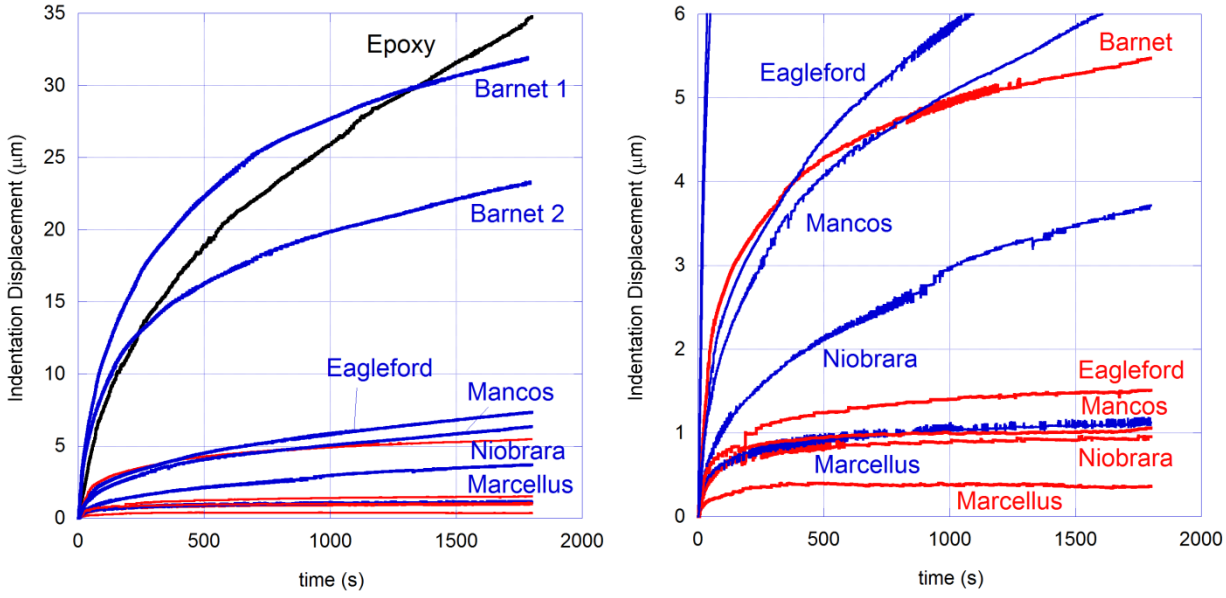

a. Wet samples

b. Room dry samples

Figure 2-18. 30-minute Creep tests for viscoelastic property assessment

Lastly, for each shale sample, a short-term (30 minutes) creep test was conducted at the maximum indentation load (1,000 gf for wet Barnett sample. 5,000 gf for all the other samples) (Figure 2-18). All five shales exhibited some increases in the viscoelastic deformations after exposed to water, including Niobrara Shale which showed little changes in the ductility index. Again, Barnett Shale sample exhibited by far the most rapid increases in the viscoelastic deformations for both dry and wet samples, indicating a strong impact of the large clay content.

To summarize, we have successfully conducted instrumented indentation tests to distinguish differences in the mechanical properties of shales including ductile and viscoelastic behavior, which will be used in the subsequent core-scale compaction experiments. Lessons learned from these experiments are as follows:

1. Clay-rich Barnett shale is best for investigating the impact of fracture deformation and proppant embedment on fracture permeability loss, followed by Mancos and Eagleford Shales.
2. Marcellus and Niobrara shales appear to be less sensitive to water and exhibit smaller ductility. However, their sensitivity to water manifests itself in different manners (reduction in the hardness for Marcellus, and time-dependent deformations for Niobrara).
3. As observed for Barnett shale samples, indentation of asperities and proppant grains can potentially lead to splitting of shale cores along the bedding planes. Based upon this observation, in the follow-up tests (section 2.1.3.3), shale chips were embedded in a small, thick-wall aluminum cup, to prevent tensile fracturing of the sample during the tests.
4. A grain-scale indentation experiments indicated that the epoxy used in a transparent fracture replica for optical visualization was too soft, and its large viscoelastic deformations masked the deformation of the shale itself. For this reason, the original idea of using an epoxy cast as for the upper half of a shale fracture was abandoned. Instead, in Subtask 2.4, a flat, glass plate with a rough surface will be

used with a flat and polished surface of a shale sample. Although the surface and aperture geometry of the fracture may not look realistic, this actually provides more useful experimental results. This is because such samples allow us to compare the behavior of the fractures in different types of shale without impacted by the macro-scale differences in the fracture surface topography.

2.1.3.3 Follow-up baseline sample characterization (Year 2)

As we commented in 2.1.2.2, core scale fracture compaction experiments in Subtask 2.4 led us to think that the ductile shale samples (which we chose to use based upon the baseline characterization tests) were in fact brittle, with little clay content. In Fig. 2-19a, XRD analysis results of small subcores taken from the cores used for the fracture compaction tests (in red) are shown for the Barnett shale and Marcellus shale, compared against the earlier results (in blue) obtained using chip samples of the same shales. Results for the additionally selected Marcellus shale cores from MSEEL and Pierre shale are also shown. The results indicate that the clay content of the core sample of the Barnett shale had extremely different amount of clays compared to the chip sample, with very little clay and rich in carbonates. Also, interestingly, the Marcellus shale samples obtained from an outcrop (provided by a vendor) had a very similar mineral composition (i.e., rich in carbonates) as the Barnett shale core sample, but had a very different mineral composition from the Marcellus shale cores from a MSEEL borehole, which was rich in clay and quartz/feldspar.

The extreme differences in the mineral compositions are puzzling, and perhaps, this indicates difficulties in testing naturally highly heterogeneous shale samples and possible biases in the material properties of recovered samples—stronger and clay-poor samples tend to be selected when larger samples are obtained for laboratory experiments.

The XRD test also revealed a possible cause of the water-sensitive behavior of the Pierre shale seen in Figure 2-6. In Figure 2-19b, even though the total clay content is very similar for the MSEEL Marcellus shale sample and the Pierre shale sample, the latter contains a moderate amount of pure smectite.

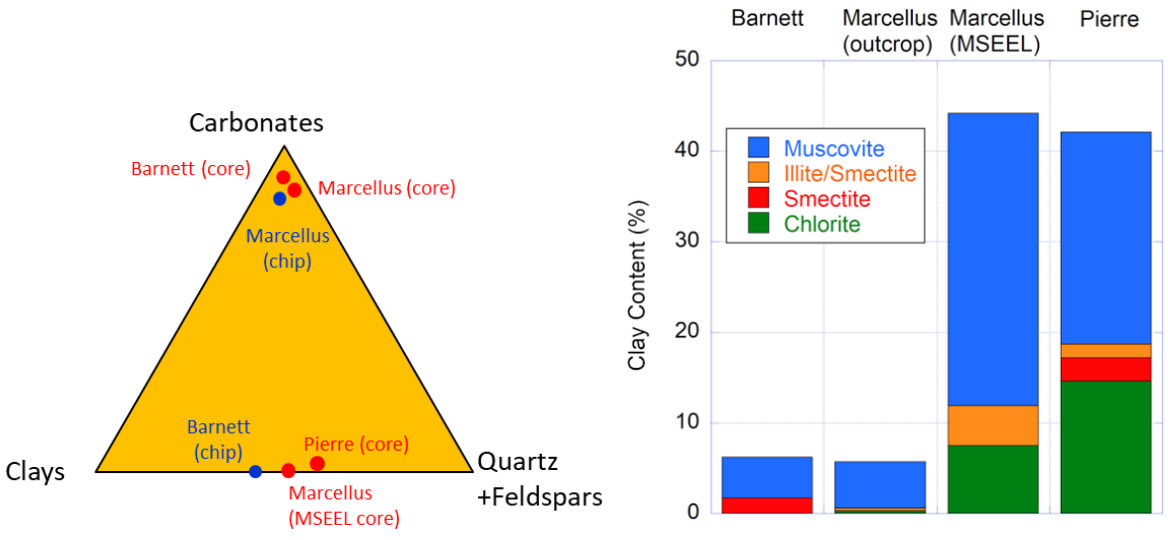

a. Ternary diagram

b. Clay composition (all for core samples)

Figure 2-19. Mineral composition analysis via XRD

Short-term (30 minutes) grain-scale indentation test curves are shown in Fig.2-20, corresponding to each sample in Figure 2-19. Before (overnight) and during the tests, the indentation test samples were soaked in 5% NaCl aq, under room temperature. To avoid possible "wedge fracturing" of the samples during indentation, these samples were cast within a small, thick walled aluminum cup (shown in the photograph) using low-viscosity epoxy. The carbonate-rich samples all showed very similar trends, exhibiting large elastic moduli (steep slope), very small creep displacement (plateau at the highest load), and small hysteresis. In comparison, the clay-rich samples exhibited marked differences from the carbonate-rich samples, showing much stronger ductility. The degree of the ductility, however, was different among the samples, indicating the important role of factors other than the mineral composition depicted by a ternary diagram.

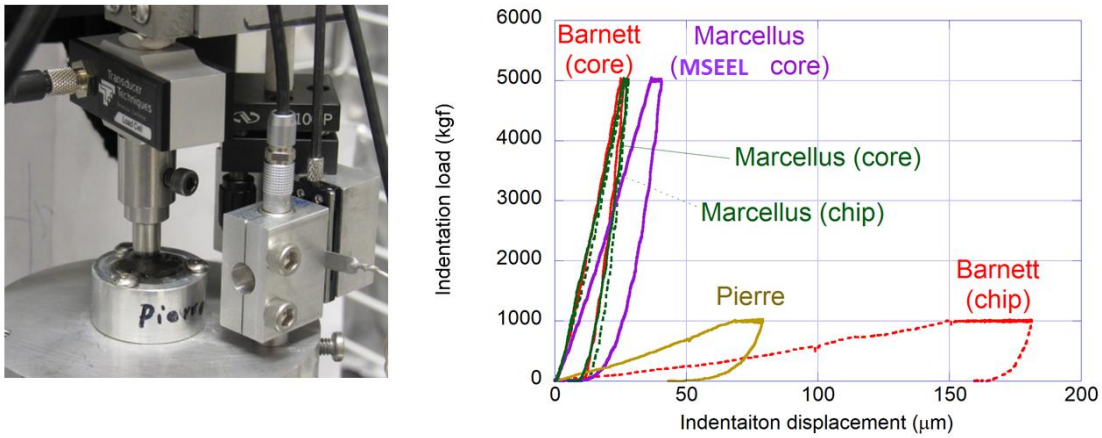

Figure 2-20. Short-term (30 min hold) indentation creep tests

2.1.4 Subtask 2.4–Fracture closure experiment I: w/o proppant (Year 2)

In this task, we conducted shale fracture compaction and permeability change measurements using the compaction/view cell fabricated in Year 1. From the shale sample property characterization experiments in Subtask 2.3 and also while preparing for the current task, we identified several issues with the originally planned experimental protocols:

1. The transparent epoxy used to cast a natural fracture is too soft and ductile compared to the obtained shale samples, which will obscure the deformation of the shale itself if used as the upper half of the fracture constituting the window for optical visualization.
2. Geometry of the fractures induced in different cores (and of different shale types) can vary significantly, making comparison of the fracture closure behavior difficult.
3. Aperture (not the surface tomography) of hydraulic fractures in shale without proppant is expected to be very small, because the opposing surfaces of a fracture are highly correlated.

At the early stage of Subtask 2.4, several modifications of the test setup and development of new experimental methods have been made to address these issues.

2.1.4.1 Preparation of the experimental system

a. Transparent fracture surface model

In order to make the transparent upper-half of the fracture strong (so that measured displacement can be attributed only to the shale deformation), it has to be made of hard and stable materials such as glass. First, we attempted to make borosilicate glass casts of a tensile fracture induced in a graphite core (Figure 2-21a), and of a nominally flat, damaged surface of a graphite core, made by compressing a 50-grit sand paper against it (Figure 2-21b). In both cases, melting the glass over 24 hours at 900˚C did produced casts, but these were not suited for the visualization experiment because of clouding of the surfaces. Although further refinement of the technique may improve the sample quality, for lack of time and resource, we decided to abandon this method for now.

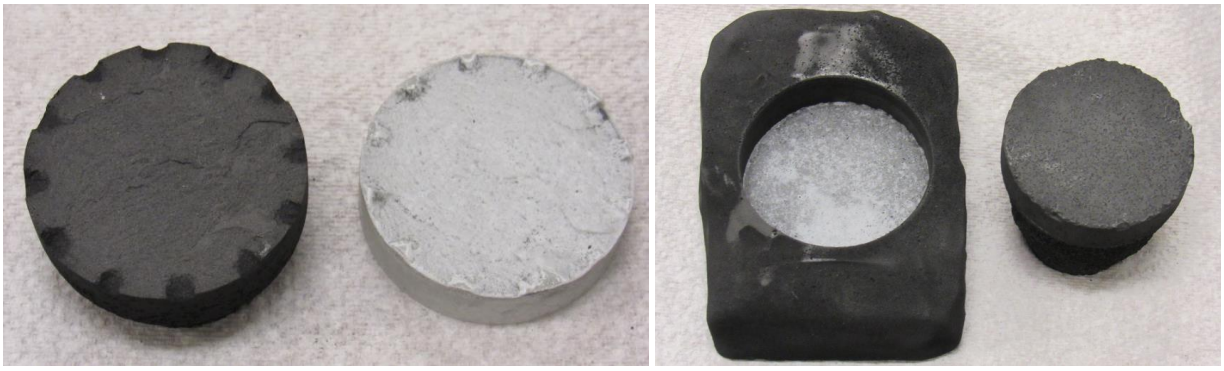

a. Tensile fracture b. Impressions from a sandpaper surface

Figure 2-21. Attempt to produce borosilicate glass casts using graphite molds. Because of possible degassing at the interface, the resulting samples became cloudy.

An alternate approach was to use a glass disk with a heavily sand-blasted surface (Figure 2-22). The created artificial rough surface was nominally flat. Such a surface in fact may be appropriate for modeling the aperture distribution between slightly mismatched surfaces of a hydraulic fracture in shale, which exhibit strong correlation at large (larger than asperity size) scales and weak correlation at small scales (Figure 2-23). Because the lower half of the fracture consisting of a natural shale sample can be flat and polished, if the same glass model is used for the upper half in different experiments, mutually comparable compaction data can be obtained for different shale samples without affected by the fracture geometry.

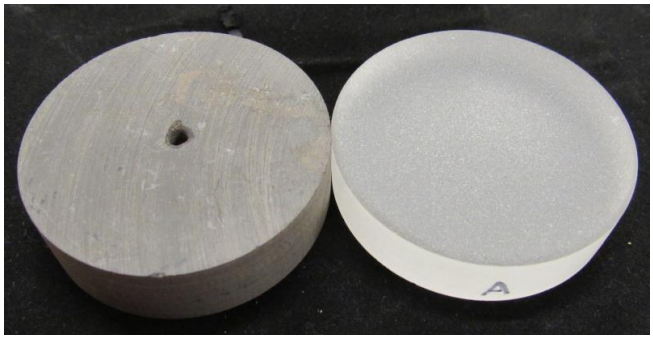

Figure 2-22. Polished Barnett shale disk (with a center hole) and a borosilicate disk with a sand-blasted surface.

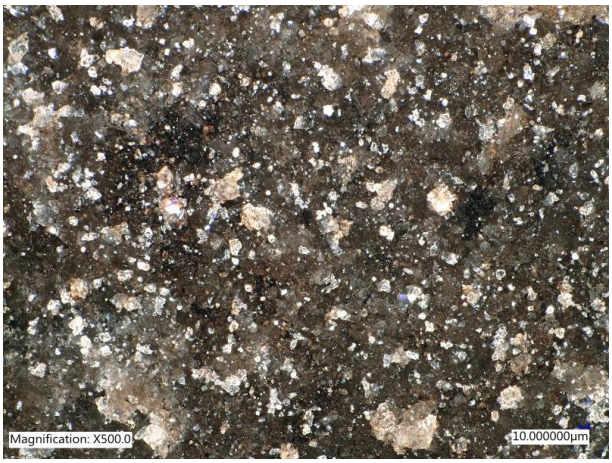

a. Barnett shale fracture (bedding parallel surface)

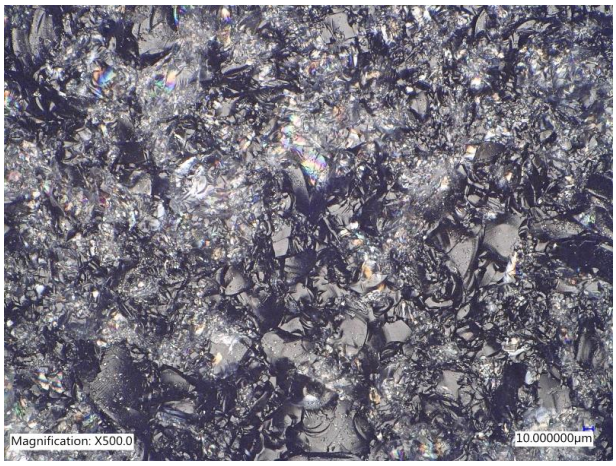

b. Photo image. Sand-blasted glass surface

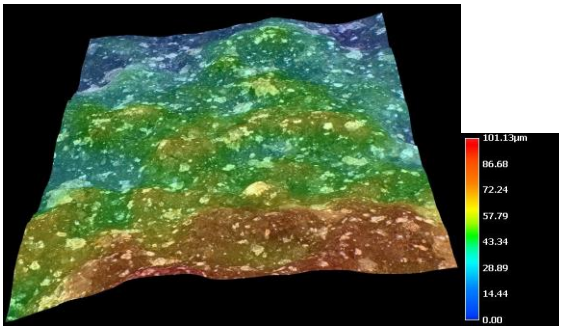

c. Barnett shale fracture surface geometry

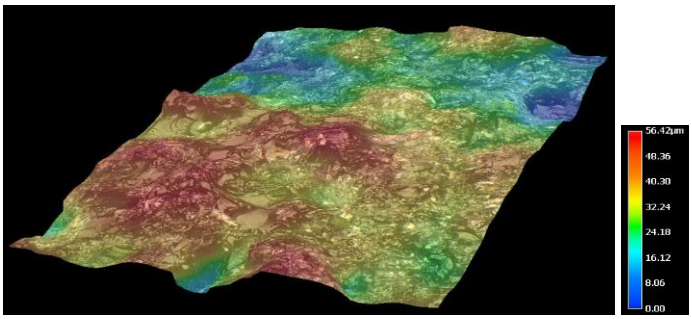

d. Sand-blasted borosilicate glass surface geometry

Figure 2-23. Images and geometry (height distributions) of a tensile fracture in a Barnett shale core (sub-parallel to the bedding direction) and of a sand-blasted surface of a borosilicate glass. Courtesy D. Senkbell, Keyence, using VHX6000 microscope on LBNL samples.

This sand-blasting method may be further extended to modify the surface geometry of the glass sample by applying a hard mask on the glass disk (i.e. using the lithography technique), preferentially etching thin parts of the mask (Figure 2-24). Although we successfully produced a glass sample with a complex surface topography, uneven application of blasting resulted in preferential etching near the center of the sample. Additionally, the details of the shale fracture surface were lost in the blasting process. For these reasons, this method was not used in the subsequent experiments.

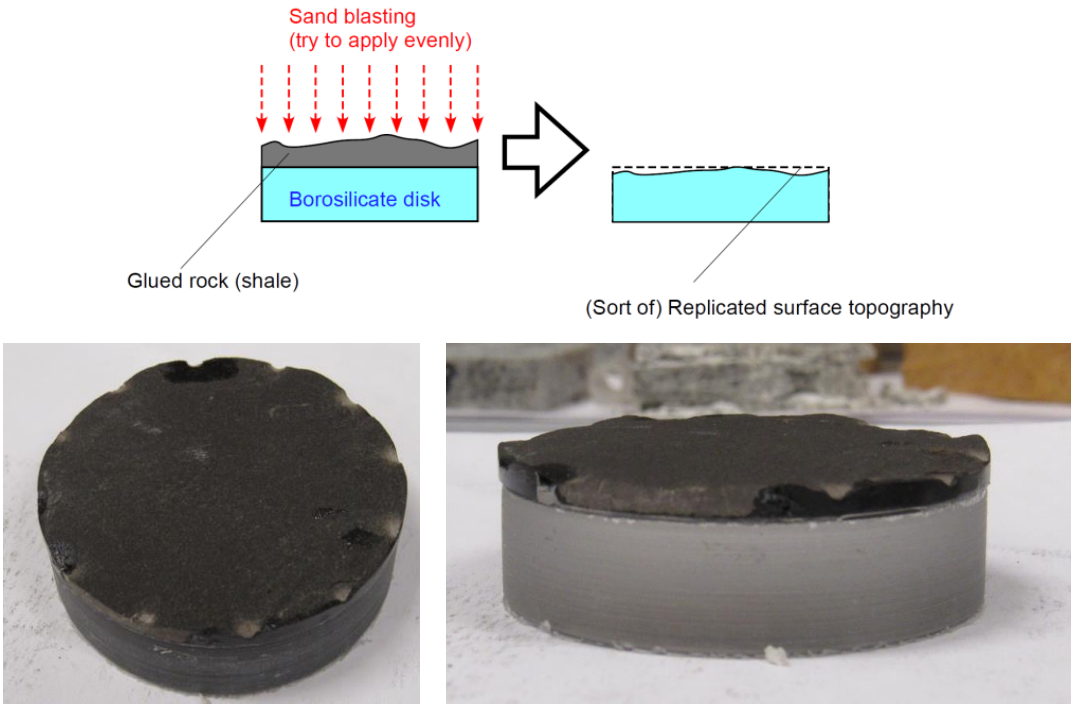

Figure 2-24. Idea of lithographic imprinting of natural fracture geometry on a glass disk via sand blasting

b. Optical visualization of fracture aperture

During optical visualization, because of the multiple window layers consisting of different materials with varied refractive index, we experienced degradation of the fracture image by the reflections. Another problem was that the contacting asperities and fracture aperture distribution was very difficult to visualize when the fracture was filled with fluid. This problem was worse particularly when the aperture was small, which will be the case when a sand-blasted glass model is used on a flat surface of a shale core.

To mitigate these problems, we developed an optical imaging method using UV light to illuminate the fracture so that the fluorescent, visible-range light produced within the fracture can be imaged without strong reflections. The differences in the intensity of the fluorescence can be related to the thickness variations in the fracture. The use of this technique is demonstrated in Figure 2-25. In this example, Letters are etched on a flat surface of an alumina-silicate core (black, poreless solid). The surface profile near the center of the core is shown on the right. In figure 2-26a, a flat glass window is pressed against the sample, which makes the letters difficult to see. In figure 2-26b, the “fracture” is filled with 1%wt Water-GLO® 802 (Spectroline), which makes the capital letters with deeper grooves visible (Note that weak fluorescence induced by the natural light is already visible in this image). When illuminated by a long-wavelength UV lamp (Figure 2-26c), both capital and small letters as well as very small aperture differences between the center and the edge of the surface can be seen from different intensities of the green fluorescent light. When the fluorescent fluid is used in the sand-blasted glass model, both large and small-scale aperture changes within a fracture can be visualized (Figure 2-27).

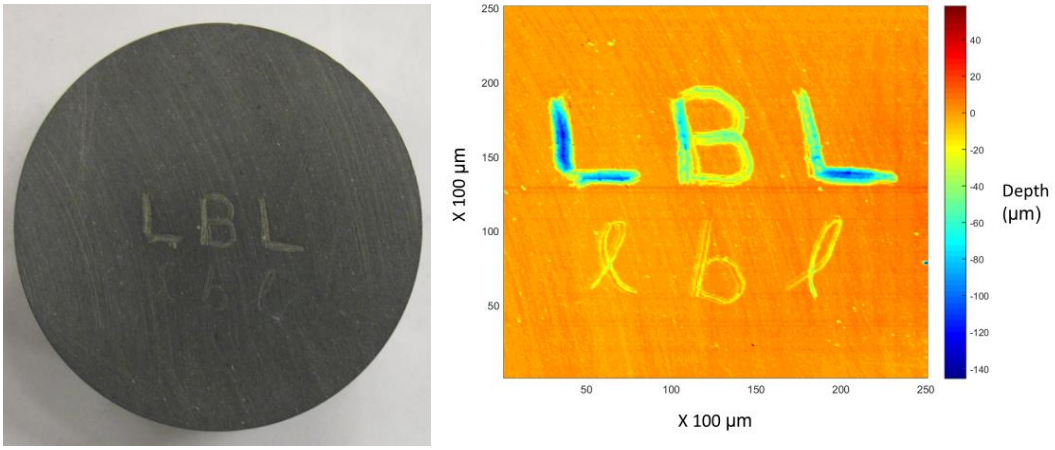

a. Letter-engraved aluminum-silicate core b. Directly scanned surface profile (via Nanovea PS-50)

Figure 2-25. Scratched test sample for demonstration

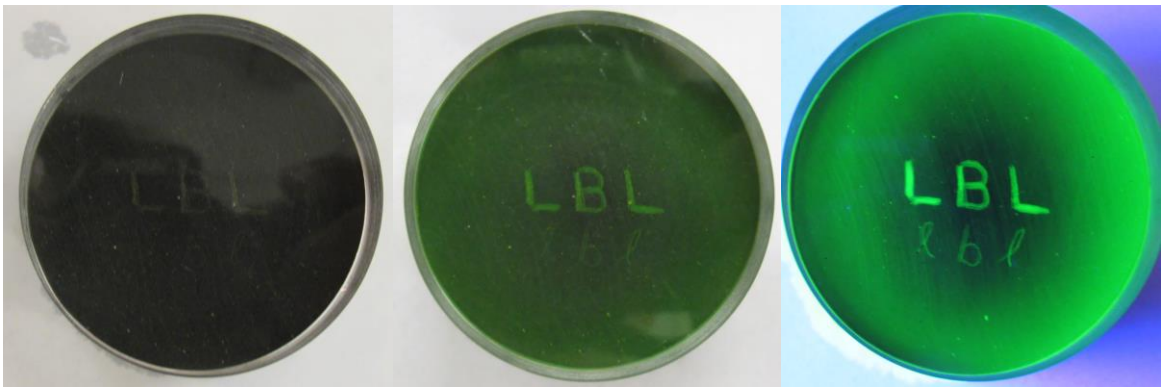

a. Cover glass only b. Filled with dyed fluid c. Illuminated by UV light

Figure 2-26. Fluorescence enhancement of a "fracture" between an etched, opaque, aluminum-silicate sample and a glass window

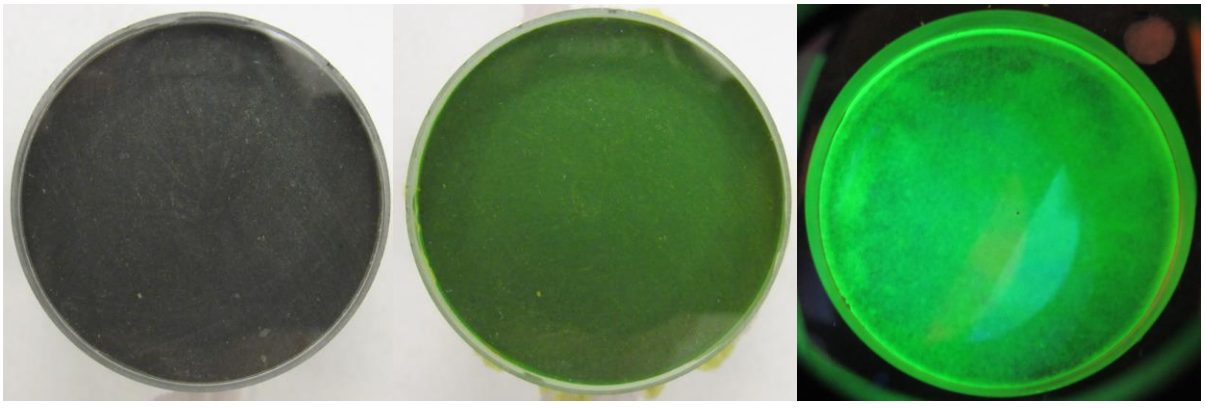

a. Cover glass only b. Filled with dyed fluid c. Illuminated by UV light

Figure 2-27. Fluorescence enhancement of a "fracture" between an opaque, aluminum-silicate sample and a sand-blasted glass window.

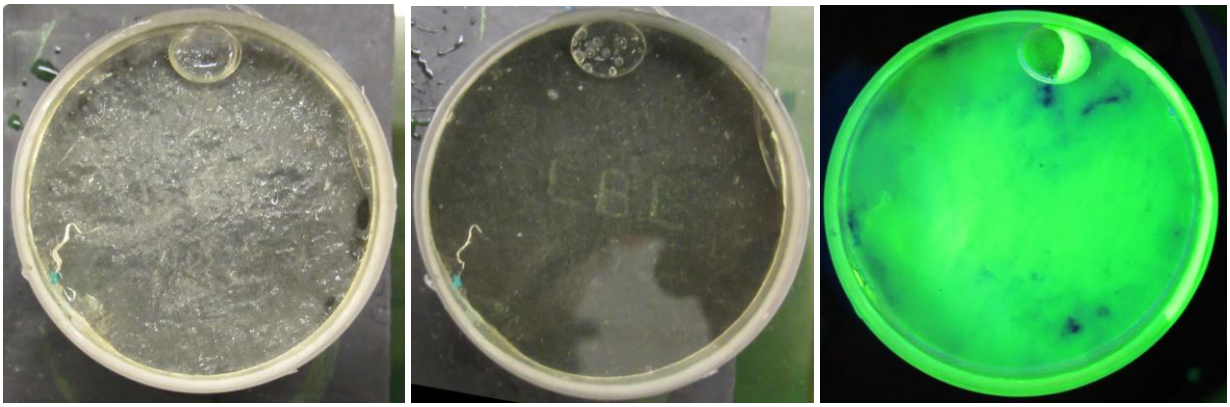

a. Cover glass only b. Filled with dyed fluid c. Illuminated by UV light

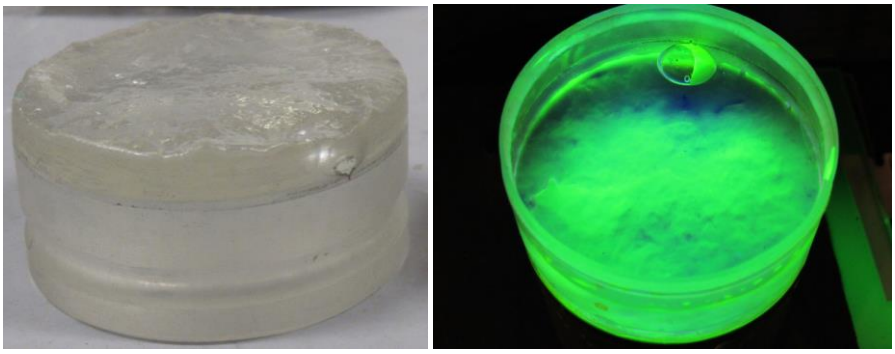

Figure 2-28. Imaging of a fracture with a very large (maximum~0.5mm) aperture. Fluorescence can visualize the location of the asperity contacts and aperture changes which cannot be seen at all when the fracture is filled with water. (Note that the opaque sample in (c) does not have letters seen in (a) and (b). Also, there is a bubble trapped in the epoxy cast of the fracture)

The fluorescence imaging can also be used for large fracture apertures as well (Figure 2-28). However, very wide parts of the aperture can be "saturated". This is partly because the dye solution is not completely transparent, and also the concentration of the dye is high (1%wt). To examine the relationships between the light intensity and the thickness of the dyed fluid, the fluid can be placed in a wedge-shaped gap between two pieces of flat glass (0.25" soda-lime glass plates)(Fig.2-29). From this example, the light intensity change is stronger (i.e., the measurement is more sensitive) for small apertures, than larger apertures. Especially, above apertures above ~150 microns, the light intensity change loses sensitivity to the aperture changes.

In conclusion, this method provides a powerful tool for imaging of a thin gap with varying thickness within a pressure vessel (with an optical window). However, the concentration of the fluorescent dye needs to be adjusted according to the thickness of the imaged fluid layer, so that the intensity change of the fluorescent light has a good sensitivity to the fracture aperture.

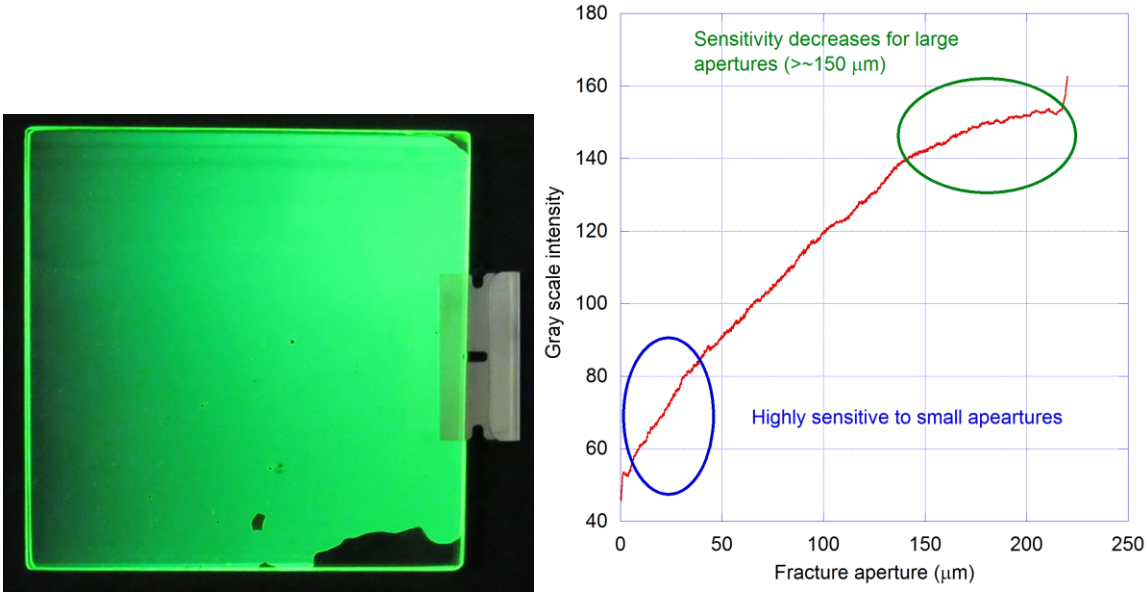

Figure 2-29. Fluorescence intensity changes over a range of "fracture apertures" formed between a pair of wedged glass plates. The plates are in contact along the left edge. The thickness of the razor blade is 220 microns.

c. Experimental System

While developing the fracture aperture visualization technique, we assembled the hydraulics and the data acquisition systems for the experiment. The system includes multiple syringe pumps, a backpressure regulator, and a transfer cylinder in addition to the main compaction cell (Figure 2-30, 2-31). Note that the injection of the dyed fluid is necessary only for fracture aperture distribution measurement, and the transfer cylinder can be bypassed to inject non-dyed fluid (brine) if necessary.

Compaction of a "fracture" between a flat shale core surface and a rough glass surface is visualized through a window at the top of the cell, using a combination of UV lighting and a camera equipped with a narrow-band filter. We have found that a 540nm, 10nm wide (FWHM) solar-continuum filter (Baader Planetarium) works quite well to capture the green fluorescent light while rejecting other lights including UV. During an initial system performance check, we found that the combination of the field of view (view-window diameter of 38 mm) and the available focal length of 20–30 cm in the system did not allow the use of our DSLR camera or industrial inspection cameras. For this reason, a CCD camera used for astrophotography (StarlightXpress SXVR-M25c with a color APS-C size sensor) and a 35 mm lens (Pentax-K) were used, with an adjustment to the lens-sensor distance to optimize the optical train. The images are captured remotely via a lap-top PC, using image capture software (Nebulosity 2.0). Also, the UV light source in an initially proposed experimental design, with a half mirror to guide the light into the view window, was replaced by a (UV-) microscope ring source (Scienscope IL-LED-E1UV).

The axial piston pressure and the pore pressure are controlled by two syringe pumps (ISCO pumps), with the latter via a high-sensitivity backpressure regulator (Equilibar). The axial displacement (or fracture closure) is measured using an LVDT. The pressure, displacement, fluid volume and flow, and temperature data are logged by a Keithley data logger and a laptop computer.

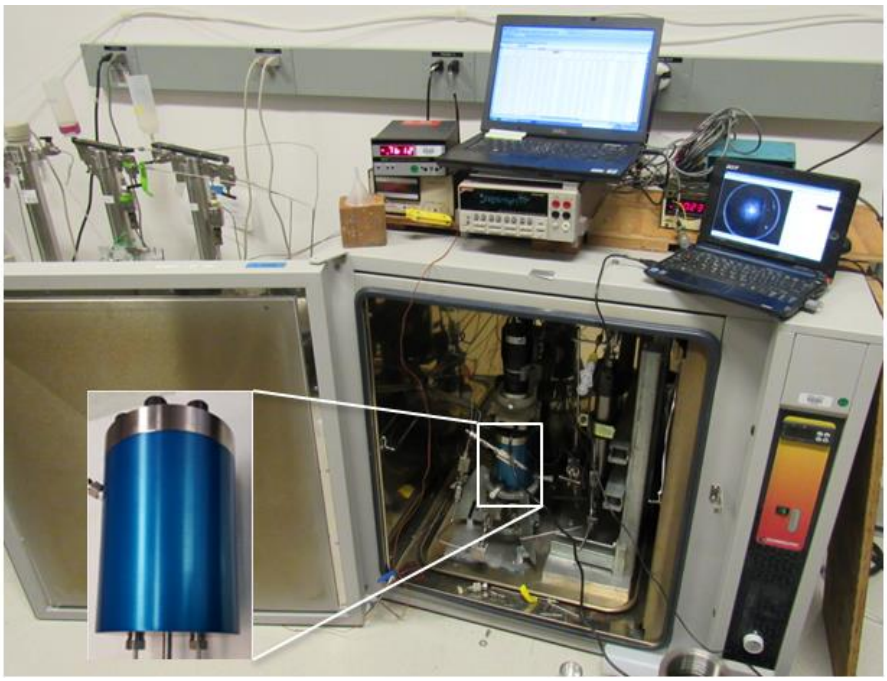

a. Experimental setup and data acquisition system

b. UV-fluorescence imaging

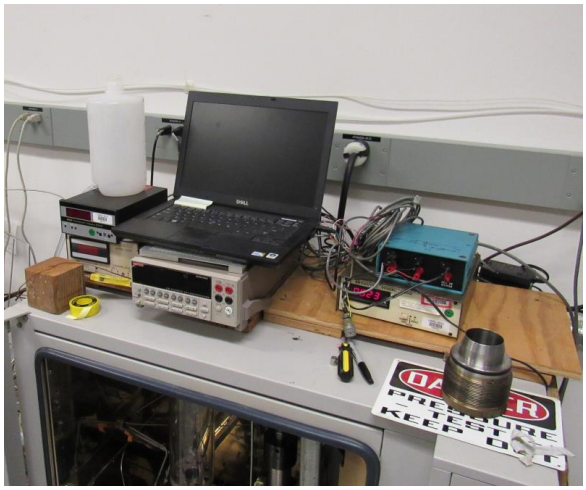

c. Data acquisition setup

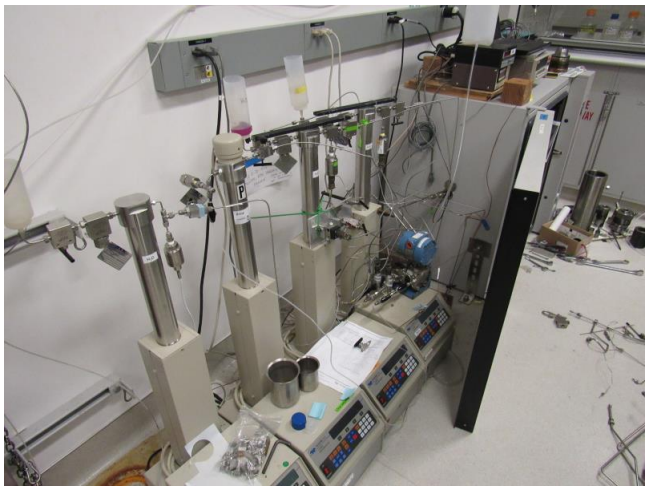

d. Pump array

Figure 2-30. Photographs of the actual experimental system. For the optical imaging of the fracture aperture distribution, fluorescent light excited by UV light is imaged using a camera lens and a CCD camera (used for astronomy).

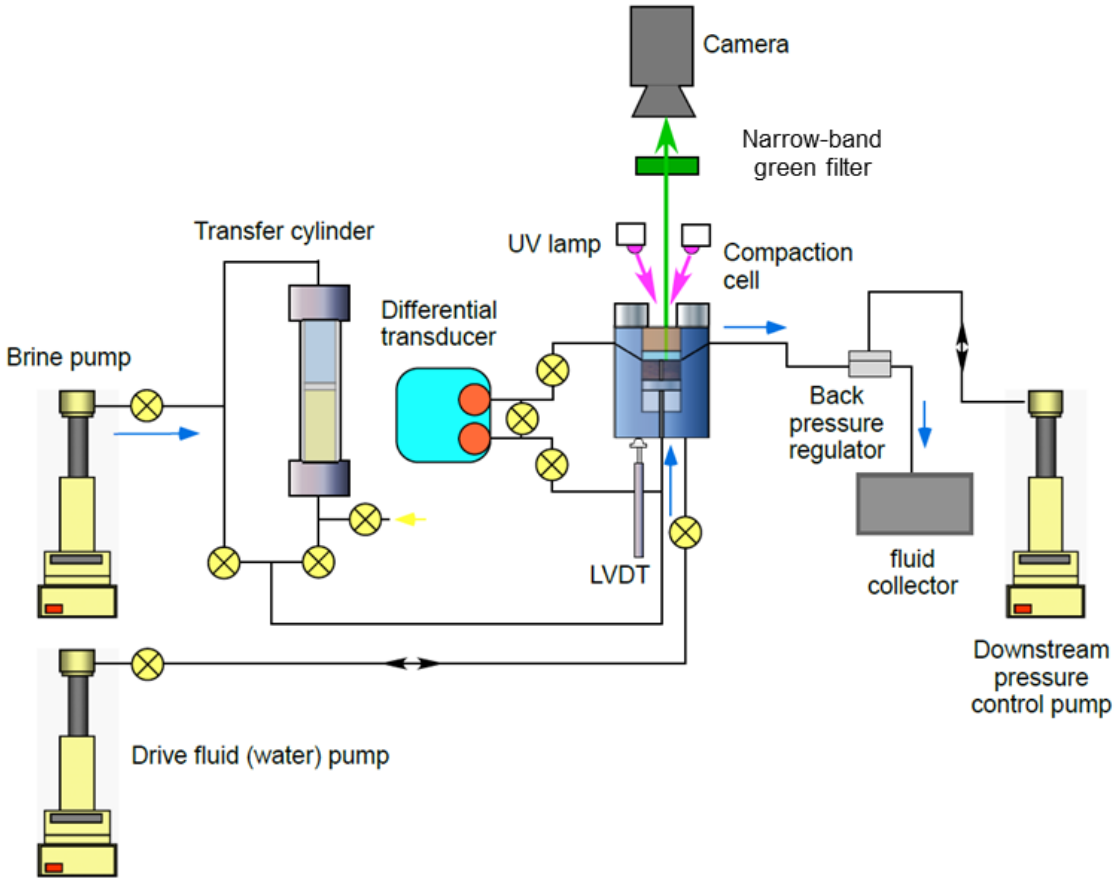

Figure 2-31. Test system diagram

2.1.4.2 Preliminary tests

In the core-scale shale fracture compaction experiments, shale fractures are closed under elevated effective confining stress, and the resulting aperture reductions and decreases in the hydraulic permeability (conductivity) are monitored over an extended period of time. Concurrently, the spatial changes in the fracture aperture are monitored through an optical view window attached to the test vessel. The images of the fracture aperture are obtained via UV-induced green fluorescence of a dye contained in the pore fluid.

The first shale fracture compaction experiment using the newly developed experimental system was conducted on a disk-shaped sample of Barnett shale. We (wrongly) expected this sample to have the highest level of clay content and exhibit the most ductility among the shale samples which we initially collected for this project (Fig.2-32). The surface of the disk was made flat and polished using a 1,500-grit sanding paper. A transparent, borosilicate disk with a sand-blasted surface was pressed against the shale sample to form an analogue hydraulic fracture with nearly mated fracture surfaces. The 3D surface profile of the glass disk and the fluorescence image of the fracture within the test cell under an effective confining stress of 20 psi are shown in Fig.2-33. Note that in this preliminary test, fracture permeability changes were determined from the pressure drops between the center of the fracture and the perimeter (i.e., a radial flow was induced in the fracture) using a differential pressure transducer.

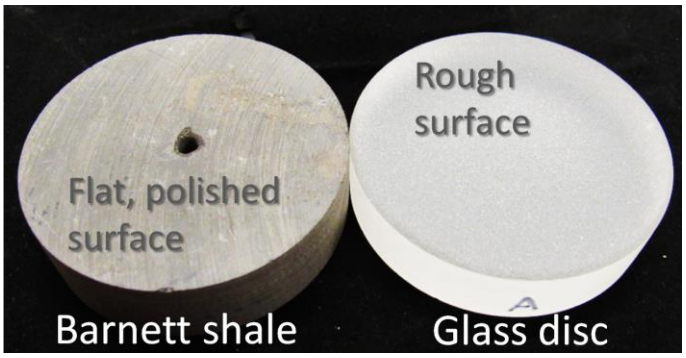

Figure 2-32. A disk sample of Barnett Shale (left) and a transparent, borosilicate glass disk with a roughened surface. The shale disk has a center hole through which brine is injected to create radial flow within a fracture (the interface between the shale and the glass surfaces).

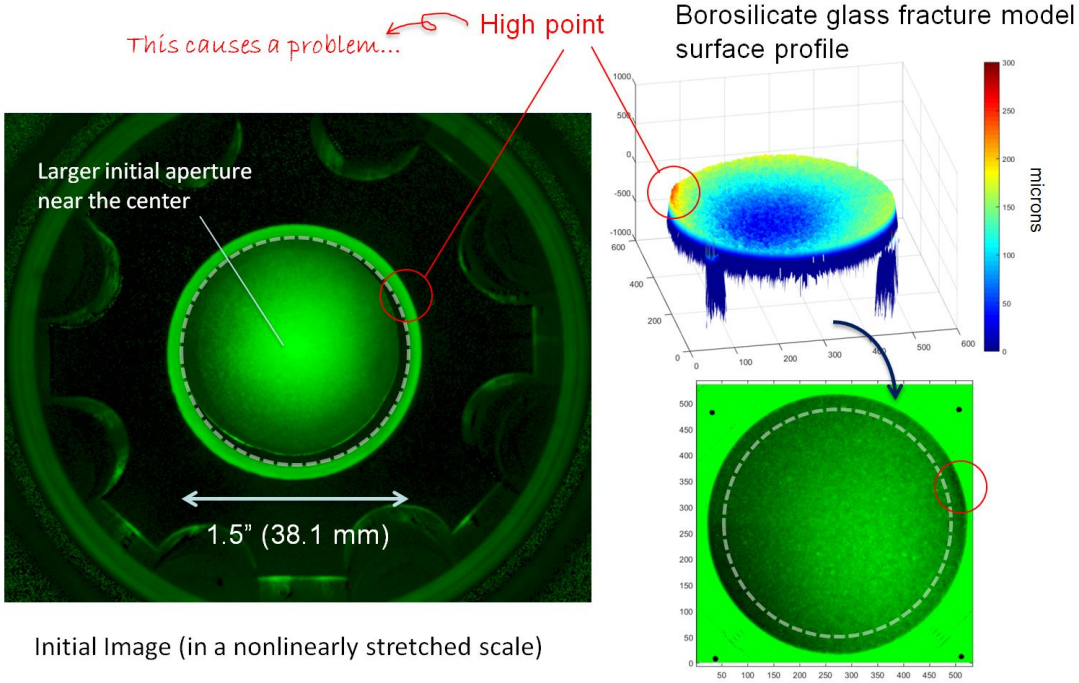

Figure 2-33. Initial (pre-loading) fluorescence image of a fracture. Because of uneven sand blasting on the glass surface, the center of the fracture has larger apertures.

During the experiment, initially, inside the test cell, a room-dry shale sample was exposed to brine (5% $NaCl_{aq.}$) over 72 hours at a pore pressure of 1,500 psi. Subsequently, while maintaining the pore pressure, the effective stress was increased by steps up to 3,500 psi. At each step, apparent fracture closure displacements (Note that this also includes deformations of the entire sample, loading platen, and the optical window parts) and the pressure drops of radial fluid flow across the center and the perimeter of the fracture were measured, and an optical image of the fracture was captured. Once the effective stress reached the target, over the following 2 weeks, monitoring of the fracture closure and permeability changes were continued. The entire test was conducted at room temperature (~25°C).

Measured compaction displacements (in red) and equivalent hydraulic aperture values of the shale fracture (in blue) are presented in Figs.2-34 and 2-35, for the initial and final effective stress change stages (Fig.2-34) and for the long-term creep compaction stage (Fig.2-35), respectively. The equivalent hydraulic aperture values were determined by assuming a radial, laminar flow of the pore fluid (viscosity assumed to be 1 cP) between a flat, rigid channel between parallel plates. Using the Cubic Flow Law, an equivalent hydraulic aperture can be computed from a measured pressure drop via

$$h = \sqrt[3]{\frac{6}{\pi}\frac{Q\eta_f}{\Delta p_f}\ln\frac{R_2}{R_1}},$$

where Q is the flow rate (0.01, 0.25, 0.5, and 1 mL/min controlled by a syringe pump [ISCO pump]), η_f is the fluid viscosity (1 cP) R_1 and R_2 are the radius of the injection hole and the outer radius of the disk sample (1/16" and 1", respectively), and Δp_f is the pressure drop.

During the initial loading (effective stress increases), the optical images indicated that cracks started to form within the glass disk (Fig.2-36). This seems to have been caused by a local stress concentration spot at the edge of the glass fracture surface model (See Fig.2-33). Although the fluorescence image in Fig.2-36 does not indicate penetration of the pore fluid into these cracks, the relatively small reductions in the hydraulic permeability compared to the mechanically measured aperture changes may be attributed to fast flow passing through these cracks. Additionally, upon inspection of the shale sample after the experiment, a few, hairline cracks were found on the shale surface. The photographs of the shale sample and the glass disk after the experiments are shown in Fig.2-37.

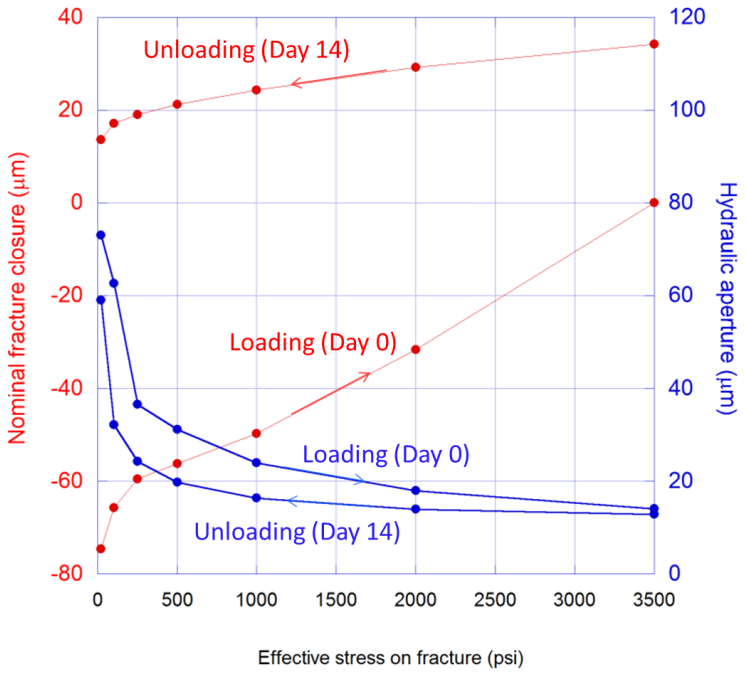

Figure 2-34. Fracture compaction (red, left axis) and the hydraulic aperture of the fracture computed by assuming that the flow within the fracture follows the cubic law (blue, right axis) during effective stress changes on the fracture.

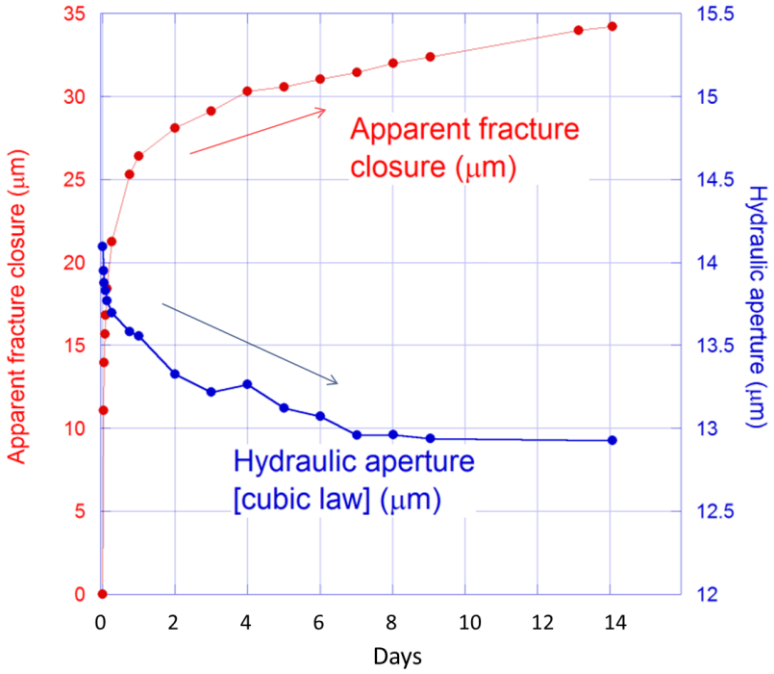

Figure 2-35. Fracture compaction (red, left axis) and the hydraulic aperture of the fracture computed by assuming that the flow within the fracture follows the cubic law (blue, right axis) during long-term loading . Although the fracture aperture keeps reducing over time, decreases in the hydraulic aperture seems to level off at a relatively high value, and the overall changes in the aperture (permeability) is small.

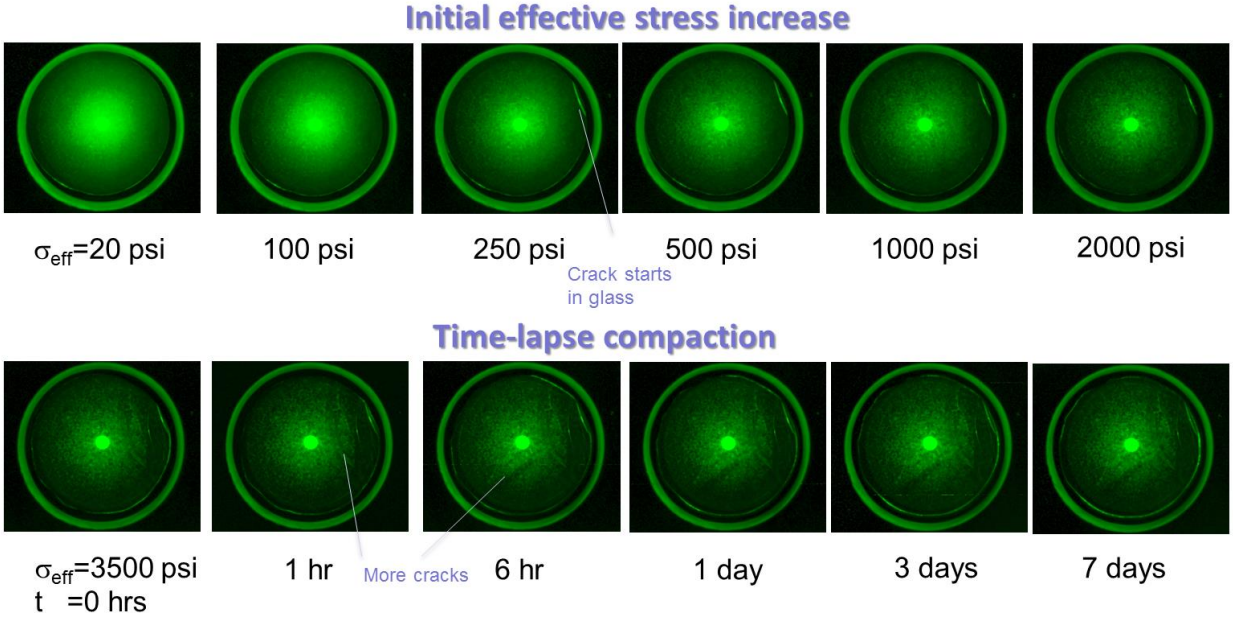

Figure 2-36. Time-lapse images of the fracture aperture changes. The aperture changed dramatically during the initial increases in the effective stress (pore pressure=1,500 psi). Subsequent long-term loading (creep loading) at a constant effective stress (3,500 psi) resulted in only small changes over time. Because of concentrated load at the edge of the glass model (Fig.2-33), the glass model fractured during the experiment.

a. Shale (before) b. Shale (after) c.Glass model (after)

Figure 2-37. Images of the shale sample and the glass fracture model before and after the experiment.

2.1.4.3 Further modifications and improvements based upon the preliminary tests

We anticipated that the cracking of the borosilicate glass disk caused by the stress concentration can happen again especially during the experiments with proppant in Subtask 2.5. Also, although it was easy to conduct the flow experiment, the radial flow geometry used in the preliminary test made the interpretation of the flow field difficult (flow rate varies across the radius, and also the flow can easily localize along a few fast paths). Additionally, the bright fluorescent light emanating from the center hole obscured the nearby aperture changes, which also made calibration of the obtained images for quantitative estimation of the fracture aperture distribution difficult. For these reasons, we made further modifications.

First, the transparent borosilicate disk was replaced by a fused quartz disk. The tensile strength of the new disk is expected to be about 7 times stronger (borosilicate tensile strength~7 MPa vs fused quartz tensile strength ~49 MPa). However because of the larger hardness of the material, sand blasting of the fused quartz was more difficult than borosilicate glass. Figs. 2-38 and 2-39 show surface profiles of sand-blasted fused-quartz glass fracture surface model and a new Barnett shale disk. Compared to the borosilicate sample in Figs.2-32 and 2-33, the new glass model is much smoother. Note that although the shale sample's surface has some large-scale topography (thanks to an imperfect hand-polishing job of the PI), the surface is much flatter and smoother at small scales compared to the glass sample. For the experiments in Subtask 2.5, an even stronger, sapphire disk was used (tensile strength of random-crystal-orientation sapphire 300-400 MPa). This is because the quartz sand gains used as proppant were expected to result in even higher stress concentration at the contacts, but having a rough surface on the fracture surface was not important for these tests.

Next, we changed the fluid flow geometry in the cell from radial flow to (quasi-) parallel flow, and also tried to prevent unwanted tensile fracturing of the shale sample. In the modified setup, the radius of a shale disk is reduced from 50.8 mm to 44.5mm, and a stainless steel ring is applied to (epoxied on) the side-wall surface. The ring has two corner o-ring grooves. The bottom o-ring prevents fast passing of fluid from the cell bottom along the side of the sample. The top o-ring has a complex shape (Fig.2-41) in order to seal the edge of the fracture from the sides of the sample and the glass disk while allowing injection and extraction of the pore fluid from the two, diametrically opposing fluid ports. A fluorescent light image of a dye plume flowing along a fracture during a test is shown in Fig.2-42.

Figure 2-38. A new, fused-quartz glass model (left) and a Barnett Shale sample with an attached (epoxied) stainless steel ring The stainless steel ring was applied to prevent tensile fracturing of the sample during the test, which is an experimental artefact due to unsupported sample side wall.

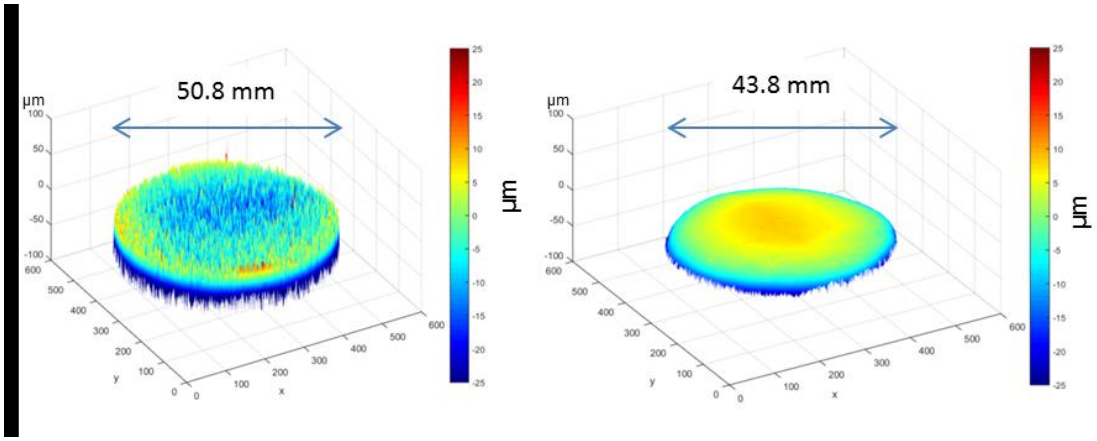

a. Fused quartz glass fracture surface b. Polished, second Barnett Shale sample surface

Figure 2-39. Surface profiles of the new shale sample and the fused-quartz glass surface.

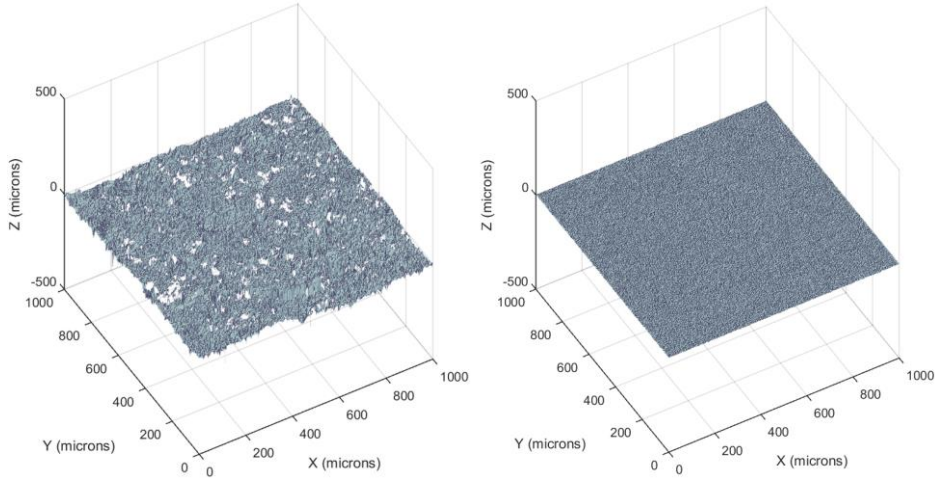

a. Fused quartz glass fracture surface b. Polished, Barnett Shale sample surface

Figure 2-40. Surface profiles of the new shale sample and the fused-quartz glass surface. Small-scale profiles over 1mm x 1mm are at the center of the profiles shown in Fig.2-10.

a. Specially designed o-ring seal

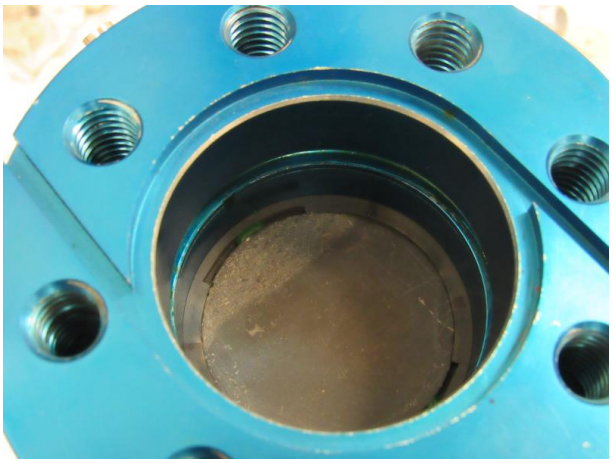

b. A rock sample and a seal installed within the visualization cell

Figure 2-41. A specially designed o-ring seal is used for conducting unidirectional flow experiments (instead of radial flow experiments) using the existing visualization cell.

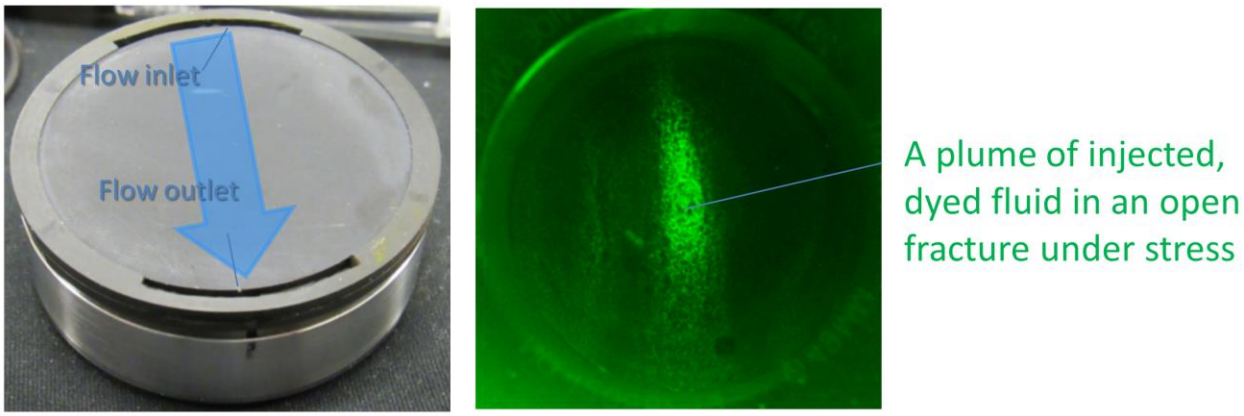

Figure 2-42. fluorescent light image of a dye plume flowing along a fracture during a compaction test.

2.1.4.4 Long-duration (~2 weeks) experiments

After the several modifications and improvements to the experimental setup and methodology, we conducted long-term (~2 weeks) compaction tests on fractures in two types of shale (+glass) samples without proppant (milestone M6). The preliminary characterization experiments conducted in Subtask 2.3 indicated a high clay content in our Barnett shale chip samples (higher than 50%), and much smaller amount was found for other shale samples including Marcellus shale (lower than 10%). Correspondingly, the Barnett shale exhibited smaller elastic moduli and high ductility, and the Marcellus shale showed large elastic moduli and smaller ductility. For these reasons, we selected these two types of shale for the fracture compaction experiments.

Barnett shale and Marcellus shale disks [diameter 44.5mm (1.75”), thickness 19.1 mm (0.75”)] with a flat, polished surface (see Figs.2-38, 2-41) were axially compressed against a quartz disk with a sand-blasted surface under room temperature. The brine used in the experiment was 5%wt $NaCl_{aq.}$, containing 1%wt of organic UV-activated green fluorescent dye WATER-GLO 801/P. The dyed brine was first introduced in the visualization cell containing a shale sample, and the pore pressure was increased up to the target pressure of 1,500 psi (10.4 MPa). The pressure was held constant over 72 hours while holding the axial stress applied to the sample equal to the pore pressure (i.e., there is no effective stress on the fracture surface). Once this is done, the axial stress (effective stress) was increased by steps. At each step, fluorescence images of the fracture were taken, and changes in the fracture aperture (nominal aperture changes including small sample and pressure cell deformation) and flow resistance were measured. The effective stress was increased up to 3,920 psi (27 MPa) over less than 1 hour, and then the test was continued for 2 weeks with periodic imaging of the fracture and deformation and flow resistance measurements between the brine inlet and outlet at the edges of the fracture.

The fluorescence images of the fractures throughout the experiments are shown for the Barnett shale sample (Figs.2-43, 2-44) and the Marcellus shale sample (Figs. 2-45, 2-46). By mapping the brightness (light intensity) of the images linearly into the depth, the captured images of fluorescence can also be used to produce three-dimensional maps of the fracture aperture (Fig. 2-47). For both fractures, increasing effective stress rapidly reduced the aperture, diminishing the brightness of the fluorescent light. Note that large brightnesses correspond to large apertures. In the figures, however, once the target stress (3,920 psi) is reached, little changes are visible in the fluorescence images.

Directly measured fracture closure displacement and the flow resistance across the fractures during the entire experimental duration (~2 weeks) are shown as a function of the effective stress in Fig.2-48. The flow rate was varied from 0 mL/min up to 1 mL/min during the test. Overall, both Barnett shale fracture and Marcellus shale fractures behaved similarly, exhibiting only small closure displacements (as little as a few microns) and hysteresis, and relatively small permeability (large flow resistance) and its large hysteresis.

The time-dependent changes in the fracture aperture and flow resistance under a constant effective stress were also similar, and both were very small compared to the overall changes during the experiments.

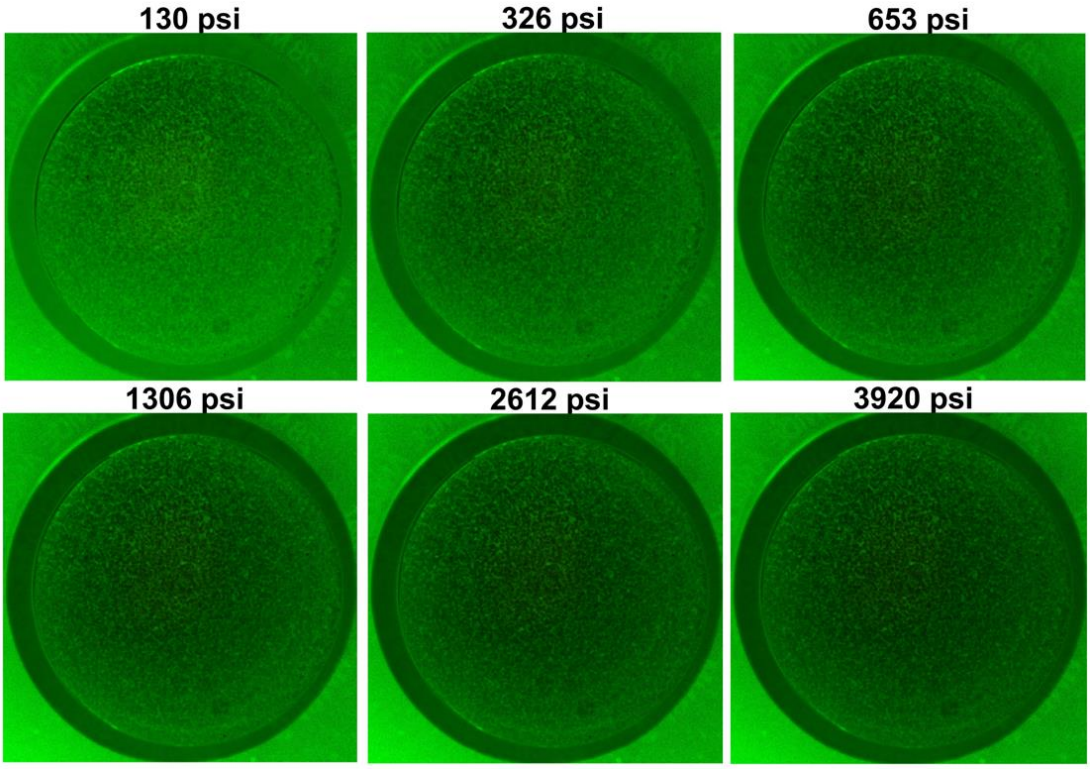

Figure 2-43. Fluorescence images of a compacting Barnett shale fracture during initial loading

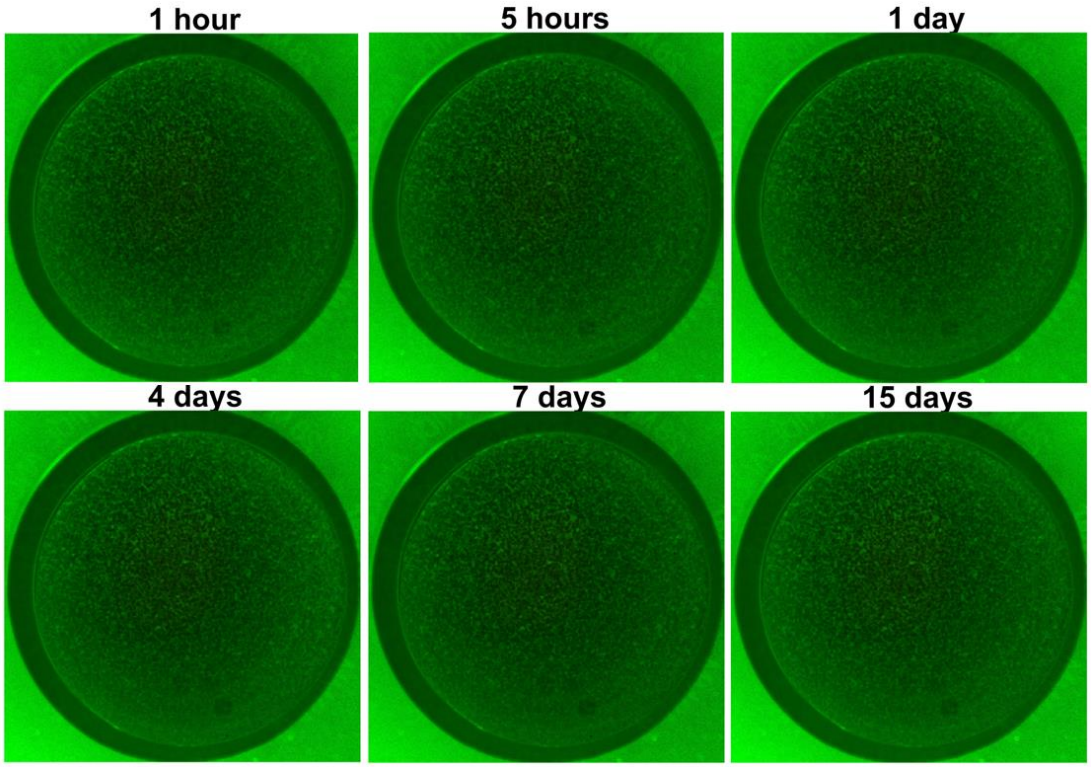

Figure 2-44. Fluorescence images of a compacting Barnett shale fracture during long-term creep under a constant effective stress (3,920 psi). The changes after the short-term closure are very small.

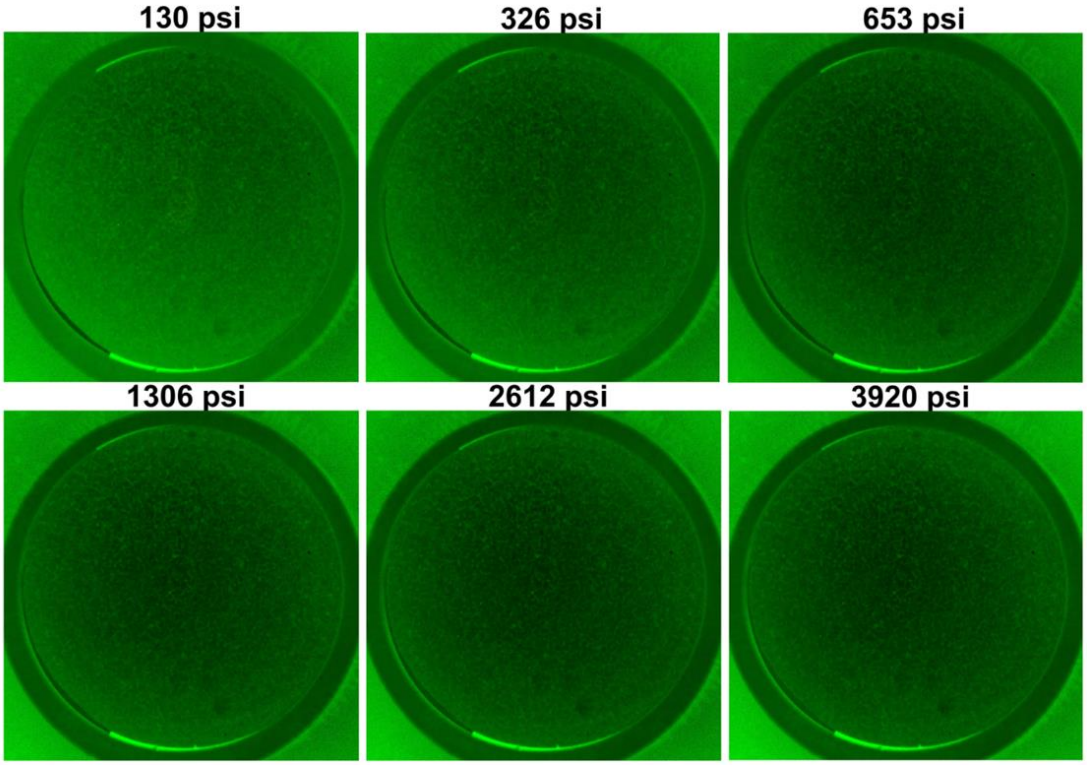

Figure 2-45. Fluorescence images of a compacting outcrop Marcellus shale fracture during initial loading

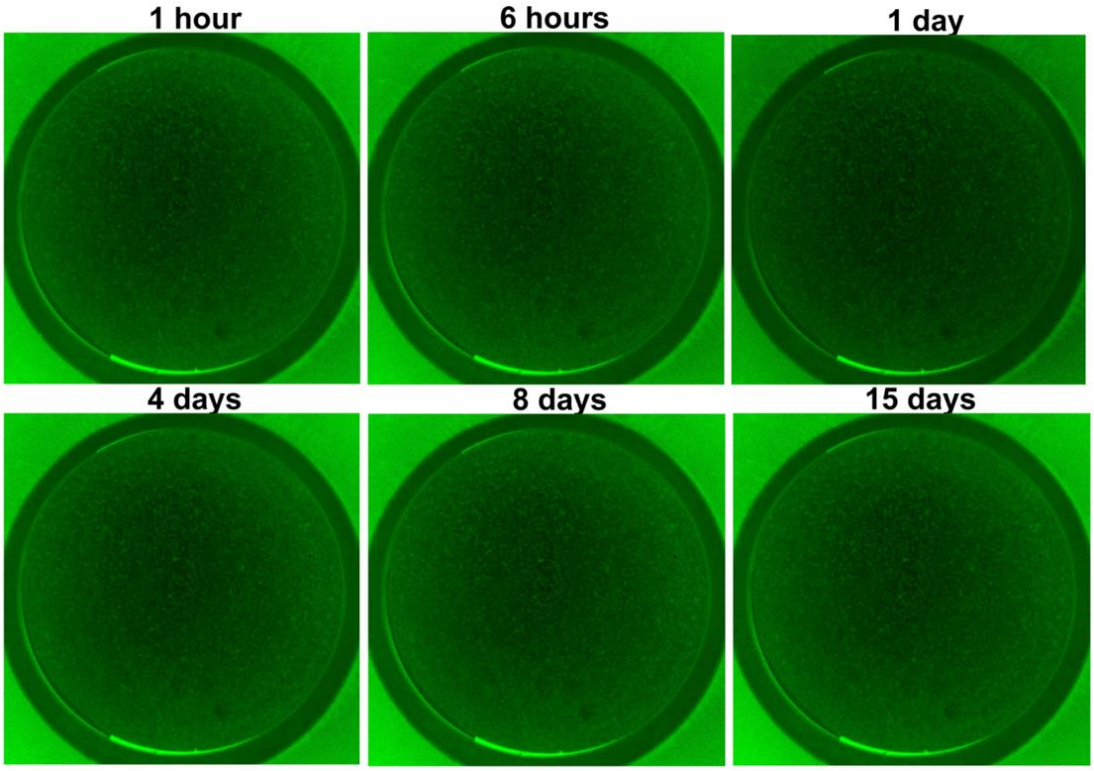

Figure 2-46. Fluorescence images of a compacting outcrop Marcellus shale fracture during long-term creep under a constant effective stress (3,920 psi). The changes after the short-term closure are very small.

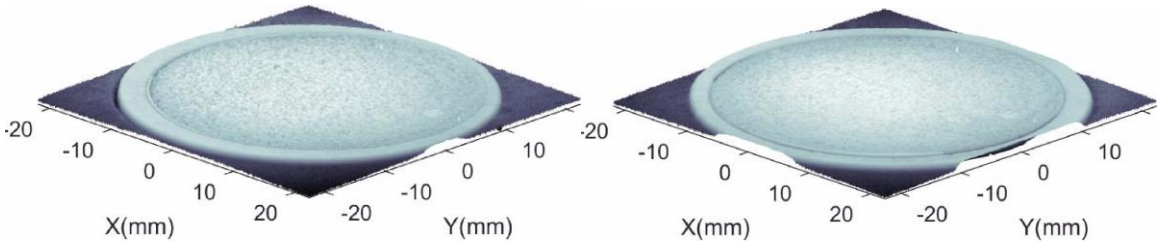

a. Barnett shale fracture (15 days)

b. Outcrop Marcellus shale fracture (15 days)

Figure 2-47. Pseudo 3-D images of the shale fractures in Figure 2-46 after 2 weeks of compaction.

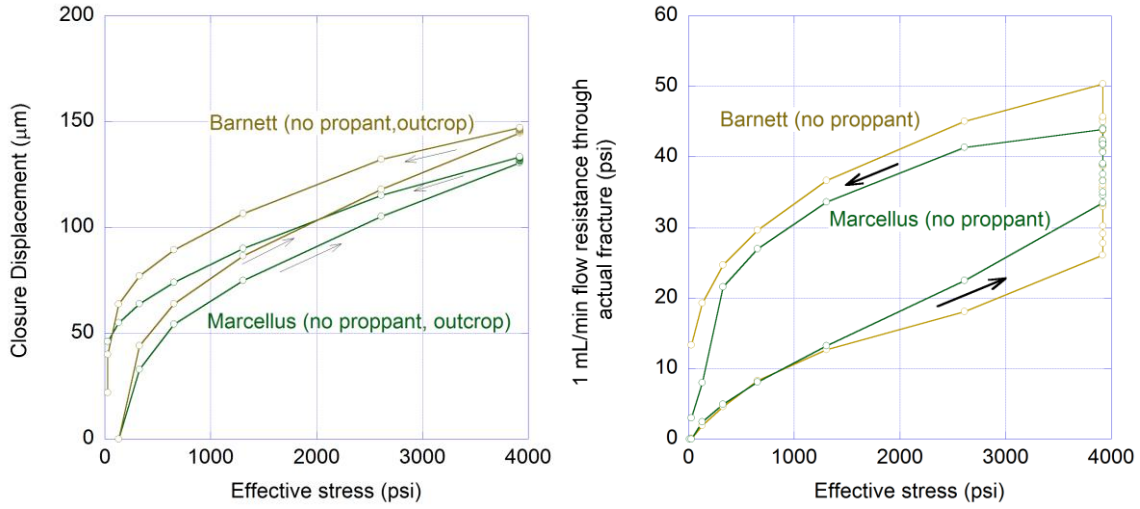

a. Closure displacement

b.Flow resistance

Figure 2-48. Fracture closure and flow resistance (1/permeability) changes during the entire experiments

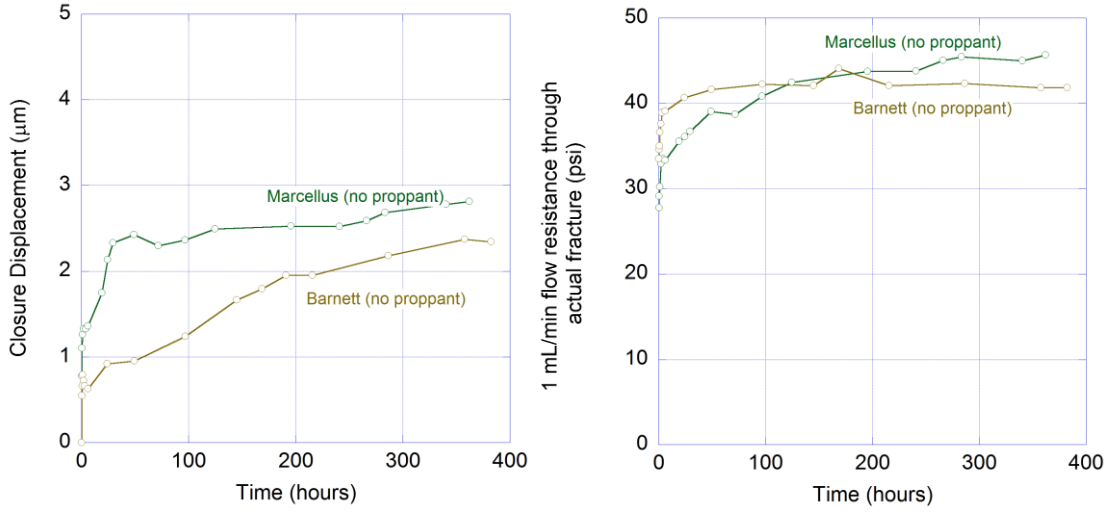

a. Closure displacement

b.Flow resistance

Figure 2-49. Creep closure displacement and flow resistance (1/permeability) changes during the long-term time-lapse experiments

Photographs of the fracture surfaces for the Barnett shale and the Marcellus shale sampled before and after the experiment are shown in Figs.2-50 and 2-51, respectively. Unlike the preliminary test, no (new) fractures developed in the rock matrix. After the experiment, both fractures exhibited “pock marks” on their surface, which were more pronounced for Barnett shale. These are tens of micron to a few hundred micron scale indentation marks (casts) from the rough, sand-blasted surface of the transparent quartz glass disk. In fact, careful comparison of Figs.2-50b and 2-51b reveals that the locations of these marks are identical for the two samples. Enlarged views of the fracture surfaces and zoomed-in views of individual indentation casts are shown in Figs.2-52 (Barnett shale sample) and 2-53 (Marcellus shale sample).

a. Before compaction b. After compaction

Figure 2-50. A disk sample of Barnett shale before (a) and after (b) a 2-week compaction experiment.

a. Before compaction b. After compaction

Figure 2-51. A disk sample of Marcellus shale before (a) and after (b) a 2-week compaction experiment.

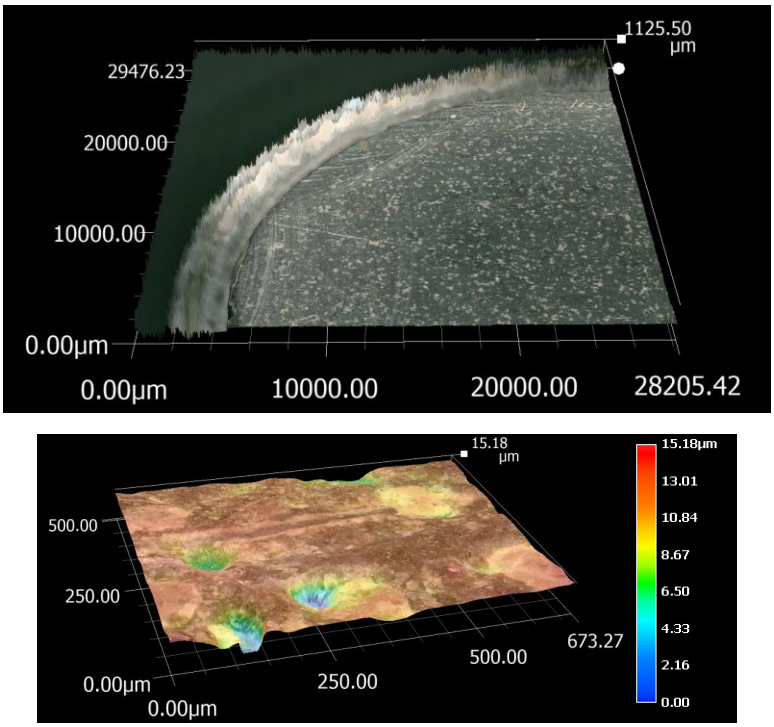

Figure 2-52. Indentation casts of the glass fracture model surface asperities on Barnett shale sample after the experiment.

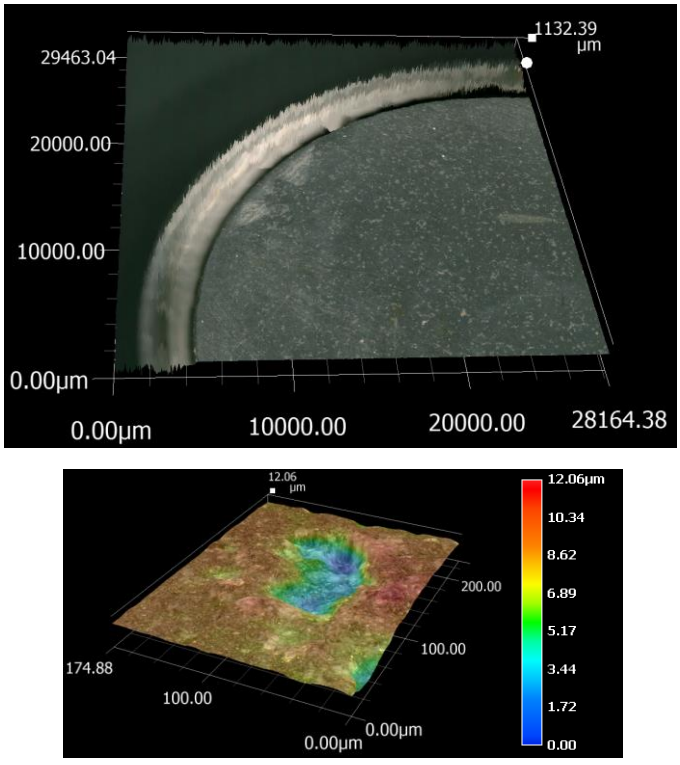

Figure 2-53. Indentation casts of the glass fracture model surface asperities on Marcellus shale sample after the experiment.

2.1.5 Subtask 2.5–Fracture closure experiment II: w/ proppant (Year 2)

For proppant-filled fractures, the overall fracture aperture was expected to be much thicker than the previous unpropped fractures. Thus, to avoid saturating the sensitivity of the fluorescence brightness to the fluid-layer thickness changes, the concentration of the dye was reduced from 1%wt to 0.1%wt. Also, because the quartz glass disk at the upper half of the sample may crack under highly concentrated load from the proppant grains, we used a sapphire glass disk with a slightly roughened surface on the proppant side. Additionally, to avoid premature cracking of the proppant grains due to the high elastic moduli and hardness of the sapphire disk, a 250-μm thick polycarbonate film was placed between the sapphire disk and the proppant layer as a stress relief.

2.1.5.1 Proppant property and its emplacement in a fracture

The proppant used in Subtask 2.5 is round, clean, quartz sand with a diameter ~1 mm (sieve size 16/20). The surface of the sand grains is smooth, and they are visually crack free. We conducted direct crushing tests on individual proppant grains held between hard, zirconia rods (compressive strength ~175 MPa) (Fig.2-55). We consider that ~28 MPa (~4,000 psi) of compression (planned effective stress during the experiments) is applied on the shale fracture with ~50% of the surface covered by a single layer of proppant. Assuming that all the proppant grains are loaded equally, from the test result, about 80% of the grains were expected to survive, at least initially. This, however, did not turn out to be the case because of slight differences in the size and geometry of individual proppant grains.

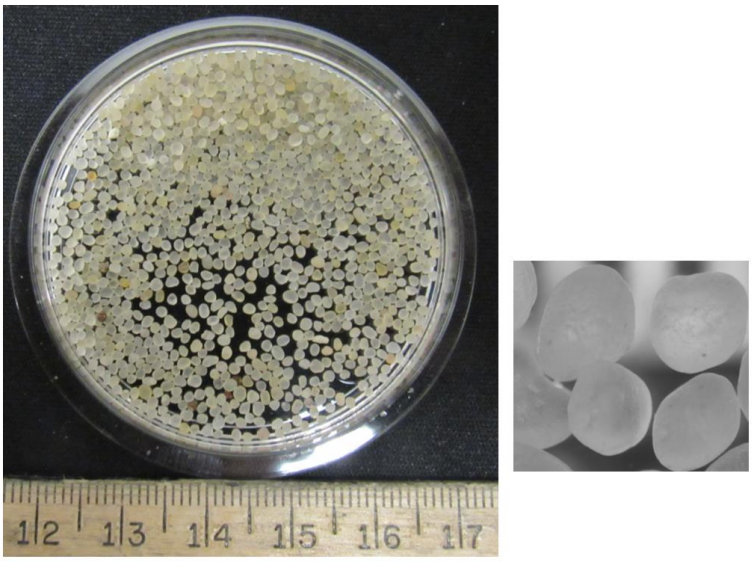

Figure 2-54. Quartz-sand proppant used for the epxeriment. The diameter is approximately ~1mm (16/20 size), and the grain shape is round and has a generally smooth surface. No obvious fractures were found in the grains.

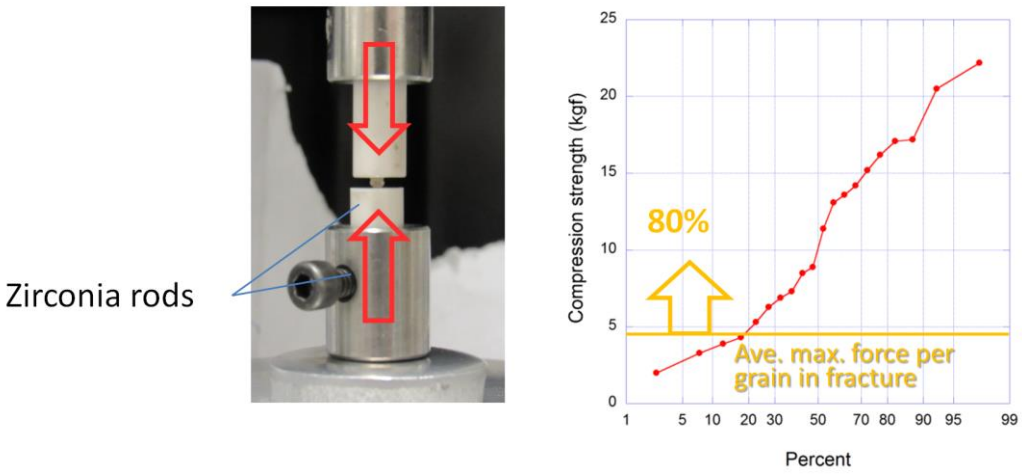

Figure 2-55. Direct crushing test of individual proppant grains held between hard, zirconia rods. According to this result, under the planned effective stress of ~4,000 psi on the shale fracture with ~50% of the surface covered by a single layer of proppant, about 80% of the grains are expected to survive (intially).

2.1.5.2 Visualization of fracture compaction in brittle shales

The experiments involving proppant-filled fractures were conducted following the same test procedure as the unpropped fractures. First, the brittle and strong Barnett shale and Marcellus shale disks [diameter 44.5mm (1.75”), thickness 18.0 mm (0.71”)] with a flat, polished surface were axially compressed against a sapphire disk [thickness 12.7mm (0.5”)] under room temperature, mediated by a proppant layer. The brine used in the experiment was 5%wt $NaCl_{aq.}$ with 0.1%wt WATER-GLO 801/P dye. The pore pressure and the maximum effective stress during the long-duration (creep) experiments were 10.4 MPa (1,500 psi) and 27 MPa (3,920 psi), respectively. The samples were first saturated by brine over 72 hours under the elevated pore pressure, and then the axial effective stress was increased by steps up to the target level. Once the maximum effective stress was applied, the monitoring of the fracture closure displacement and the stress and pressure was continued over 2 weeks, with intermittent measurements of the flow permeability (pressure drops across the fracture) and imaging of the fracture via the UV fluorescence technique.

Figs.2-56 and 2-57 show fluorescence images of a propped Barnett shale fracture, and Figs.2-58 and 2-59, a propped Marcellus shale fracture. For both samples, after the initial effective-stress-increase-induced fracture closure, the aperture changes became very small although visually detectable. More prominent behavior was the progressive crushing and relocation of the proppant grains during the early stage (Fig.2-60). Larger proppant grains failed first, transferring the load to smaller grains. Because only a small number of the grains were supporting the load due to the large stiffness and strength of the shale matrix, this sequential grain failure and load transfer resulted in crushing of a large number of proppant grains (~ 50% of the grains failed in the experiments).

(Pseudo-) 3D images of the proppant and fracture and photographs of the samples after the 2 weeks of creep tests are shown in Figs.2-61 and 2-62. These 3D images were created by inverting the luminance (i.e., black to white intensity) of the obtained fluorescence, and then mapping the intensities into the MATLAB™’s “bone” color scale from black (aperture=1 mm) to white (aperture=0 mm). Because

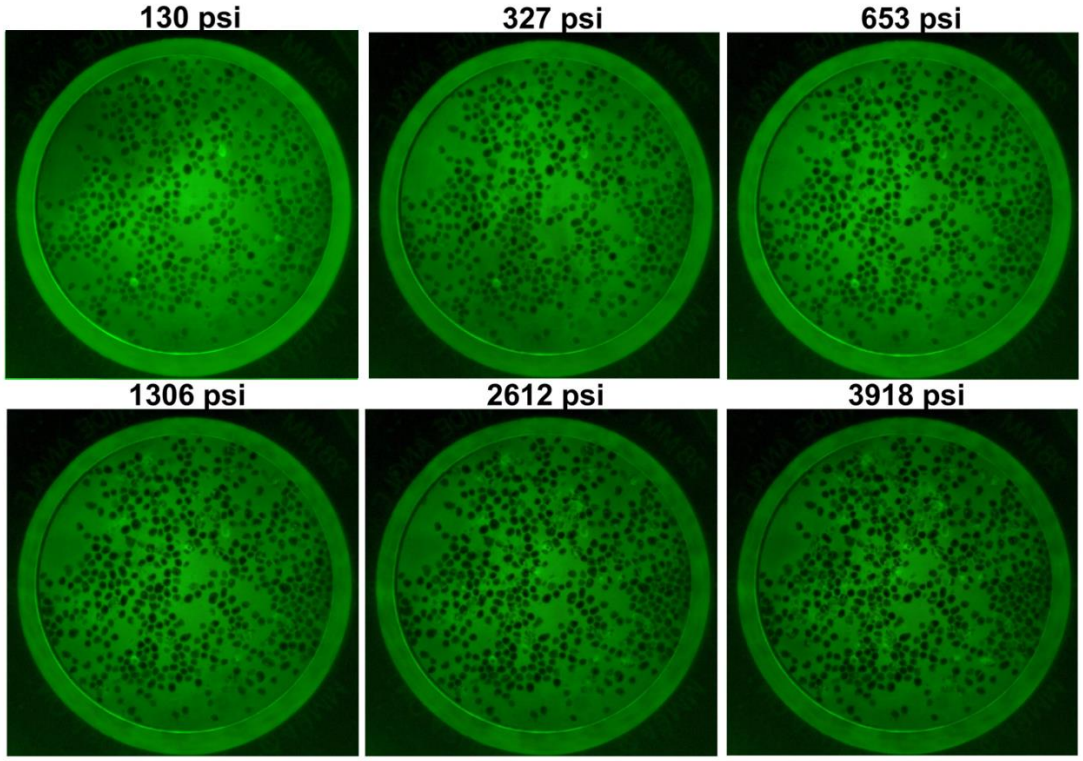

Figure 2-56. Compaction of a Barnett shale fracture containing proppant with increasing effective stress.

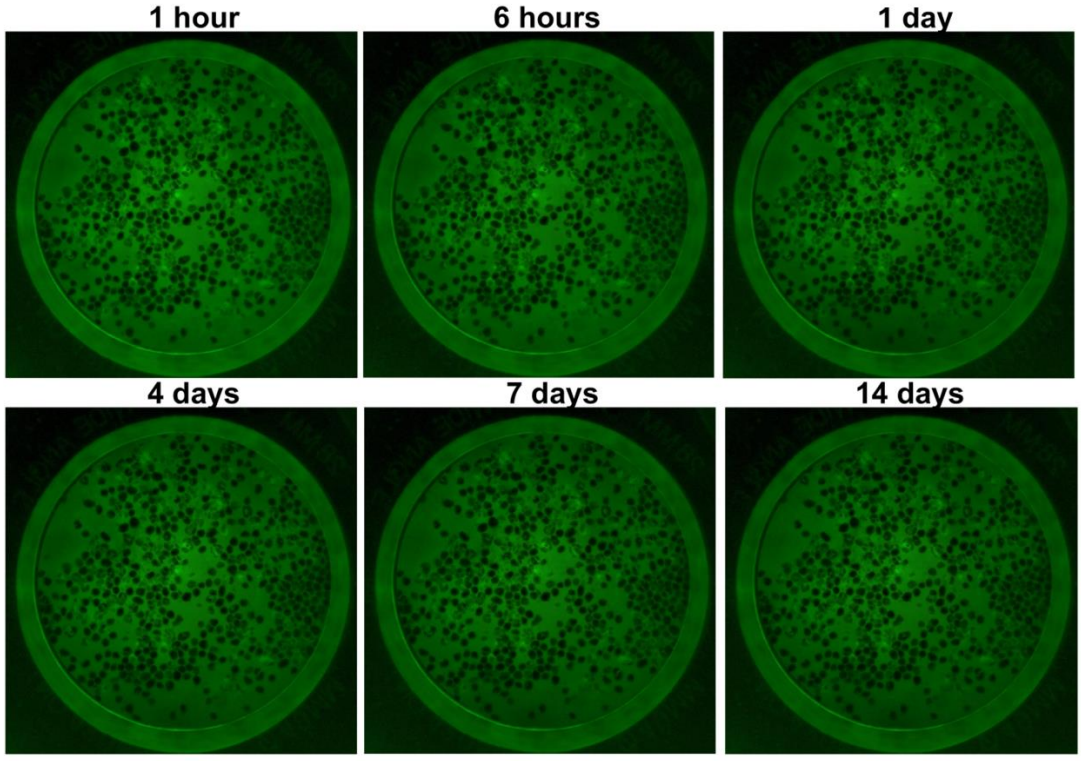

Figure 2-57. Creep compaction of a Barnett shale fracture containing proppant. Once the effective increase is stopped, the changes in the aperture (and the fluorescence intensity) became very small.

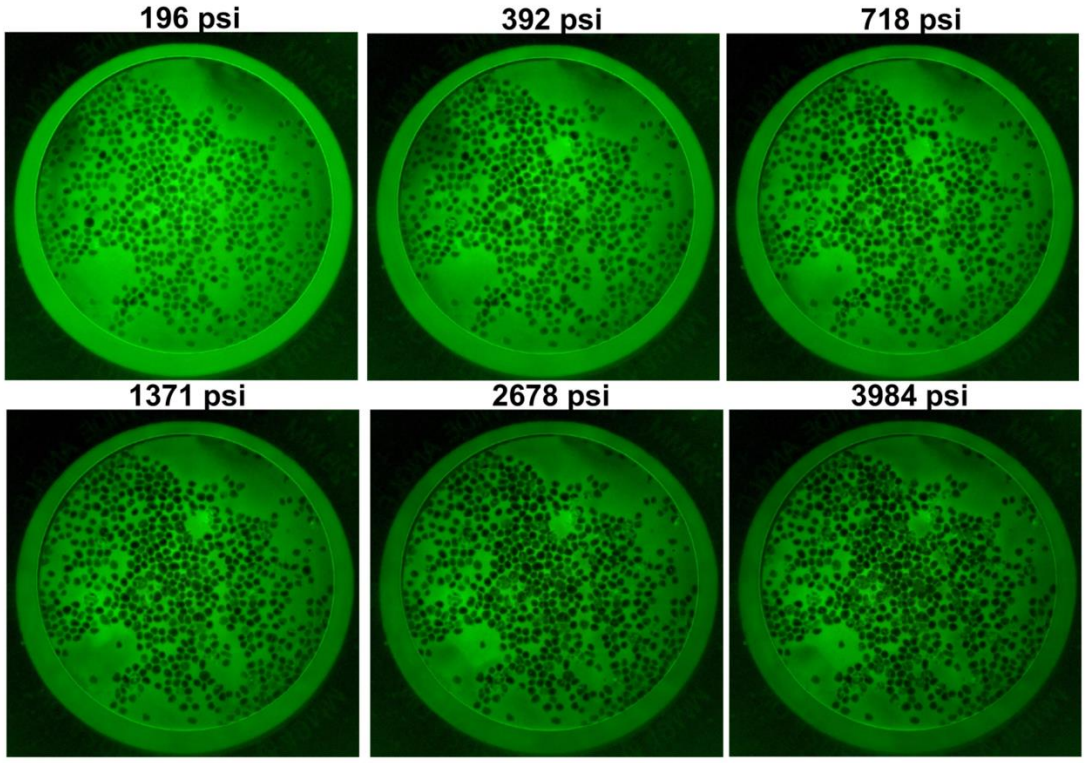

Figure 2-58. Compaction of a Marcellus shale fracture containing proppant with increasing effective stress.

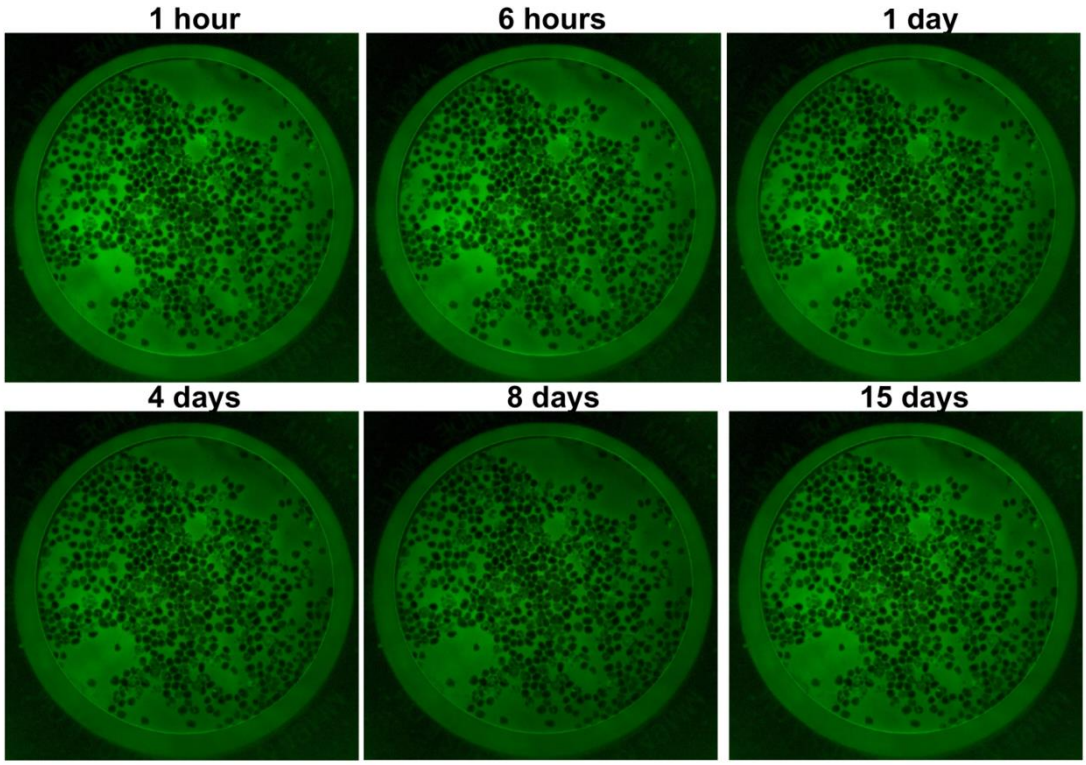

Figure 2-59. Creep compaction of a Marcellus shale fracture containing proppant. Once the effective increase is stopped, the changes in the aperture (and the fluorescence intensity) became very small.

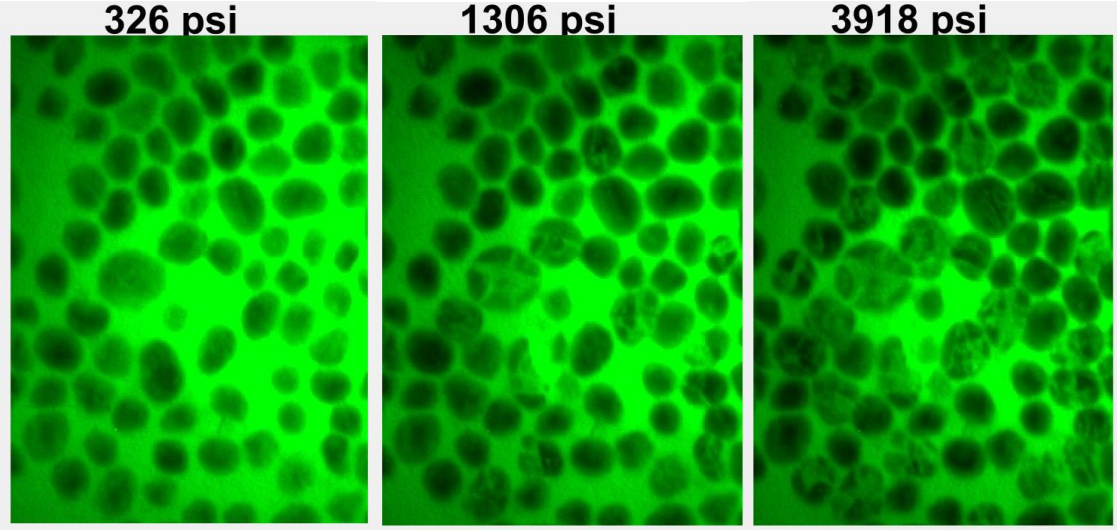

Figure 2-60. Progressive proppant crushing (fracturing) was observed for both Barnett and (outcrop) Marcellus shale samples during the initial increases in the effective stress. Here, only zoomed-up images for the Marcellus shale are shown. A three-dimensionalized image for the highest effective stress (3,918 psi) is shown on the right.

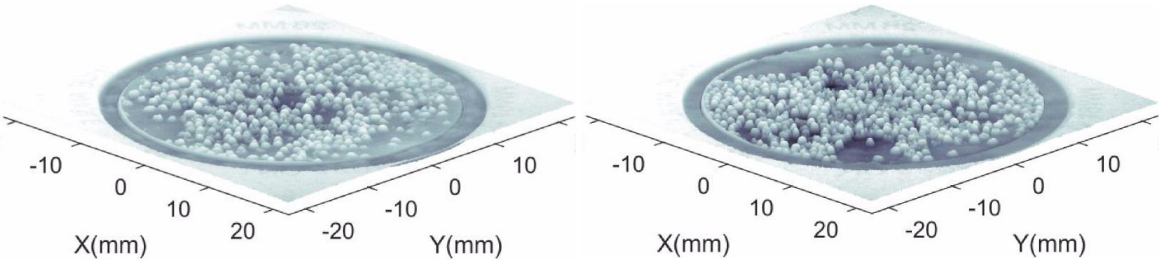

a. Barnett shale fracture (15 days) ***b. Outcrop Marcellus shale fracture (15 days)***

Figure 2-61. Pseudo-3D images of the samples at the end of the 2-week-long compaction experiments. Except for the crushed proppant grains, embedment of the proppant grains is not evident.

a. Barnett shale b. Marcellus shale

Figure 2-62. Photograph of the surfaces of the shale samples after the experiments. Shallow, but clear indentation marks (casts) from the proppant grains can be seen.

of imperfect image processing (particularly for difficult flattening of the imaged field and removal of reflections in the optical train of the imaging system), errors are visible especially as a warped (non-flat) shale sample surfaces. In spite of the observed small fracture deformation, photographs of the shale sample surfaces after the experiments (Fig.2-26) do show clear indentation marks (casts). Visibly, these marks are more prominent for the Barnett shale sample compared to the Marcellus shale sample.

Microscope images of the sample surfaces are shown in Figs.2-63 and 2-64 for the Barnett shale and Marcellus shale samples, respectively. These images indicate that the proppant casts are generally very shallow (tens of microns or less) and irregular in shape. In many cases, this irregular proppant cast geometry can be attributed to the embedment of crushed proppant grains with sharp edges. The seemingly higher degree of embedment for the Barnett shale sample appears to be due to the bright texture of broken and exposed shale matrix resulting from indentation, because the microscope observation does not show any significantly deeper proppant casts that the Marcellus shale sample.

One interesting observation is the lack of tensile fractures underneath the proppant grains in the shale matrix. It appears that even though the shale matrix is hard and brittle, indentation by the proppant grains resulted primarily in compaction and shear failure of the rock (and of course, proppant grain crushing) rather than tensile fracturing. An exception, however, is the case when a proppant grain is located near the edge of the fracture surface. Because of the presence of an unsupported free side wall (although there is some stress applied by an o-ring), tensile fractures do start from an indentation cast, propagating parallel to the side wall (Fig. 2-64 bottom right).

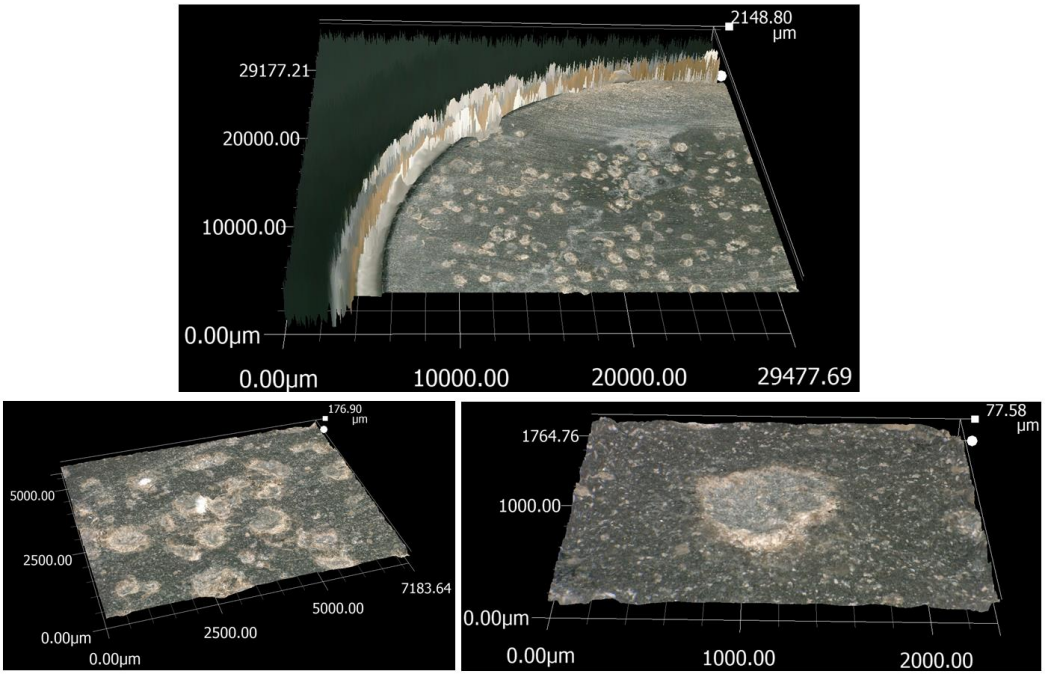

Figure 2-63. Microscope images of the sample and proppant casts. In spite of the first appearnce, the proppant casts are all very shallow. Barnett samples for some reasons tend to exhibit surface damage more cleary than the Marcellus shale sample.

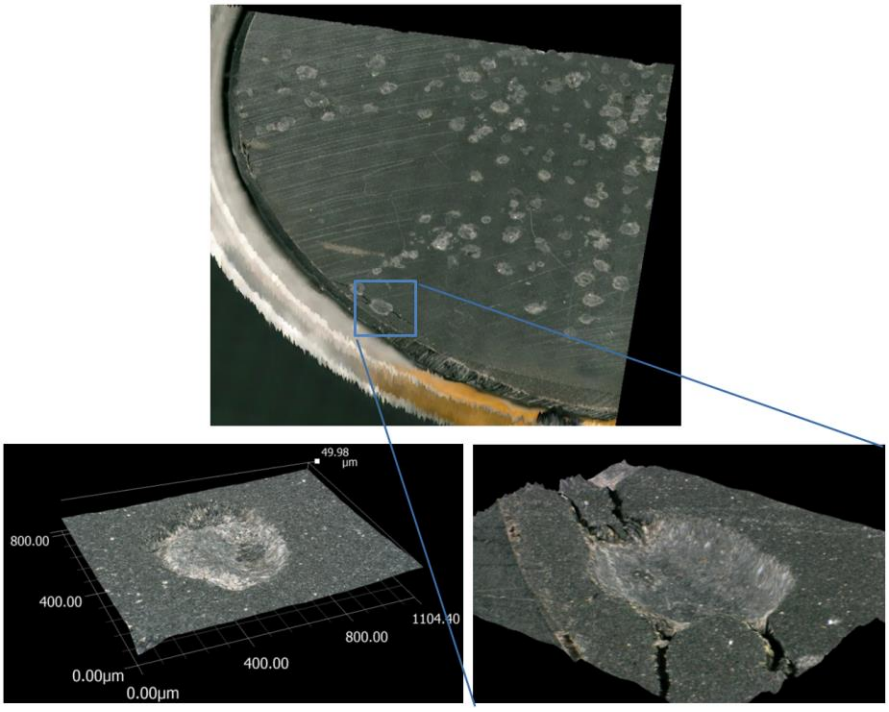

Figure 2-64. The proppant casts often exhibit surface damage caused by sharp edges of broken proppant grains (bottom left). Generally, proppant peneration did not cause fracturing of the shale samples. An exception is when a grain is located near the edge of the sample surface where the presence of unsupported boundary resulted in tensile fractures parallel to the edge wall.

2.1.5.3 Visualization of fracture compaction in ductile shales

As mentioned in Sections 2.1.2.2 and 2.1. 3.3, the Barnett shale core samples we originally considered ductile (i.e. clay rich) did not turn out to be the case. Therefore, instead, we used a Marcellus shale core obtained from the MSEEL project and a Pierre shale outcrop core, which both exhibited large ductility.

Possibly because of the high clay contents (both with ~50% clays), both cores contained tensile fractures which made the preparation of the samples for our compaction experiment difficult. For the MSEEL core, open fractures in a large, field core were filled with low-viscosity epoxy (mixed with 0.1%wt fluorescent dye Sulforhodamine B) before it was sub-cored. For the Pierre shale, the provided outcrop core was already shaped as a 2-inch diameter, 2-inch height cylinder. For both samples, in order to avoid disturbing the fragile, fractured matrix, a PVC heat-shrink jacket was applied to the cores while trimming the core diameter and the length to produce disk-shaped samples necessary for the experiment.

The experiments were conducted following the same procedure as the brittle shale samples. For Marcellus/MSEEL shale, the duration of the creep test was extended up to 1 month (31 days). Figs.2-65 and 2-66 show fluorescence images of a propped Marcellus shale fracture. Because the intensity of the fluorescent light varied significantly during the experiment, the brightness had to be adjusted for distinguishing the changes occurring during the creep tests. This resulted in the partially saturated brightness of the images for the lowest effective stresses in Fig.2-65. From these images, only a small number of proppant grains are seen crushed during the initial effective stress increases. At high effective stresses and during creep compaction, the open space between the proppant grains show darkening, indicating that the embedment of the proppant grains caused heaving of the shale matrix. The reductions in the fluorescence intensity continued over 1 month. Strangely, however, the image taken on Day 31 shows brighter intensities than Day 29. If aperture reductions alone were responsible for the brightness change, this would not have happened. Upon close inspection, we also realized that there was a significant degree of irregular fluctuation in the brightness of the images taken over 1 month.

During the post-experiment examination of the sample, we observed that the proppant embedment produced fine-grained debris which made wash water used on the sample surface turbid. This led us to wonder if the darkening of the fluorescence during the experiment was caused by the increased turbidit of the brine. As a part of the visualization experiment, on Day 31, brine without the fluorescent dye was injected at a rate of 1mL/min into the fracture to purge out the dye-containing fluid, then fresh brine containing dye was reinjected (Fig.2-67). This experiment resulted in initial brightening of the fluorescent intensity (Drainage 50 s) before the image became dark for the lack of the dye in the system. Once the fresh brine and the dye were injected, the result image became brighter than the initial state. Additionally, the image at “Drainage 50 s” revealed a plume of fine particles being discharged from a section of densely packed proppant (and crushed shale matrix). These observations prove that the observed darkening of the images (especially after 2 weeks) was at least partially attributed to the clouding of the brine, and that a significant degree of shale matrix fracturing and debris production was caused by proppant embedment for this shale.

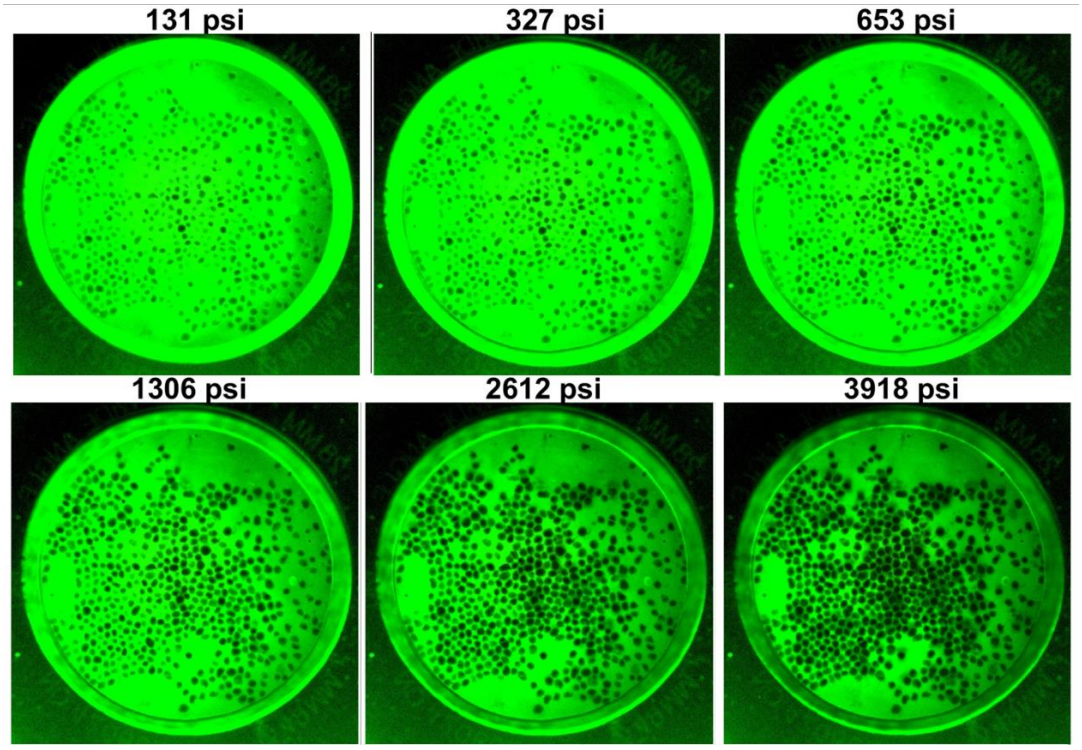

Figure 2-65. Compaction of a Marcellus (MSEEL core) shale fracture containing proppant with increasing effective stress. The initial images are oversaturated so that the images after the target effective stress are not too dark. Only a small number of proppant grains were crushed

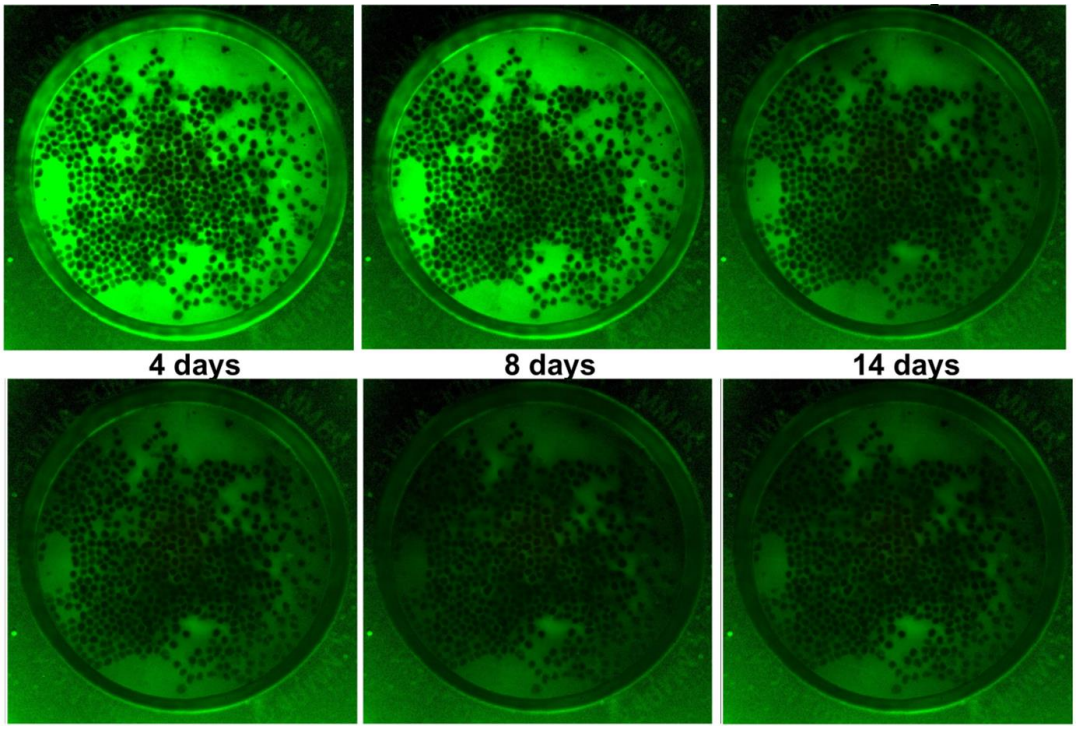

Figure 2-66. Creep compaction of a Marcellus (MSEEL core) shale fracture containing proppant. Fracture closure and darkening of the fluorescent light continue with time. Note that however, there is a sudden increase in the brightness between Day 29 and Day 31.

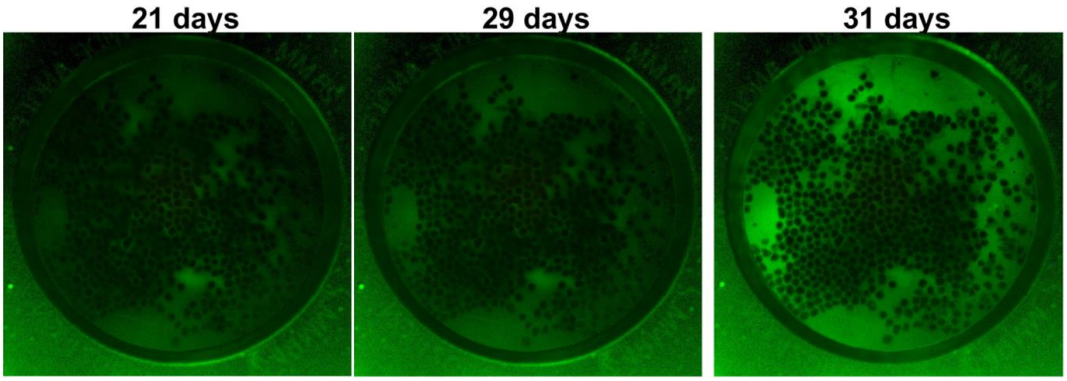

Figure 2-66. (Continued)

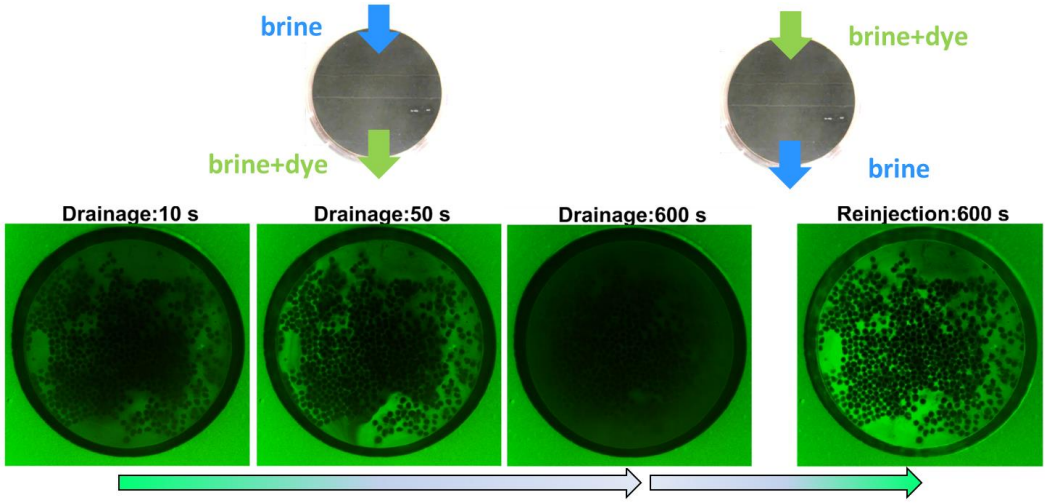

Figure 2-67. On Day 31, after an initial image was captured, 5% NaClaq brine without the fluorescent dye was injected to purge out the dyed brine. This resuled in initial temporary brighteneing of the fluorescence, followed by darkening. After reinjection of fresh dyed brine, the overall image brighness increased significantly. Also note that for T=50 s, there is a dark plume (cloud) of particles streaming from a zone with high proppant density.

Next, Pierre shale sample was tested. The duration of the creep test was 2 weeks (15 days). Figs.2-68 and 2-69 show fluorescence images of a propped Pierre shale fracture for increasing effective stress and for the subsequent creep test, respectively. Similar to the MSEEL sample, the brightness of the images for the lowest effective stresses is partially saturated. For this experiment, no proppant grain failure was observed. At the end of the effective stress increase test (Fig.2-68), there was already a significant degree of shale matrix heaving and debris formation around the proppant grains. As indicated by the darkened zones in the fluorescence image, the aperture reduction occurred preferentially along the top, right, and then the bottom circumference of the fracture surface.

It is interesting to note that, similar to the MSEEL sample, the reduction of the aperture seems to have happen betweened the proppant grains first, followed by closure of the fracture surfaces unsupported by the proppant. The latter behavior was more prominent during the creep phase of the experiment, especially near the flow inlet (top in each image) of the fracture (Fig.2-70). Once the surfaces of the shale and the sapphire glass (mediated by a polycarbonate film) around the inlet and the outlet came into contact, permeability of the fracture was lost.

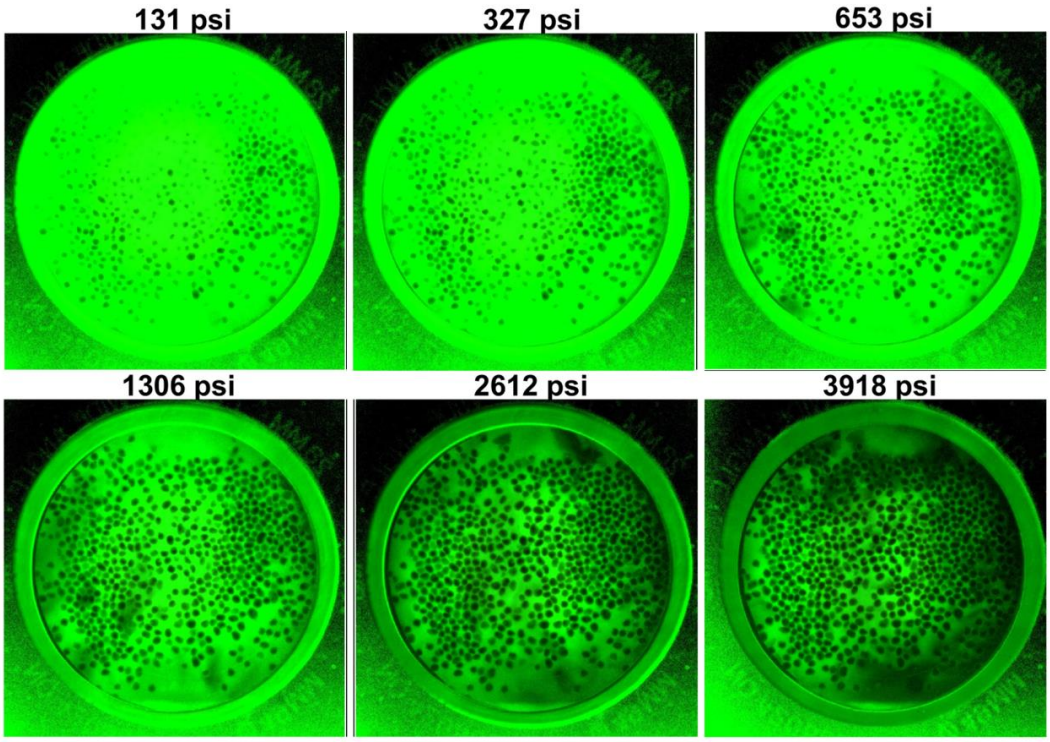

Figure 2-68. Compaction of a Pierre shale fracture containing proppant with increasing effective stress. The initial images are oversaturated so that the images after the target effective stress are not too dark. No proppant graine crushing was observed.

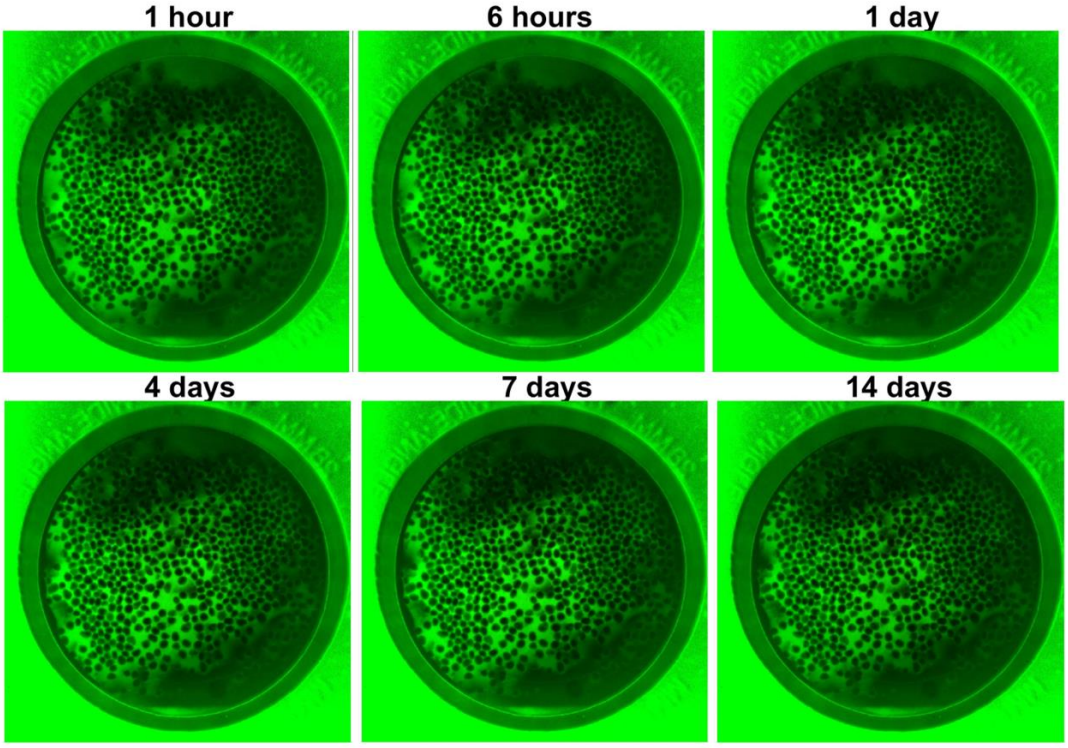

Figure 2-69. Creep compaction of a Pierre shale fracture containing proppant. Fracture closure and darkening of the fluorescent light continue with time. Fracture closure occurred primarilly along the top-right sample edges.

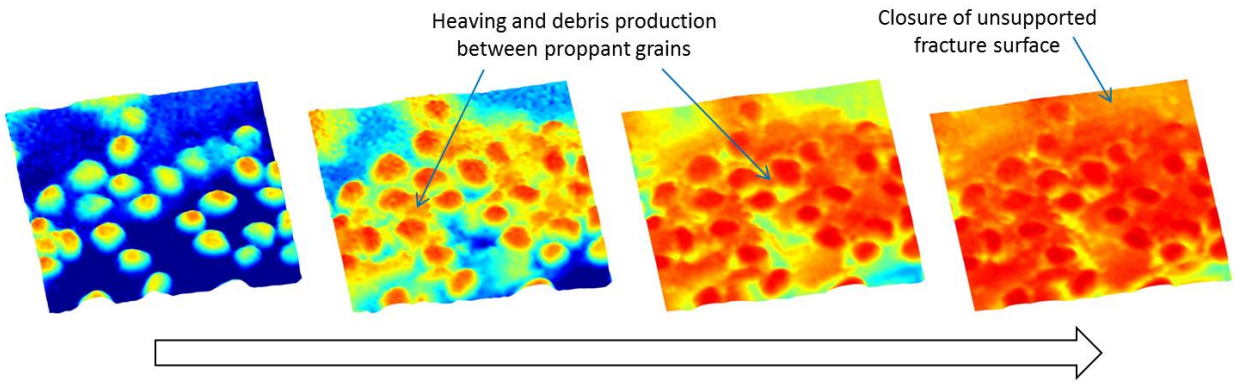

Figure 2-70. Colored 3D images of a section of the fracture in Fig.2-68. Red color indicates closed surface. The fracture initially closes between proppant grains due to indentation-induced heaving and debris production, followed by creep closure of the unsupported section of the fracture.

(Pseudo-) 3D images of the proppant and fracture and photographs of the samples after the experiments are shown in Figs.2-71 and 2-72, respectively.

Unlike the brittle shales, the changes in the aperture from ductile shale matrix deformation are clearly seen in the 3D images. Particularly, for the Pierre shale fracture, the apertures near the inlet and outlet are completely closed. The preferential closure may be partly attributed to the low proppant density near the fluid ports, which caused higher stress concentration around the proppant grains and accelerated the embedment, as well as to the larger area of unsupported surface.

The photo images of the samples after the experiments (Fig.2-72) show severe embedment (casts) of proppant grains. In addition, a large amount of material was lost during cleaning of the fracture surface of the shale debris and loose proppant grains after the experiment.

Microscope images of the sample surfaces are shown in Figs.2-73 and 2-74 for the Marcellus/MSEEL shale and Pierre shale samples, respectively. The MSEEL shale sample exhibits severe damage (fracturing and pulverization) of the shale matrix in addition to well-defined proppant casts as deep as a few hundred microns. The Pierre shale sample shows the most severe proppant embedment (indentation depth up to ~1mm), but the pulverization and microfracturing was not as prominent as MSEEL sample. The sample surface exhibits a “muddy puddle” look, and completely embedded and trapped proppant grains can also be found. It appears large-scale tensile fractures did form in and around the proppant casts. However, in many cases, these fractures are difficult to distinguish from desiccation-induced fractures during the microscope observation and imaging.

The differences in the proppant embedment behavior between the two ductile shales are attributed to the constituent clay types (note that both shales have similar overall clay content, and the Pierre shale sample here has a large amount of smectite) and, possibly, to the location of the clays with respect to the quartz/feldspar grains. At this point, however, we have not studied the mineral-grain-scale structure of the shale samples to examine the latter mechanism.

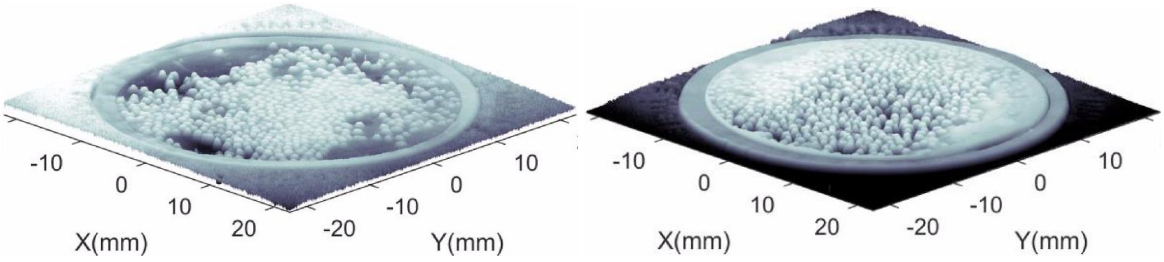

a. Marcellus shale (MSEEL core) fracture (31 days) ***b. Pierre shale fracture (15 days)***

Figure 2-71. Pseudo-3D images of the samples at the end of the 1-month (Marcellus shale) and 2-week (Pierre shale) long compaction experiments. Fracture closure between the proppant grains are visible for both samples, and the complete closure of the aperture for large sections for the Pierre shale fracture.

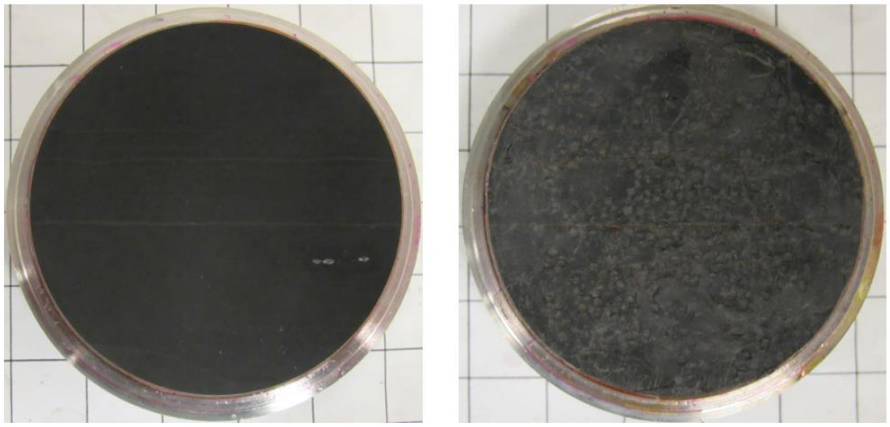

a. Marcellus (MSEEL) shale

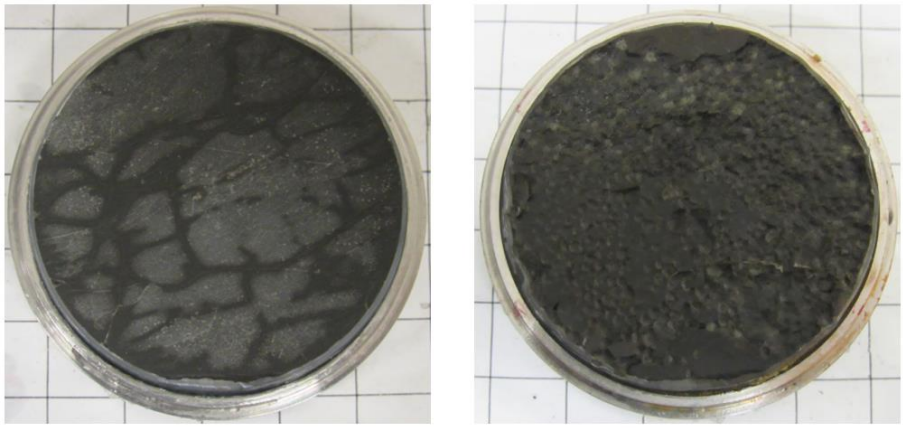

b. Pierre shale

Figure 2-72. Photograph of the fracture surfaces before (left column) and after (right column) of the experiments. Very prominent indentation casts and destruction of the fracture surface can be seen. Both samples contained preexisting fractures, possibly due to descication of the large amount of clay in the sample. The fracturing was more severe for the Pierre shale sample.

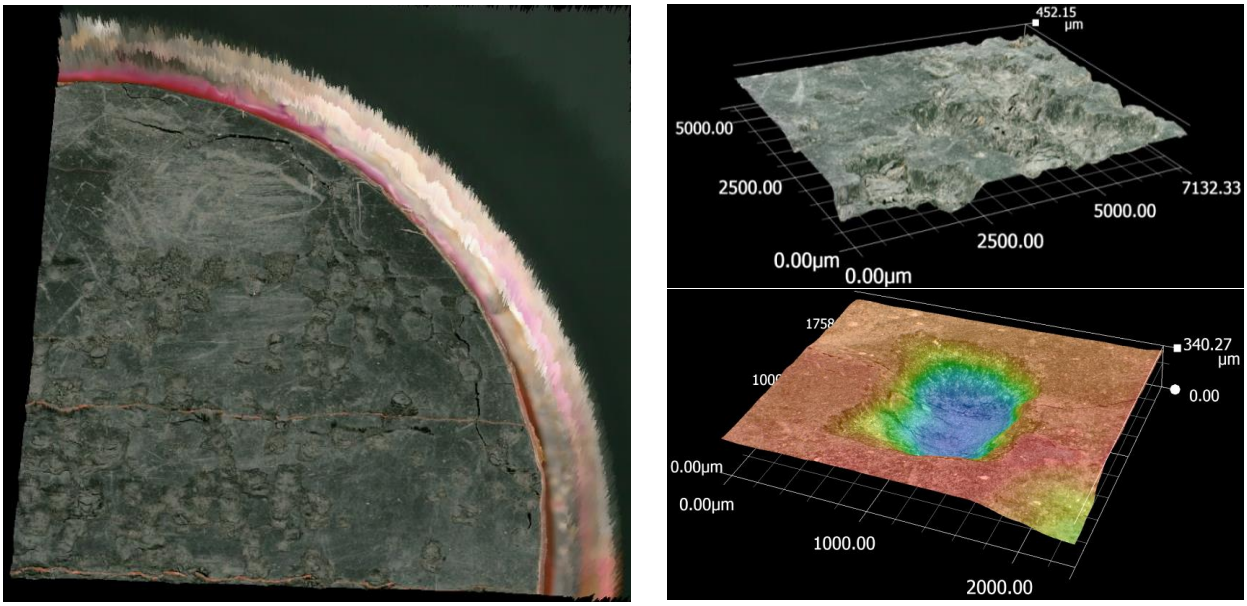

Figure 2-73. Microscope images of the Marcellus (MSEEL) shale sample and proppant casts. In addition to well-defined, deep proppant casts, close examination of the images reveal severe fracturing of the shale matrix between and around the cast.

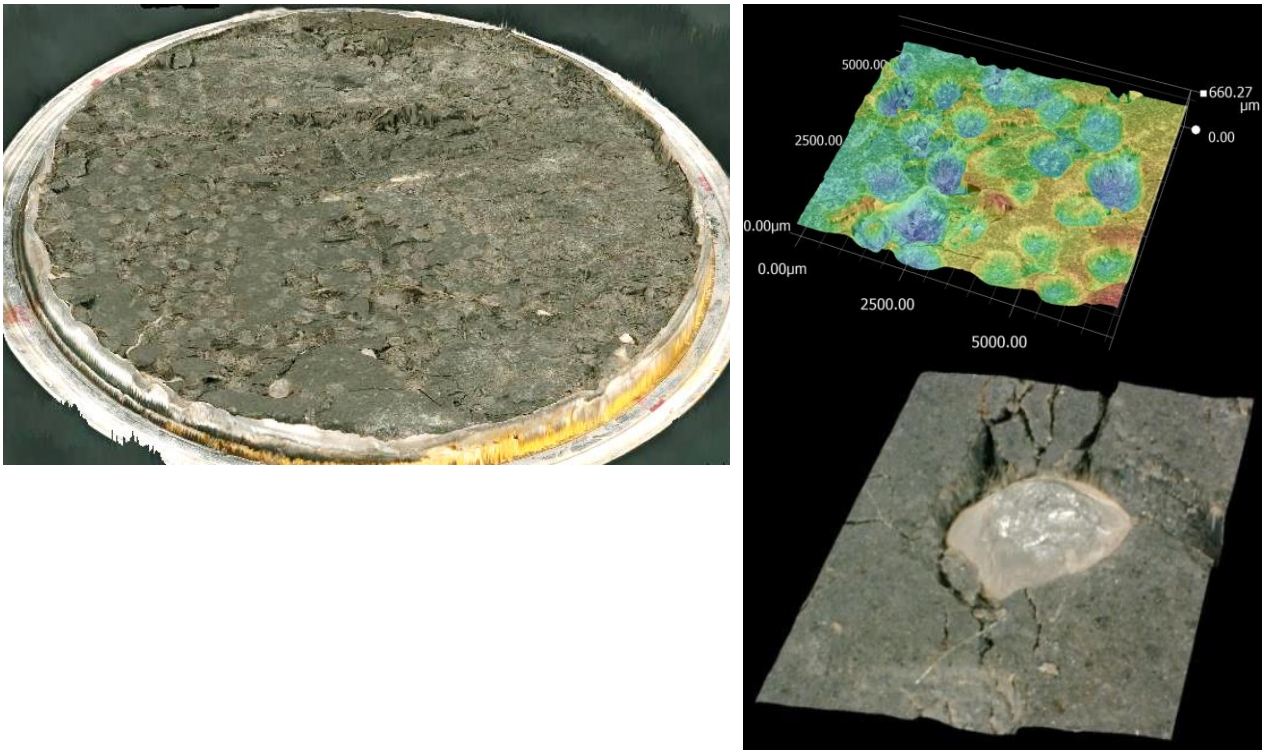

Figure 2-74. Microscope images of the Pierre shale sample and proppant casts. Very well-defined, deep proppant casts are visible. In some cases, the proppant grain was completely embedded and logged in the shale matrix. Although fracturing of the matrix was observed, the fine-scale fracturing of the matrix as seen in Fig.2-72 was not seen for this sample.

2.1.5.4 Stress and Time-dependent fracture closure and permeability changes

Finally, a summary of the fracture closure displacements and flow resistance (proportional to the inverse of the fracture conductivity) is shown for the entire effective stress cycle and for the long-term creep compaction tests. Figure 2-75 shows closure displacement and flow resistance changes as a function of the applied effective stresses for each experiment. The results presented previously for unpropped fractures are also presented for comparison.

For the effective stress changes (Fig.2-75), propped fractures exhibited much larger deformation than unpropped fractures. Interestingly, the results for the Marcellus/MSEEL sample were similar to the brittle Marcellus/outcrop and Barnett shale samples. This can be attributed to the crushing of the proppant grains in the brittle shale fractures while the ductile MSEEL sample exhibited little grain crushing but larger proppant embedment. The very ductile Pierre shale exhibited by far the largest fracture closure and hysteresis.

Because of the very large initial permeability of a propped fracture, the pressure drop across the fracture during the experiments were difficult to determine using the small flow rate of the tests (typically, only up to 1 mL/min of flow was applied during the permeability measurements). Nonetheless, the changes in the flow resistance during the creep tests at the maximum effective stress (~3,920 psi) and the resulting hysteresis can be seen, consistent with the fracture closure displacement. For the case of the Pierre shale sample, during the creep test, the flow resistance increased very rapidly. In order to limit the maximum pressure drop across the fracture to 10–25 psi, the flow rate was reduced by steps down to 0.01 mL/min during the test. Because the permeability became very small at the end of the two weeks, the permeability measurement was not conducted during the rapid unloading of the effective stress at the end of the experiment.

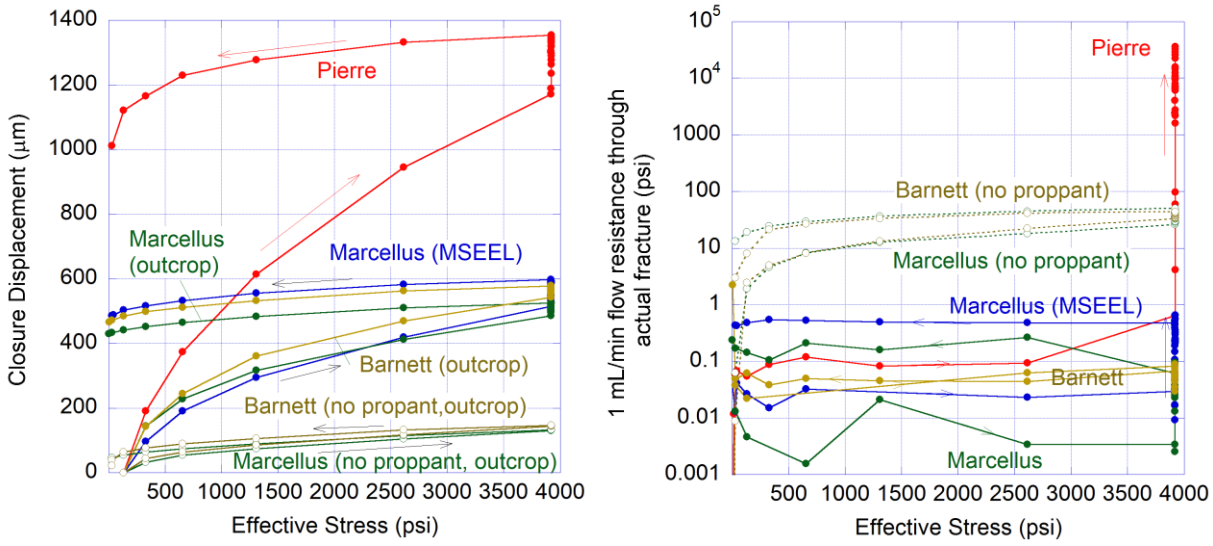

Figure 2-75. Fracture closure and flow resistance (1/permeability) changes during the entire experiments. . Results for the experiments without proppant are also shown for comparison.

During long-term creep deformation experiments, as expected, we observed initial rapid fracture closure and permeability reduction (flow resistance increase). These were followed by slower, but continuing changes in the fracture aperture and permeability. Again, the deformations for unpropped fractures were much smaller than both brittle and ductile shale samples with proppant. Note that the deformations shown in Fig.2-76 are relative closure displacements from the beginning of the creep tests, and the vertical scale is expanded compared to Fig.2-75.

The relative closure deformations for each shale type are consistent with the short-term (30 min) indentation experiment results shown in Fig.2-20. Permeability of the unpropped fractures in brittle shales, however, was larger than propped Pierre shale but smaller than MSEEL Marcellus shale, because the initial apertures for the umpropped fractures were already quite small (a few tens of microns).

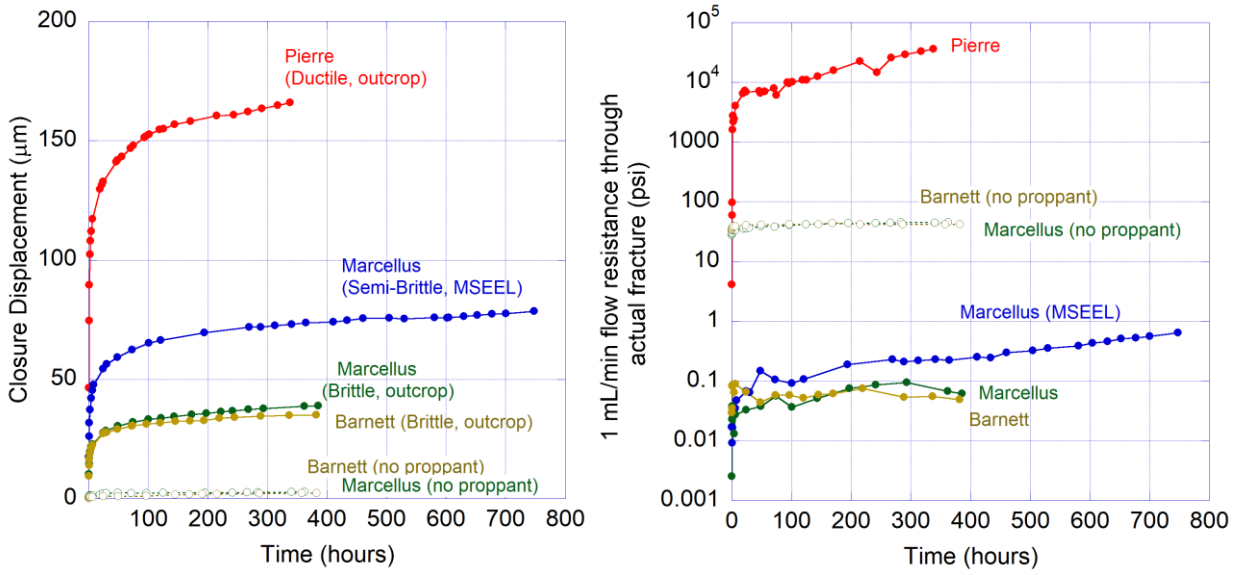

Figure 2-76. Creep closure displacement and flow resistance (1/permeability) changes during the long-term time-lapse experiments. Note that the closure displacements shown here are the additional deformaitons of the fractures after the target effetive stress is reached. Results for the experiments without proppant are also shown for comparison.

2.1.6 Subtask 2.6– Gas/liquid transport experiment (Year 2)

This subtask investigated the effect of shale matrix pores including fractures on gas and fluid transport. The majority of pores in shales is narrow, have complex and poorly described topologies, and likely have regions with varying wettability. Narrow pores restrict flow and at the same time promote capillary condensation which can further restrict flow. Capillary condensation will occur under appropriate conditions of pressure, temperature, and salt concentration which vary over location and production time. Varying (mixed) wettability can pin contact lines resulting in the need for very large pressure gradients to move fluids.

For this task we conducted X-ray CT imaging experiments by introducing high-density Kr gas into room-dry and humidified samples of five different types of shale studied in Subtasks 2.2 and 2.3 (Figure 2-77). These samples (2-inch diameter and 2-inch long cores) were placed in a 2.3-inch I.D. polycarbonate tube, with each sample wrapped in a cardboard layer to limit movement and separated by a cardboard disk. The tube containing the samples was placed on a PVC endcap, and the assembly was inserted into an X-ray-transparent aluminum pressure vessel (Figure 2-78). Samples were scanned to obtain initial densities (Figure 2-79). The vessel was leak tested with 200 psi N_2 gas, a vacuum applied for 30 min, and then finally filled with Krypton gas. Initially room dry (as received) samples were placed in the vessel and pressurized with 150 psi Kr for 8 days, followed by 1,000 psi Kr for 21 days. The shale was then removed from the vessel, weighed, and replaced in the vessel and humidified air was allowed to flow into the vessel for 10 days. After humidification the samples were pressurized with 1,000 psi Kr for 21 days. At the end of the experiment the samples were again removed from the vessel and reweighed to estimate the amount of water absorbed by the shale during humidification (see Table 2-3). The time line of the experiment is shown in Figure 2-80. To monitor density changes due to changes in water content and invasion of Kr, x-ray CT scans were taken at appropriate intervals.

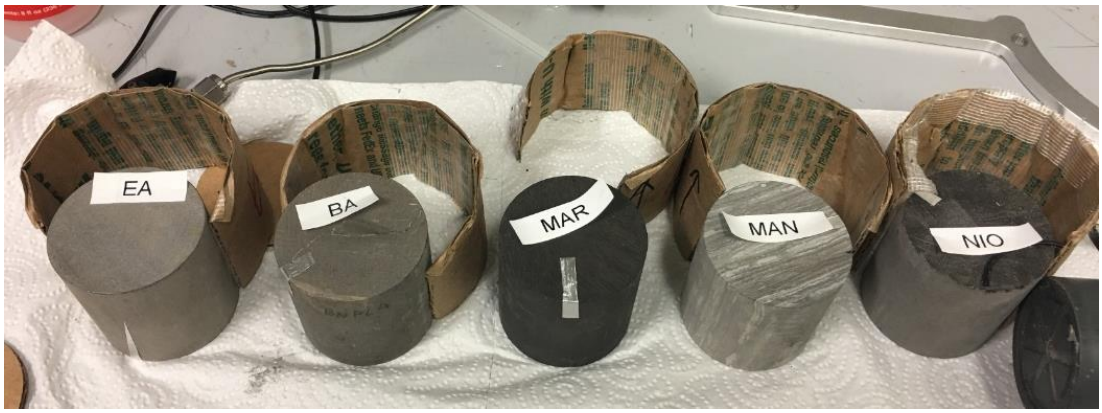

Figure 2-77. Shale samples used for Kr invasion tests. Left to right Eagleford, Barnett, Marcellus, Mancos, and Niobrara.

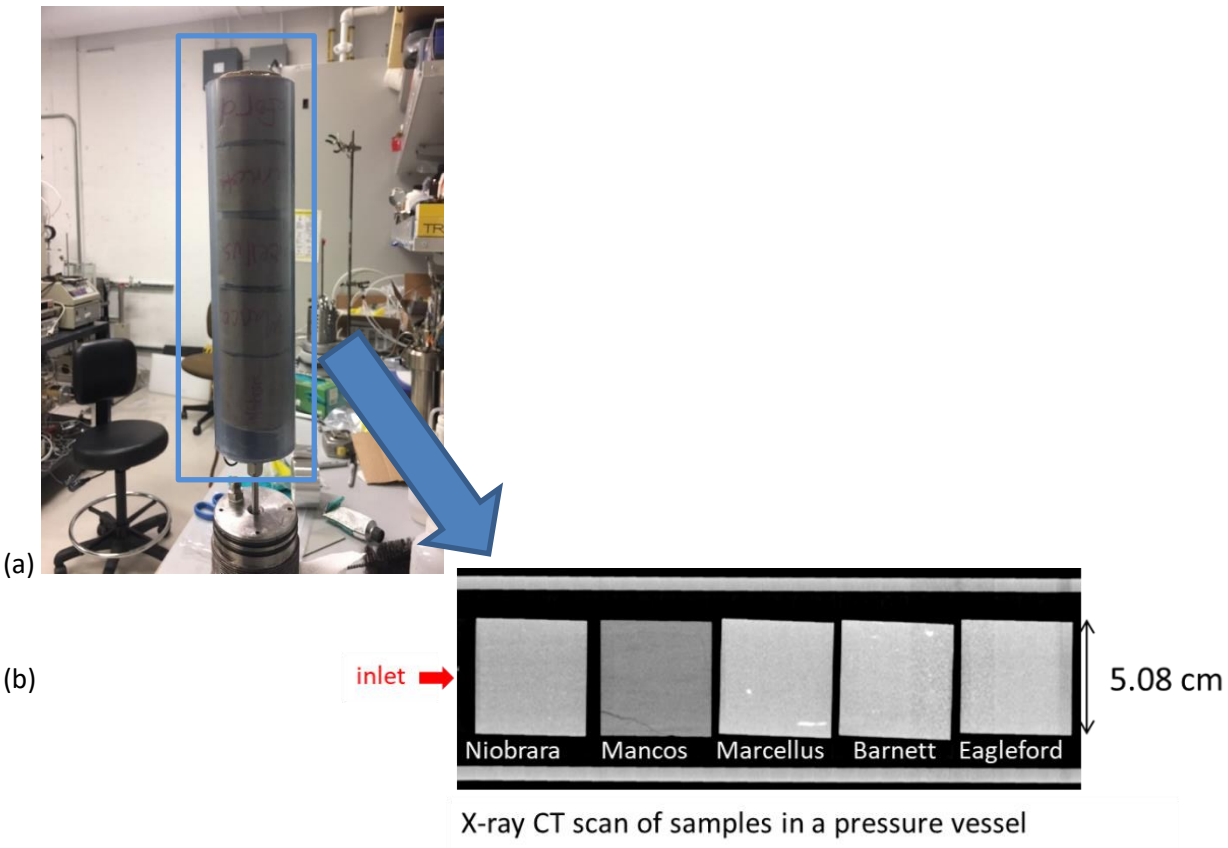

Figure 2-78. Sample assembly and X-ray CT image of shale cores for heavy gas migration imaging experiments. (a) Assembled sample (b) X-ray CT image of shale cores within a pressure vessel

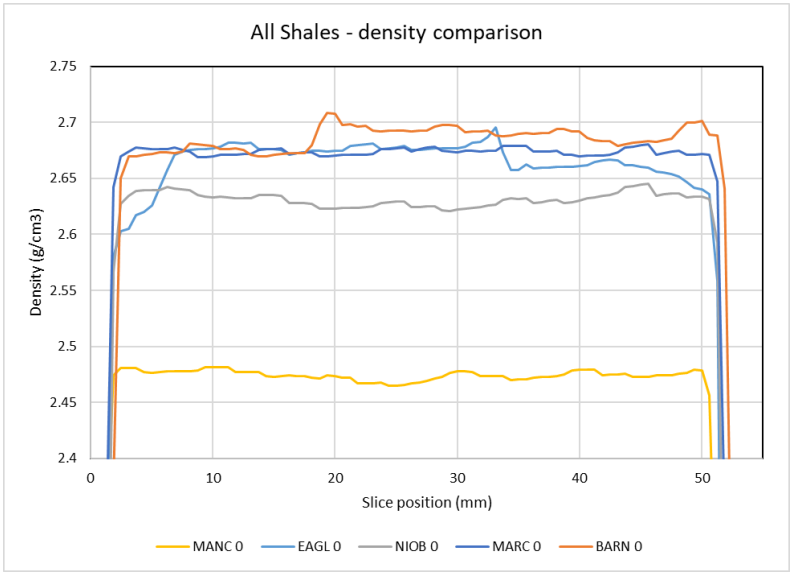

Figure 2-79. Comparison of initial shale densities.

Table 2-3. Weight and density changes to shale samples after humidification.

Shale	Room dry Weight (g)	Room dry density (g/cm3)	Humidified Weight (g)	Humidified density (g/cm3)	Difference (g)	Density Difference (g/cm3)
Eagleford	260.243	2.528	260.393	2.529	0.150	0.00146
Barnett	271.258	2.635	272.020	2.642	0.763	0.00740
Marcellus	271.946	2.641	272.569	2.647	0.623	0.00605
Mancos	262.714	2.552	265.380	2.578	2.666	0.02589
Niobrara	254.574	2.473	256.084	2.487	1.510	0.01467

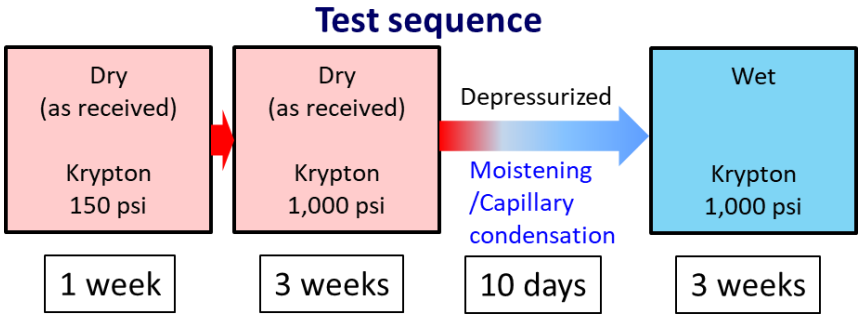

Figure 2-80. Test sequence.

As expected, measurements indicate imaging of the gas migration is not an easy task. Subtle differences in the gas and fluid phases in shale are overlaid by large density differences in the samples due to material variations in each bedding layer, fractures, and inclusions (Figures 2-81 and 2-81). Difference images with respect to the reference (T = 0 hrs) do not readily provide obvious images of gas migration (Figure 2-83). However, simple averaging to calculate density differences do show clear indication of gas movement.

To obtain density data, CT scans were converted from Hounsfield units (HU) to density using a calibration curve obtained from scanning standard samples of known density. A circular region was then defined which included a cross section of the sample. Average density was then calculated for each scan slice through the sample. Examples of this process, and images of the cross section for the Niobrara sample are shown in Figure 2-84. Figure 2-84a shows average density for each slice along the axial direction for the 150 psi and 1,000 psi Kr invasion in the room dry Niobrara shale. Typical cross sections for each of the conditions are shown in Figure 2-84b. The average density of the entire core is listed in Figure 2-84c. The average density data is summarized in Table 2-4 and Figure 2-85 for all the cores.

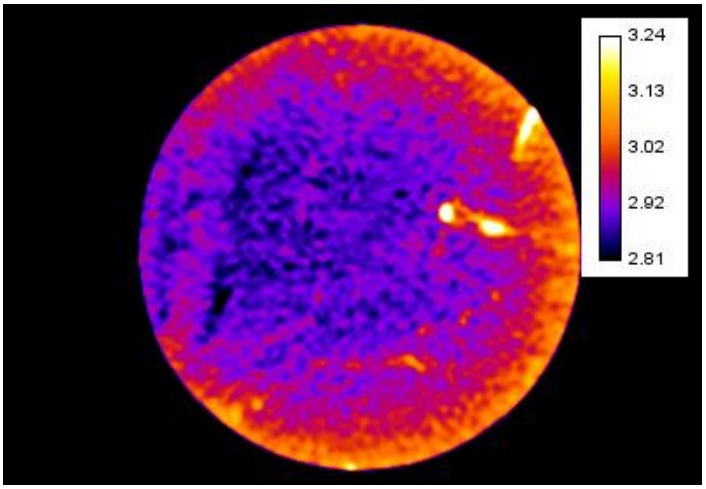

Figure 2-81. A selected slice through a Barnett shale core showing calibration in g/cm^3.

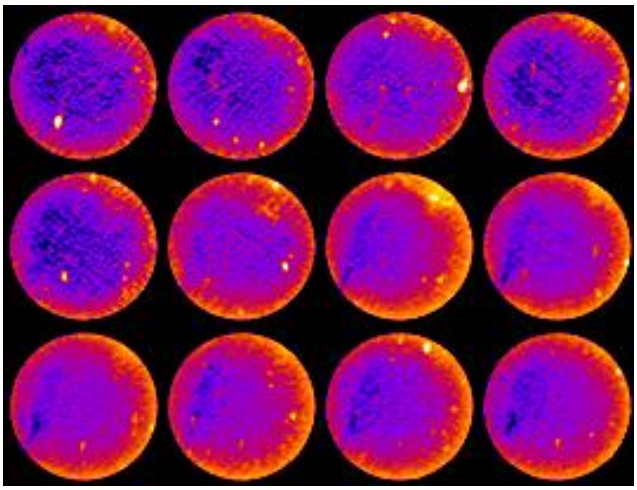

Figure 2-82. A series of cross sections along the axis of the Barnett shale core (same calibration as Figure 2-81).

(a) (b)

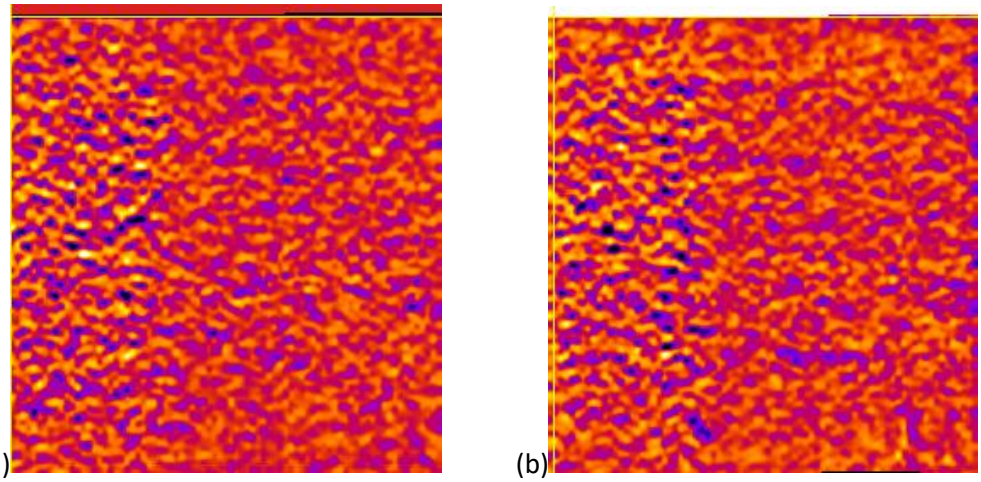

Figure 2-83 Resulting cross section from the difference between (a) T=0.5 hr and T=0 hrs, and (b) T=78 hrs and T=0hrs. Visually, there is no observable change in the density of the sample.

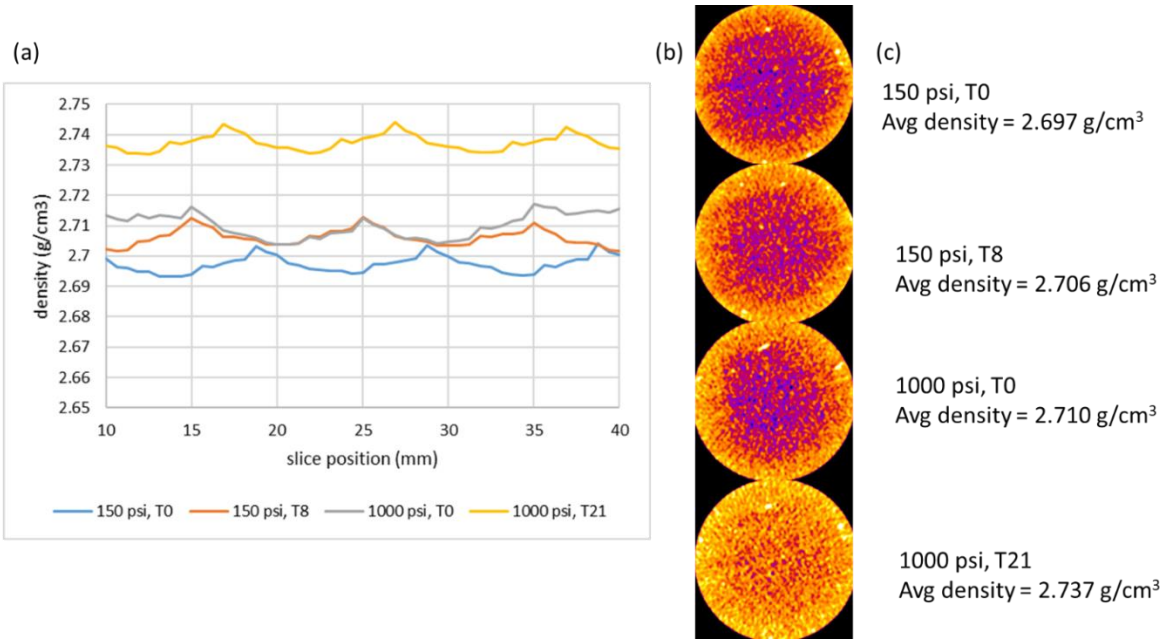

Figure 2-84 Density of Niobara (room dry) during Kr exposure at 150 psi and 1000 psi. (a) average density per slice along axis of core (b) selected cross section at each condition (c) average density of the core at each condition.

Table 2-4. Average density changes due to Kr invasion into shale samples

	150 psi T8-T0 day	1000 psi T21-T0 day, room dry	1000 psi T21-T0 day, humidified
	density difference (g/cm^3)		
Barnett	0.00331	0.02173	0.00755
Marcellus	0.00720	0.04598	0.02921
Mancos	0.00386	0.01120	0.01146
Niobrara	0.00899	0.02748	0.05015
Eagleford	-0.00637	0.00446	0.00105

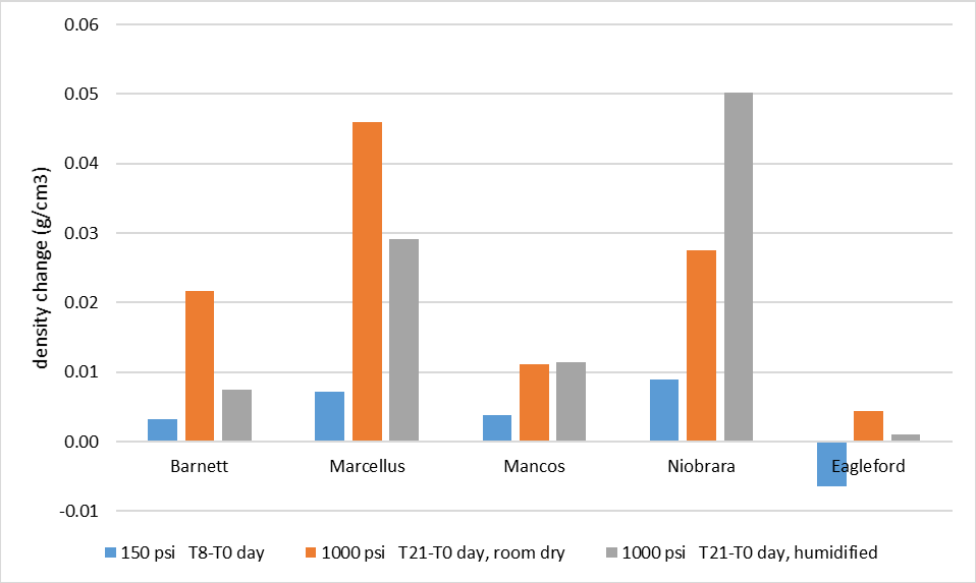

Figure 2-85 Density changes due to Kr invasion into the shale cores.

Treatment with humidified air decreased the amount of Kr invasion into the samples for the Barnett, Marcellus, and Eagleford shales. For Mancos, there was no change and for Niobrara there was more invasion into the core after humidification. When the humidified samples were pressurized with 1,000 psi Kr, the density of the sample decreased. This was likely due to the Kr gas pushing out some of the absorbed water from the samples. For the Barnett and Marcellus shales this effect resulted in a density that was still higher than the density of the dry core. For the Eagleford, the density was slightly lower than the room dry condition, but invasion into this core was so small that the effect was within experimental error. For Niobrara and Mancos, this resulted in a drying of the sample below the level in the 'room dry' state.

Table 2-5. CT measurements of sample densities (in g/cm3) before and after pressurization of the humidified sample compared to density of the sample at the room dry (as received) condition.

	Density of sample after humidification, 0 psi	Density of sample after humidification and pressurization to 1000 psi	Density of room dry sample, 1000 psi
Barnett	2.83201	2.78357	2.77825
Marcellus	2.82482	2.77882	2.76123
Mancos	2.53015	2.51492	2.53504
Niobrara	2.71207	2.68277	2.70994
Eagleford	2.79557	2.74792	2.75982

2.1.6 Final remarks on the laboratory experiments

In Task 2, we developed a novel optical visualization technique/setup for real-time visualization of shale fracture and proppant compaction under elevated stress and pressure. Using this system, some key findings have been made, and important lessons have been learned.

1. Proppant failure in a brittle shale fracture

We determined our initial experimental parameters (proppant coverage, effective stress) based upon directly measured individual proppant strength and considerations of the brittle, strong shale matrix properties. However, a large part of the quartz sand proppant crushed during the experiment. From the time-lapse images of proppant failure, this seems to be mainly attributed to the nature of the proppant which was a sparsely distributed (~50% surface coverage) monolayer. With hard fracture surfaces which deform little under the concentrated stress at the proppant-shale contacts, only a handful of proppant grains carry the load before fracturing and then transferring the load to the next largest grains. The result is progressive, "zipper" failure of the proppant in the fracture (Fig.2-80). Although less likely to happen for softer (or very strong) proppant and multiple-grain layers of proppant (because of grain confinement from the sides and increased overall compliance of the proppant layer), this failure mechanism will lead to gross overestimation of the proppant layer strength if the compressive strength of individual proppant grains or a proppant pack is used to predict the proppant sustainability in a fracture within strong, brittle shale.

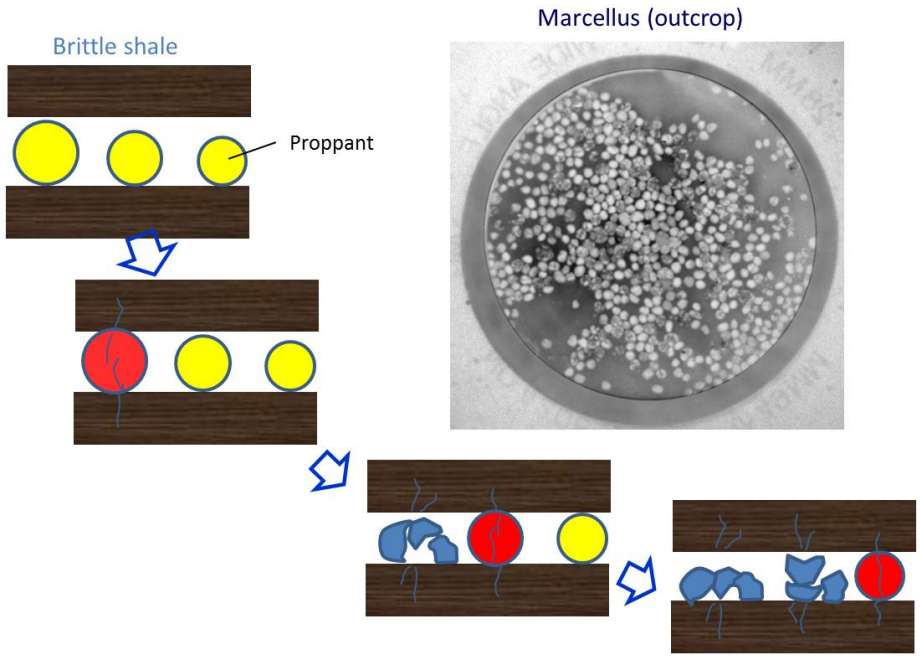

Figure 2-80 Observed proppant crushing behavior in brittle shale fractures. For sparse (~50% coverage), monolayer proppant, progressive and sequential failure of the grains resulted in crushing of a very large number of grains (>50%) during the initial effective stress increase stage.

2. Proppant embedment in a ductile shale fracture

Our original conceptual view of proppant embedment in ductile shale fractures was (1) the shale matrix deforms plastically beneath proppant grains, then (2) the overall fracture aperture reduces because the unsupported sections of the fracture closes by the amount proppant was embedded into the rock matrix. Based upon the visualization experiments, depending upon shale type, this process can be slightly more complex.

Initially, the ductile shale samples we used in the experiment (MSEEL Marcellus shale and Pierre shale) exhibited heaving of the shale matrix and debris production around proppant grains, which resulted in filling of the space between proppant grains and reduction of the fracture permeability. This was followed by the closure of unsupported fracture surfaces due to time dependent (visco-plastic) deformation of the shale matrix. What seems to be interesting is that, if a sparse, monolayer of proppant is distributed as a continuous network compartmentalizing the unsupported sections of a fracture, at least initially, destruction of the shale matrix by proppant grain indentation can actually reduce the permeability of the fracture. Another possibility is that when proppant accumulate at critical location in a flow network (e.g., fracture intersection), such heaving can create an effective local flow barrier. Such behavior, however, is expected to vary depending upon the ductility of the shale, as seen in the different proppant behavior between semi-ductile MSEEL Marcellus shale (resulted in debris production but not closure of unsupported surfaces) and very ductile Pierre shale (resulted in visco-plastic heaving, complete embedment of proppant grains, and large-scale deformation of the unsupported shale matrix).

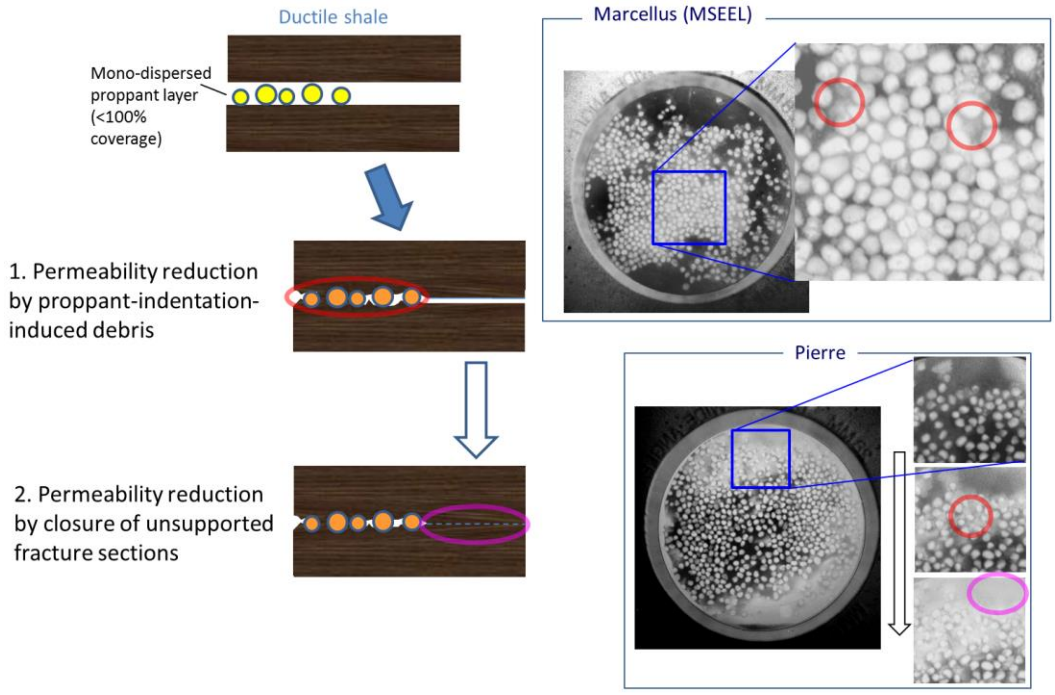

Figure 2-81 Observed aperture closure behavior in ductile shale fractures. Initially, aperture and permeability reduction were caused by filling of the inter-proppant-grain space by heaved matrix and debris produced by indentation. In later times (for more ductile Pierre shale), unsupported (by the proppant) sections of the shale fracture closued, resulting in near-complete brocking of the fluid flow along the fracture.

3. Time-dependent fracture closure displacement and a universal law

When the experimentally measured time-deformation data in Fig.2-76 are replotted using a logarithmic time axis, remarkably distinct linear relationships emerge (Fig.2-82) (with, perhaps, exceptions for the fractures without proppant). Also, the slope of the fitted lines appears to change when there is a dramatic change in the fracture permeability (or possibly fracture compaction mechanisms).

Such semi-logarithmic time scaling laws have been observed in may geological processes involving "healing" of materials (e.g., Griggs, 1939, Kneight et al, 1995TenCate, 2011). Snieder et al. (2017) showed such scaling can result from superposition of relaxation process at a range of scales, as would be the case for the embedment of proppant grains with various contact conditions. Although this scaling law does not seem to apply directly to the permeability changes in the fracture, the semi-log time scaling for proppant embedment (and possibly ductile shale fracture matrix deformation, for the case of Pierre shale after the "kink" point) appears to be quite robust, and can be a powerful predicting tool for long-term fracture deformation and permeability changes. Potentially, such tool can be applied to shales with a wide range of ductility, as the results of our experiments demonstrate.

It is tempting to predict very long-term behavior of fractures using short-term experiments on small chip samples (i.e., via grain-scale indentation experiments). Fig.2-83 shows indentation creep displacements during 30-minute loading tests using our indentation test system. The anticipated semi-logarithmic time scaling is not evident for all the samples. However, the Pierre shale sample did exhibit a very clear semi-log trend, which encourages us to do further investigation into the possibility.

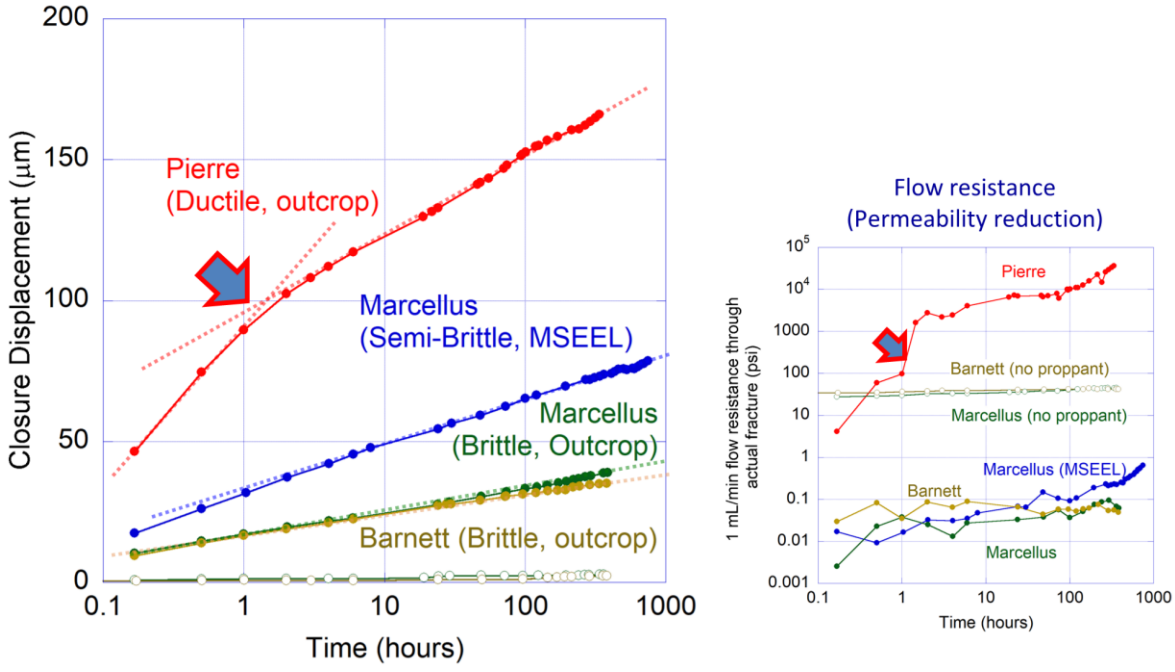

Figure 2-82 Remarkably distinct semi-log time scaling of fracture closure (creep) displacement during long-duration compaction experiments. A sudden change in the slope for the Pierre shale test corresonds to an abrupt increase in the flow resistance.

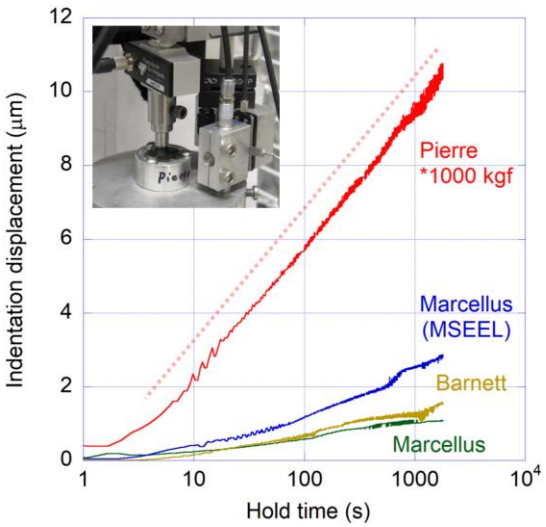

Figure 2-83 For the short-duration (30 min) indentation experiment, the semi-log time scaling was not obvious, possibly because of the effect of sample heterogeneity. However, the results for Pierre shale sample (chip) did show a clear semi-log scaling.

4. Impact of increased test temperature on the sample behavior and fracture visualization

Almost all the experiments in this project were conducted under room temperature (~25°C). One visualization experiment, however, was conducted on a brittle Barnett shale sample with proppant, at a slightly elevated temperature of 60°C (Fig.2-84). This test resulted in somewhat increased fracture compaction, which also seemed to follow the semi-log time scaling initially. However, after ~1 day, the compaction displacement stopped changing, and after ~4 days, sudden increases in the flow resistance were observed. Post-experiment examination of the sample revealed that the organic fluorescent dye produced highly viscous substance in the system, which seemed to have impeded the movement of the

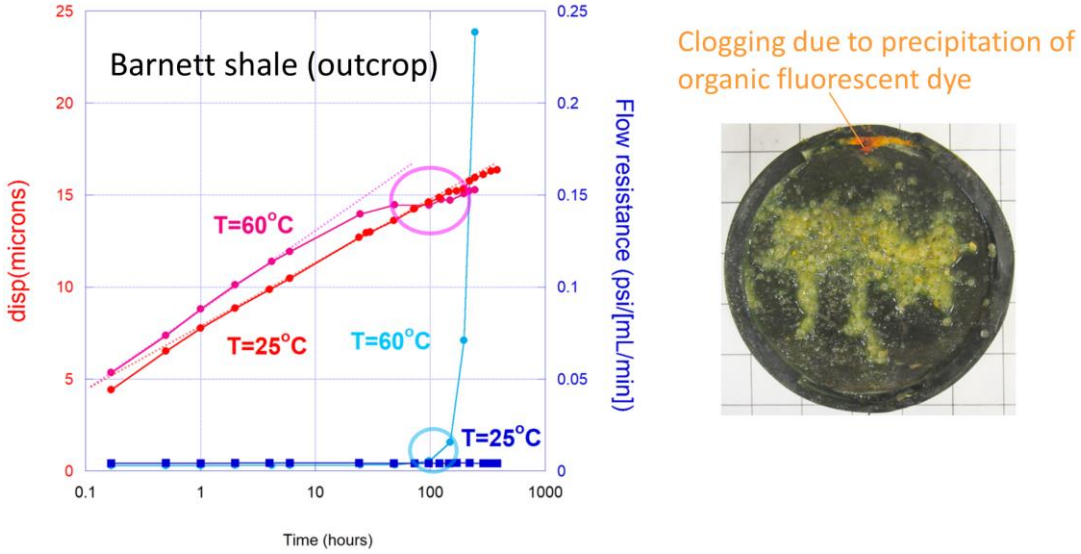

Figure 2-84 One experiment conducted at 60°C on another Barnett shale sample exhibited faster compaction following semi-log time scaling. However, the prolonged exposre of the fluorescent dye in the system resulted in sedimentation (precipitation) of the dye at the fluid inlet, resulting in clogging.

pressure vessel piston, and reduced the permeability by clogging. These results indicates that the application of the fluorescent-dye imaging method needs to be modified for higher-temperature experiments. Currently, we are considering injection of the dyed fluid only when imaging of the fracture is necessary.

The use of the intermittent use of the imaging (dyed) brine may also be necessary because of the high-temperature instability of the fluorescence of the dye. Fig.2-85 shows UV light induced fluorescence of dye-containing brine (0.1%wt) kept at elevated temperatures over time. The reference, room-temperature sample did not exhibit noticeable changes in the fluorescence capability over the test duration. It can be seen that within a few days, the reduction in the fluorescence intensity becomes visible, and the reduction is severer for higher temperatures.

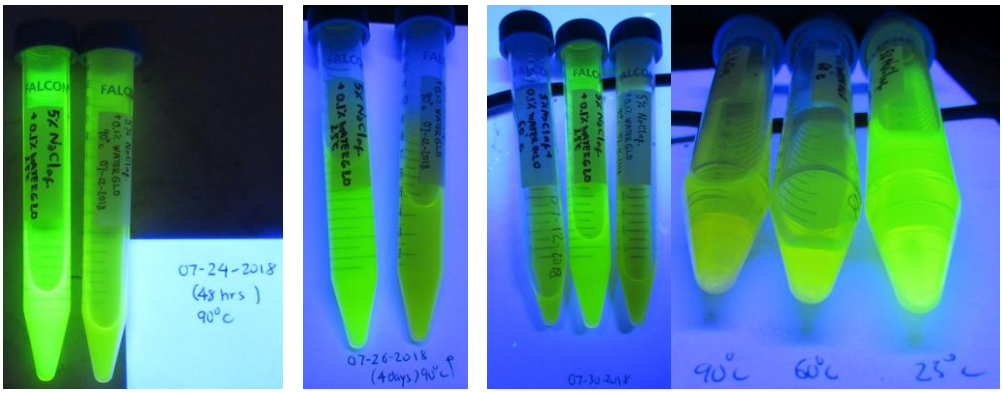

a. 48 hrs b. 4 days c. 18 days

Figure 2-85 Prolonged heating of the dye itself did not cause precipitation. However, when heated, the dye started to lose fluorescence capability after a few days (tested at 60°C and 90°C)

2.2 Task 3.0 Numerical Modeling

The numerical modeling part of this project focused on model development and testing based on LBNL's coupled multiphase flow and geomechanical codes, TOUGH-FLAC and TOUGH-RBSN. We developed and tested model approaches for both grain and block-scale mechanical interactions in the fracture and adjacent shale matrix. The approaches were tailored to capture coupled hydraulic and mechanical responses in proppant filled fractures in shale based on previous laboratory studies reported in the literature, and refined based on new laboratory results as reported in Section 2.1. The two codes were used to solve similar but complimentary problems of proppant deformation/crushing in strong, brittle shale and rock matrix deformation/proppant embedment in ductile shale.

In the following subsections 2.2.1 to 2.2.6, the work and results are reported for each modeling subtask, with final remarks on the modeling work given in subsection 2.2.7.

2.2.1 Subtask 3.1— Develop grain-scale modeling approaches

Subtask 3.1 involves the adaptations and testing of TOUGH-FLAC and TOUGH-RBSN codes for grain-scale modeling. We envision two types of mechanical responses depending on the clay content of the shale. In a shale with high clay content we would expect more ductile behavior with elasto-plastic yielding, whereas in a shale with lower clay content we may expect more brittle mechanical response with discrete fracture propagation and crushing. We are exploring TOUGH-FLAC for modeling the ductile behavior with continuum elasto-plastic or visco-elastic (creep) constitutive models, whereas TOUGH-RBSN is explored for modeling the brittle behavior with development discrete fractures and crushing.

2.2.1.1 Grain-Scale modeling with TOUGH-FLAC (Subtask 3.1a)

The grain-scale modeling with TOUGH-FLAC was developed and tested in early FY2017 using solid elements for shale and proppants and special interfaces for interaction between shale and proppants. We successfully demonstrated and tested:

- Progressive proppant embedment with progressive increasing contact between the shale and proppant involving contact detection in 3D as well as large strain modeling with continuous updating of the geometric configuration.
- Proppant embedment using elastic and elasto-plastic (Mohr-Coulomb) constitutive models with permanent indentation pattern at the end of the simulation.
- Swelling expansion of the shale matrix when exposed to a change in pressure or changes in saturation and the effect of swelling on fracture aperture.
- Creep closure of fractures over several years with progressive embedment for proppants using visco-elastic model and creep parameters from laboratory data.

Figure 3-1 and 3.2 show one full 3D simulation example performed to test and demonstrate the capability to model embedment of multiple proppants. We considered a 4 by 4 mm part of a shale sample with 4 proppants of different sizes. Figure 3-1 shows how each proppant of different sizes have been embedded into the shale sample after 0.3 mm vertical compression. Figure 3-2 presents the

surface imprint after unloading when the upper rock sample has been moved up vertically 0.3 mm to its original position. Maximum embedment depth is 0.28 mm, which is reasonable considering that the maximum vertical compression on the top of the rock sample was 0.3 mm. The calculated imprints of the type shown in Figure 3-2 could be compared to observed surface imprints from laboratory experiments.

Figure 3-3 and 3.4 show example of creep closure modeling over a 3-year period. We applied elastic and creep properties based on modeling of laboratory experiments on Haynseville shale. In Figure 3-3 we can observe the initial sharp closure due to elastic embedment. Thereafter, the time-dependent embedment due to creep takes place 3 years of simulation time. At the end, we can observe that the fracture closure by creep is dominant. Figure 3-4 shows the vertical displacement and embedment after 3 months and 3 years. These results demonstrate the adopted grain-scale modeling approach for modeling long-term closure behavior of propped fractures. This approach of grain-scale modeling with TOUGH-FLAC will be very useful for future studies on long-term fracture closure and proppant embedment in soft and ductile shale of high clay content. The grain scale model also provides approach that in subsequent tasks of this project was used for modeling the indentation tests.

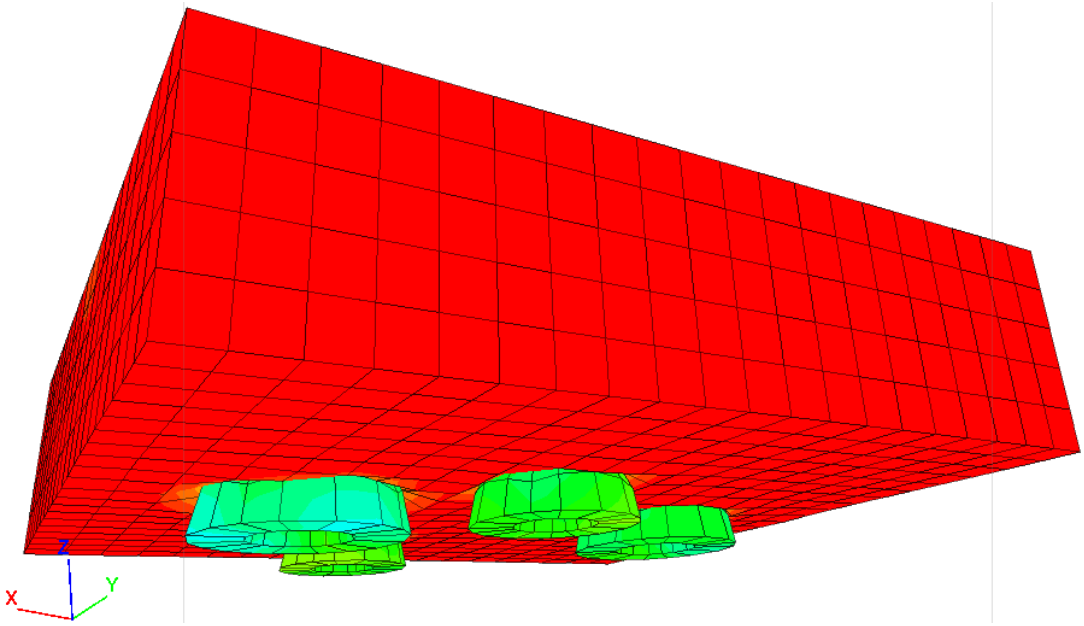

Figure 3-1. 3D simulation of vertical compression of soft rock on multiple proppants of various sizes (diameters ranging from 0.7 to 1 mm). The contours show vertical stress distribution with blue areas indicating high compressive stress and red areas low compressive stress.

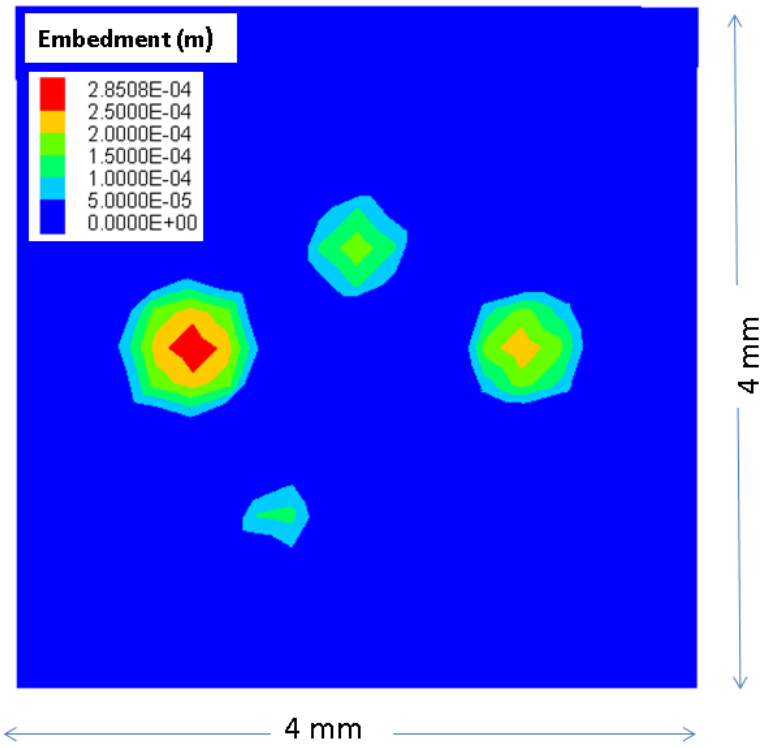

Figure 3-2. Plane view of the rock surface with contours of embedment depth.

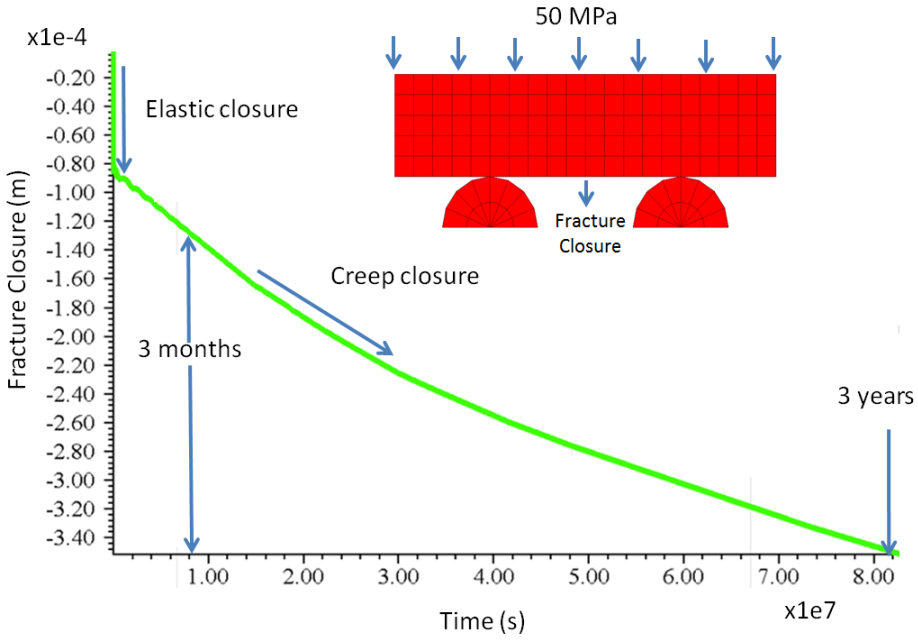

Figure 3-3. TOUGH-FLAC simulation results of closure of fracture by elastic and creep behavior using creep properties for Haynesville shale.

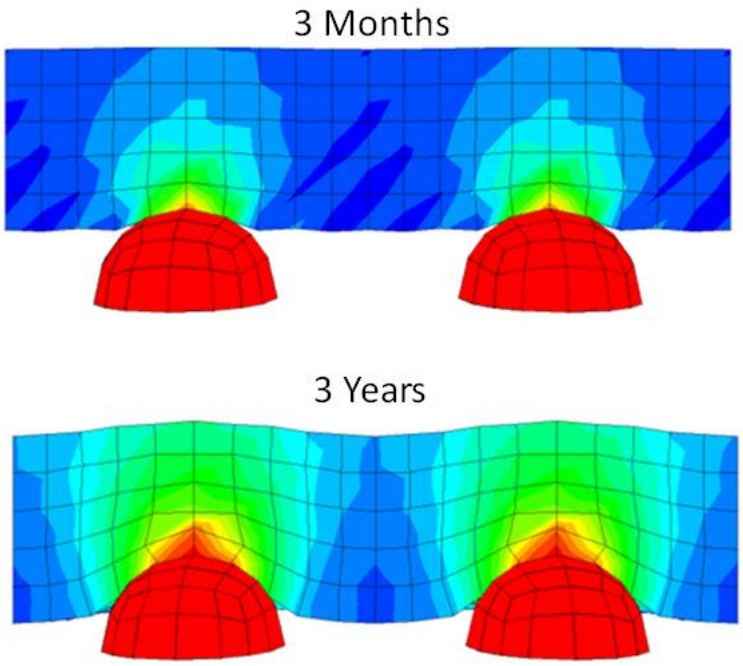

Figure 3-4. TOUGH-FLAC simulation results of closure of fracture after 3 months (about 0.13 mm closure) and 3 years (about 0.34 mm closure), where initial half aperture is 0.5 mm.

2.2.1.2 Grain-Scale modeling with TOUGH-RBSN (Subtask 3.1b)

In FY2017, the RBSN approach was applied for grain-scale modeling of proppants within relatively brittle, strong, and non-swelling matrix. In FY2018, the modeling approach has been improved by introducing a new type of element representing the contact between two materials that initially place apart. Main accomplishments and findings from the RBSN modeling works are as follows.

- More sophisticated node generation and mesh diskretization are developed to describe complex geometry at proppant grain-matrix contact zone.
- The RBSN modeling is extended to 3D simulations of proppant embedment into the matrix block. Embedment tests for a single proppant grain and a layer of multiple proppant grains on the matrix block have been simulated.
- Parametric studies have been conducted for different strengths of proppant. Dominant failure in the proppant domain (i.e., crushing) could be demonstrated with relatively low proppant strength.
- Random distribution of multiple proppant grains in a layer leads to a disparity in local failure extent due to the spatial density of grains.

We have used the rigid-body-spring network (RBSN) approach to analyze fracture propagation near the contact between proppant grains and the rock matrix. The RBSN is limited to model contact interactions with pre-defined interfacial elements, so it is more suitable to simulate failure with small embedment in relatively stiff and brittle matrix.

For the 3D modeling of proppant-matrix interaction, complex geometry arises around proppant-matrix contract zone where spherical surface and flat surface are in close proximity to each other. To model each domain surface without any geometrical distortion, sophisticated mesh generation process should be considered. By the nature of the Voronoi discretization, the geometry of a Voronoi cell is determined not only by its nodal position but by the relative position of the neighboring nodes. Thus, it is crucial to start with carefully distributing the nodal points, which will be a basis of the proper Voronoi tiling.

To construct a spherical component discretized with irregular Voronoi cells, a group of 2 nodes ($N = 2$ configuration) is placed on a randomly directed ray $\vec{v}_{\theta\phi}$ from the sphere center, as shown in Figure 3-5a. The combination of different random angles θ and ϕ defines the ray direction. Additional nodal groups are introduced in the same way, so a sphere and the surrounding phase (e.g., interphase, shell, etc.) can be represented (Figure 3-5b).

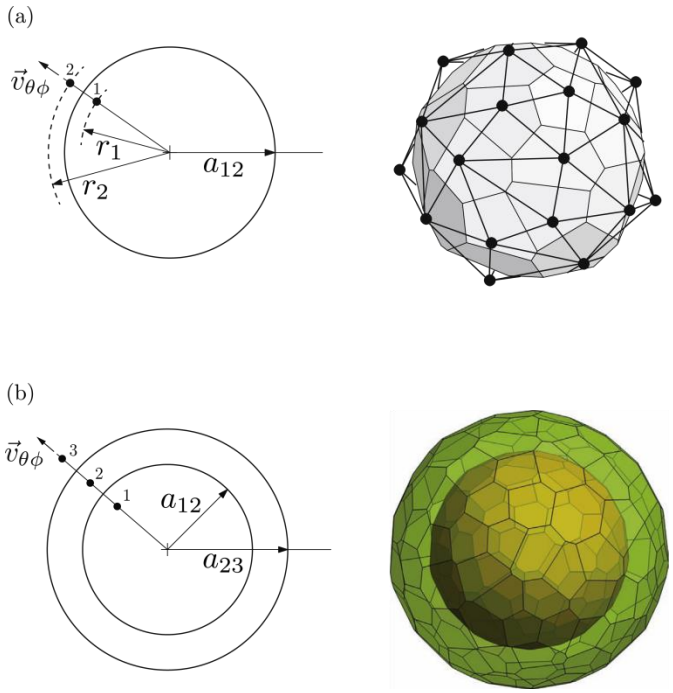

Figure 3-5. Nodal placement for diskretization of spherical components: (a) $N = 2$ configuration; and $N = 3$ configuration of layering nodal pairs.

To model multiple spherical grains, trial spheres are randomly positioned within the domain. In the current stage, the radii of spheres are assumed to be uniform. To avoid the overlaps between grains in the $N = 2$ configuration, grain placement is subject to $d^* > 2a_{12}$, where d^* is the distance between the centers of the trial sphere and the closest neighbor sphere.

Then, the geometry of the contact between a proppant grain and the matrix block is formed by introducing a set of auxiliary nodal points, which is positioned at the same distance from the spherical surface and from the block surface. These auxiliary points, together with the closest nodal sets of the sphere and block domains, generate a wedge-like volume and help to form the surfaces of each domain discretized with an intended geometry. Figure 3-6 shows examples of discretization of a single spherical grain and multiple grains contacted on the matrix block for 3D simulations.

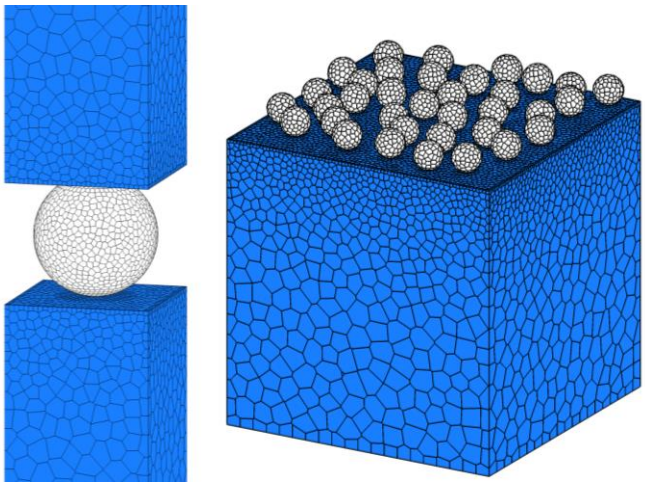

Figure 3-6. 3D mesh for a single proppant grain (left) and multiple proppant grains (right) contacted on the matrix block.

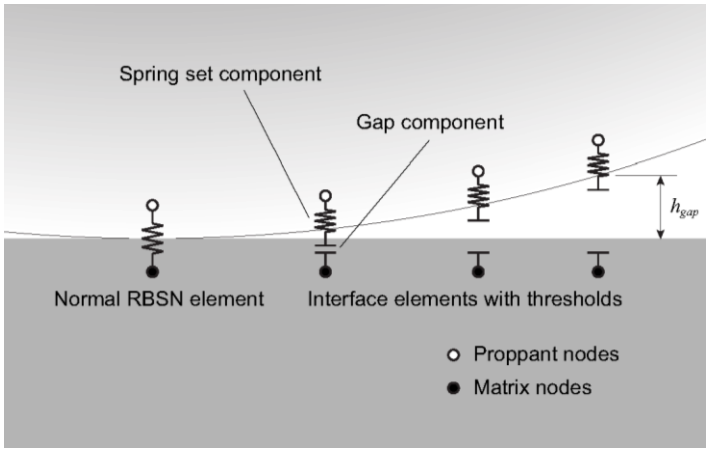

Figure 3-7. Conceptual illustration of new interface elements.

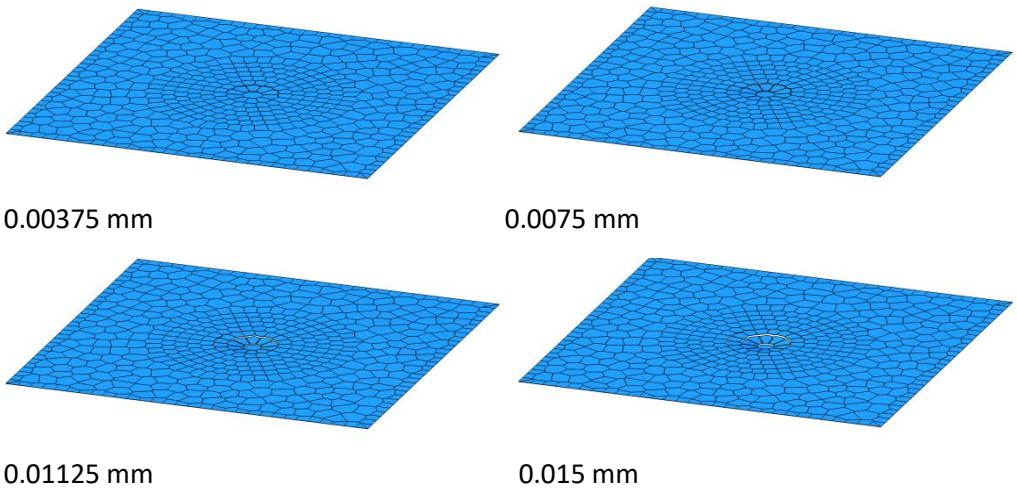

Figure 3-8. Deformation profiles of the matrix surface with increasing the embedment displacement (×5 exaggerated).

For more realistic modeling of contact zone and the corresponding deformation in the embedment process, we have improved the modeling approach by introducing a new type of interface elements. Figure 3-7 shows the concept of the modeling assumption. A normal lattice element is assigned at the initial contact where the spherical proppant domain borders the flat matrix block, and new interface elements are added to connect those two domains at the potential contact area. The new interface element comprises a gap component and a lattice spring set, so the spring stiffnesses are activated at a certain amount of displacement in the interface element. The threshold for stiffness activation is set based on the actual height of the gap, h_{gap}, at the initial model geometry.

The new interface elements are validated through a single grain embedment simulation. Figure 3-8 presents the progressive surface deformation at the proppant-matrix contact. With the increasing embedment displacement, the matrix deformation conforms to the contour of the hard proppant grain. The results demonstrate that the interface elements adaptively fulfill the contact behavior between two domains initially apart from each other.

With the new interface elements in the embedment modeling, we have conducted parametric studies for potential crushing of proppant grains and crack formation in matrix. A Voronoi mesh has been prepared for a 1-mm diameter single proppant grain placed between 5-mm thickness matrix blocks (the left illustration of Figure 3-6). A finer mesh is discretized for the potentially failing regions in the proppant grain and its nearby matrix region while a graded mesh density is given in the other matrix region for computational efficiency.

Three cases of different strength parameters are considered for the proppant material. In the Mohr-Coulomb failure criterion, cohesion, tensile strength, and friction angle are 1) 15.5 MPa, 10 MPa, and 30°; 2) 7.5 MPa, 5 MPa, and 25°; and 3) 3.5 MPa, 1.5 MPa, and 20°. The strength parameters of the matrix are adopted from the properties of Opalinus Clay: 5.5 MPa cohesion, 2 MPa tensile strength, and 25° friction angle. Young's moduli of the proppant and matrix materials are 70 GPa and 20 GPa, respectively. The embedment is simulated up to 0.015 mm of displacement.

In the results, different fracture formations are observed depending on the strength of proppant contrasted with the matrix strength. In the first case with the proppant much stronger than the matrix, only matrix failure develops from the contact zones while the proppant is in elastic regime with no fracture (Figure 3-9). With the lowered strength parameters of the proppant, yet stronger than the matrix, fractures initiate at the contacts and develop into both the proppant and matrix domains (Figure 3-10). Since the proppant is stronger than the matrix, the fractured region in the matrix is slightly larger than in the proppant domain. The last case with the weaker proppant also exhibits fracture development in both the proppant and matrix (Figure 3-11). However, compared to the second case, the weaker proppant has more vigorous fracture development than the matrix domain.

From the parametric studies, we have found a natural tendency for fractures to arise in weaker material when two different materials are compressed in contact, but the material strengths are not the absolute condition for fracture development. Especially when the material strengths are not in pronounced contrasts, the fracture formation may be more affected by the geometry of the contact zone (e.g., stress concentration in singular geometry).

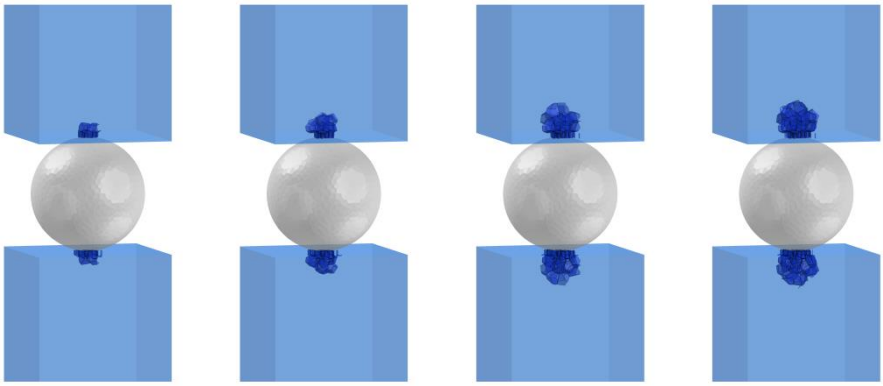

Figure 3-9. Fracture propagation in the matrix domain. No fracture occurs in the high strength proppant.

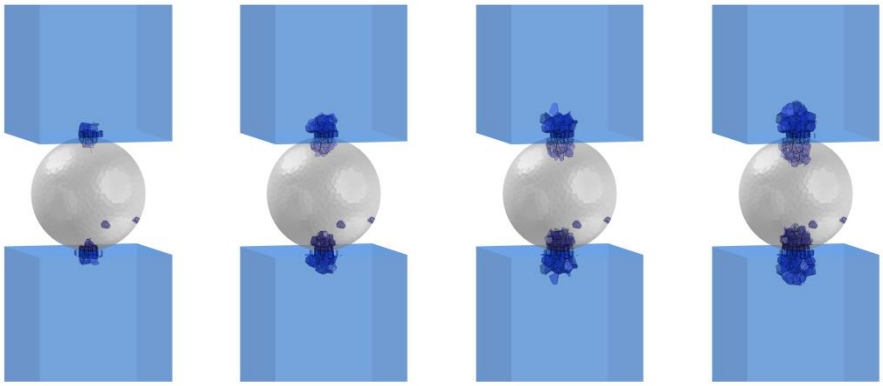

Figure 3-10. Fracture propagation in both the proppant and matrix domains. Since the proppant is a bit stronger than the matrix, smaller fractured regions are observed in the proppant domain.

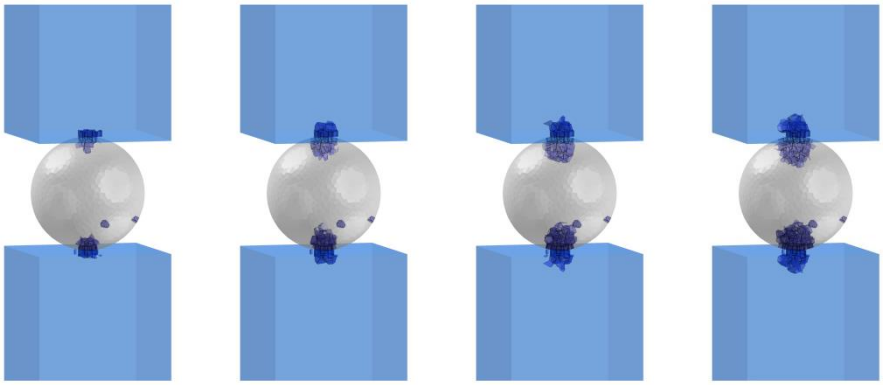

Figure 3-11. Weaker proppant exhibits more vigorous fracture propagation than the matrix.

Next, we simulated potential crushing of multiple proppant grains and fracture formation in the matrix block. Figure 3-12 shows the model geometry, where 35 spherical grains with 1 mm diameter are randomly distributed on a 10×10×5 mm matrix block. To reduce the computational burden, only lower half of the proppant grains are modeled with symmetric boundary conditions at the cut-plane of the spheres, and the gradation of mesh density is provided in the matrix block domain. Displacement controlled boundary conditions are applied at the bottom surface of the matrix block with up to 0.02 mm of displacement upwards to get the proppant grains embedded into the matrix.

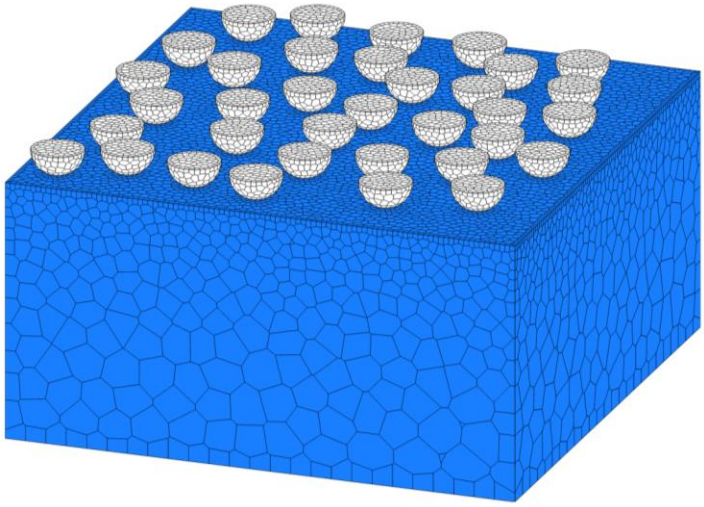

Figure 3-12. Model geometry for multiple proppant grains on the matrix block.

Two cases of different strength parameters are considered for the proppant material, for which in the Mohr-Coulomb failure criterion, cohesion, tensile strength, and friction angle are 1) 15.5 MPa, 10 MPa, and 30°; and 2) 7.5 MPa, 5 MPa, and 25°, respectively. The strength parameters of the matrix are adopted from the properties of Opalinus Clay: 5.5 MPa cohesion, 2 MPa tensile strength, and 25° friction angle. Young's moduli of the proppant and matrix materials are 70 GPa and 20 GPa, respectively.

Figures 3-13 and 3-14 present the failure patterns in the considered cases, where fractured lattice elements are illustrated with opaque dark blue color while the proppant grains and the matrix block are shown in transparency. As seen in the previous simulations for the embedment of a single proppant grain, different fracture formations are observed depending on the strength of proppant contrasted with the matrix strength. In the first case with the proppant much stronger than the matrix, failure mostly occurs in the matrix block around the contact zone (Figure 3-13). In contrast, with the lowered strength parameters of the proppant, yet stronger than the matrix, fractures initiate at the contacts and develop into both the proppant and matrix domains (Figure 3-14). It is interesting to remark that the extent of local failure differs from grain to grain, which might be attributed to the non-uniform distribution of the proppant grains on the matrix block.

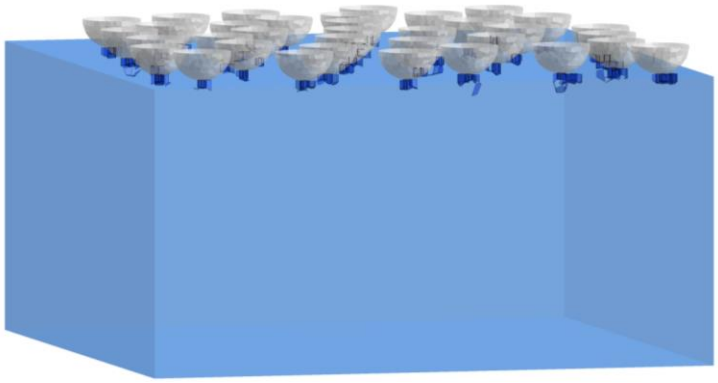

Figure 3-13. Failure pattern in the case of high strength proppants. Failure occurs mostly in the matrix domain.

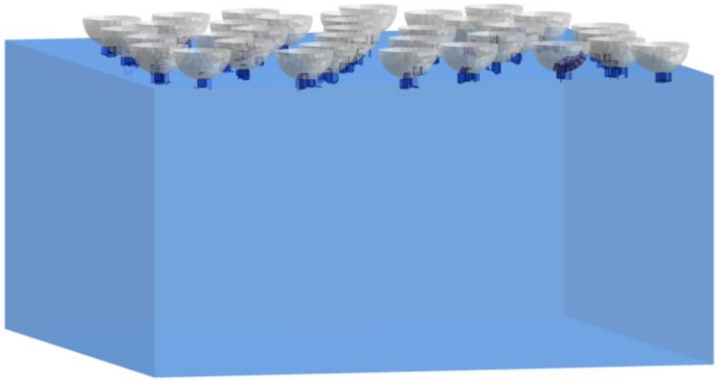

Figure 3-14. Failure pattern in the case of lowered-strength proppants. Failure occurs in both the proppant and matrix domains.

2.2.2 Subtask 3.2 — Development of a block-scale modeling approach

A block-scale model was developed and tested in Q3 of FY2017. The motivation for developing the block-scale model is that for block-scale problems (a few to tens of m's in scale), realistically, grain-scale models cannot be used. Therefore, upscaling by using an equivalent continuum layer modeling of a proppant bed and fracture is necessary.

The effective medium modeling of a fracture/proppant bed used in this approach is based on

- Finite thickness element fracture representation
- Proppant bed modeled as a continuum (elasto-plastic), exhibiting stress and time-dependent changes in the permeability
- Matrix swelling into fracture considered using an internal swelling method

In Q3 of FY2017 we demonstrated the use of the block-scale modeling approach for hydraulic fracturing at 100 m scale and then tested the applicability of the approach to model experiments on two-inch diameters rock cores (Figure 3-15). The model includes components of the sample, fracture, upper plastic replica and glass view window. The model is mechanically fixed on top for vertical displacement

and restricted from lateral displacements on the lateral boundary. In the model, the sample can be loaded from the bottom either by applying a constant stress or by applying a constant vertical velocity signifying a displacement controlled loading. In the simulation, the normal closure of the fracture and stress normal to the fractures is monitored. We tested the model using various constitutive models, from the basic non-linear elastic closure model, through elasto-plastic models to represent irreversible behavior, and creep for modeling long-term closure.

Figure 3-16 shows the results of modeling the proppant pack using an elasto-plastic model with a cap, in this case the Cam-Clay model, which can model compaction by pore-collapse rather than just shear failure. The results shown in Figure 3-16 includes initial elastic compaction, followed plastic compaction after the stress has reached the pre-consolidation pressure which was set to 5 MPa. After full compaction, there is an elastic rebound resulting in an irreversible behavior.

We also tested to model fracture closure by creep deformation. Here we used the same Burger models as we used in previous creep simulations at the grain scale. However, in the block scale model we do not represent the stress concentrations at proppants and actual creep parameters has to be calibrated to obtain relevant creep deformations. Such parameters could be calibrated again experimental data if they will display creep deformations. Figure 3-17 shows an initial elastic closure of 0.1 mm, followed by creep deformations for another 0.2 mm closure over 3 years.

Any of the constitutive models tested for the block-scale maybe used for the interpretative modeling of the experiments in FY2018 and will be a complement to the grain-scale modeling of the same experiments. The comparison between the grain-scale and the block-scale modeling of the experiments can be useful for learning how to upscale from the small to the large scale. The exact choice of constitutive model will be decided during the interpretative modeling of the experiments.

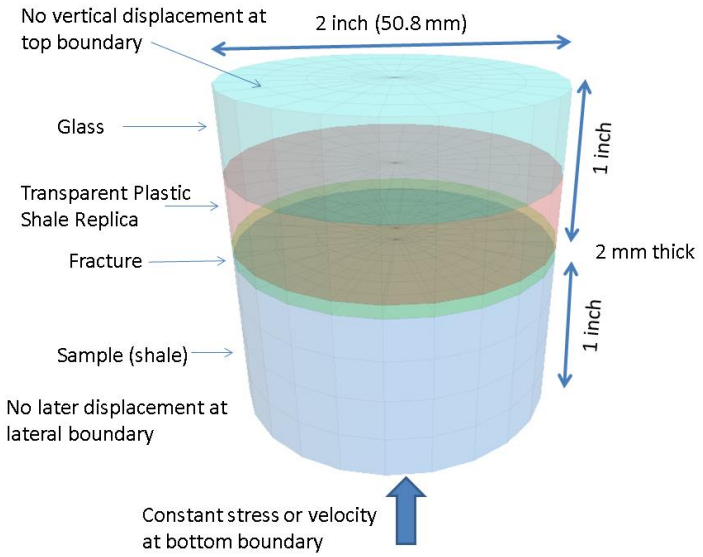

Figure 3-15. Model of laboratory experiment using a finite thickness representation of the fracture in block-scale modeling approach.

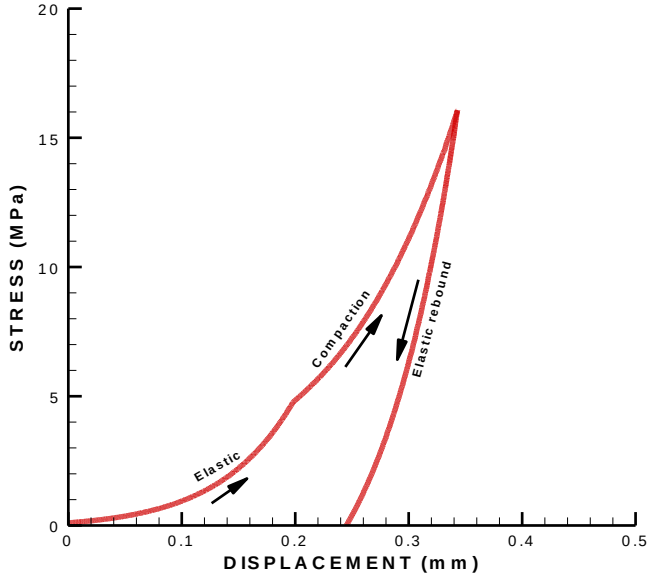

Figure 3-16. Modeled vertical stress versus vertical displacement at the fracture corresponding to fracture closure when using a Cam-Clay constitutive model for the finite thickness fracture elements.

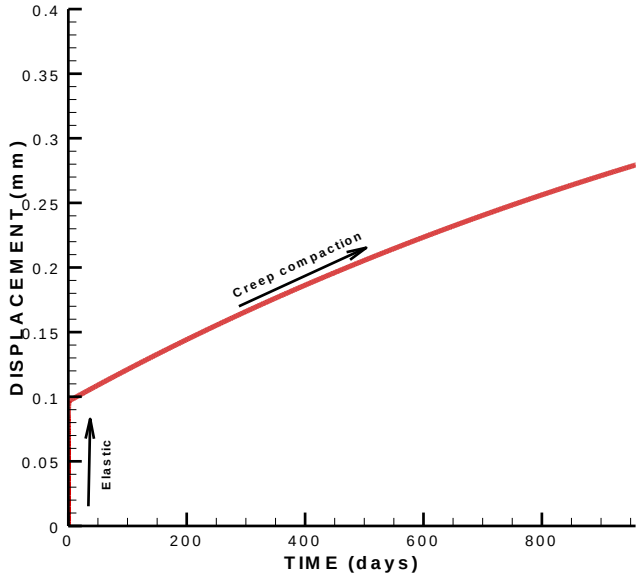

Figure 3-17. Modeled time-dependent fracture closure in the case of using Burger creep model for the finite thickness fracture element.

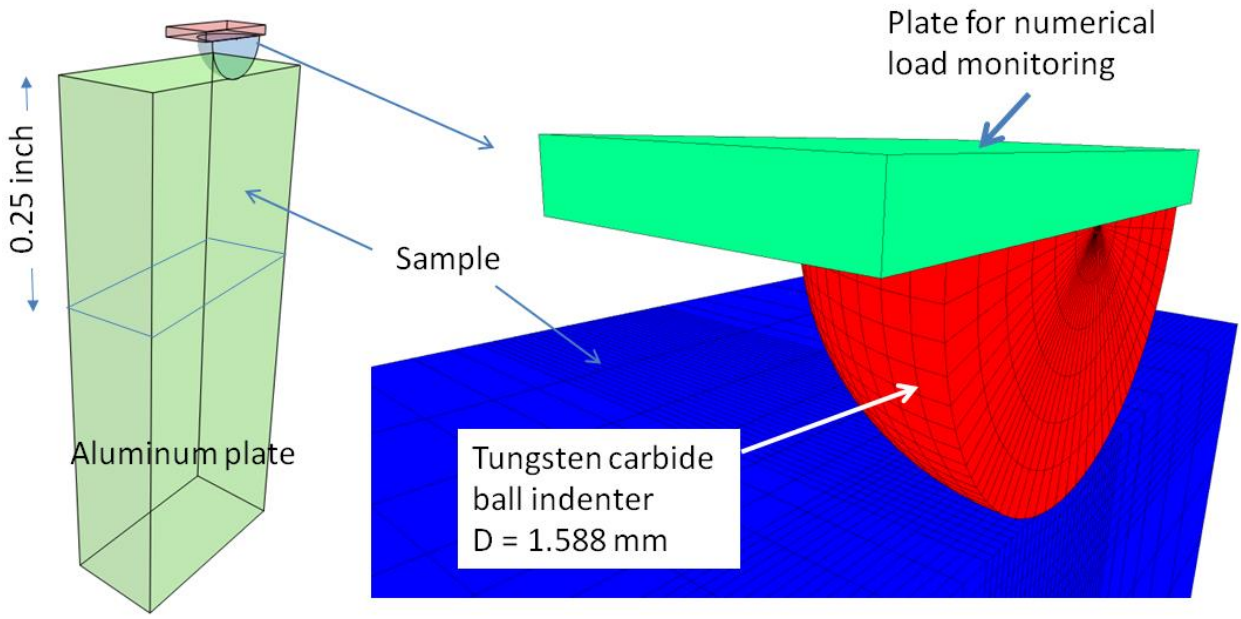

Figure 3-18. Half symmetric model for numerical simulations of indentation tests.

2.2.3 Subtask 3.3 — Modeling of indentation experiments and material parameterization

Micro-indentation tests conducted in Subtask 2.3 have been modeled with TOUGH-FLAC. The initial model that was applied is shown in Figure 3-18. It is a half symmetric model containing half of the tungsten carbide ball indenter and central parts of the sample including its entire sample thickness and underlying aluminum plate. On top of the indenter single element plate is places for applying vertical compression (velocity) and for recording the total load applied on the indenter.

We first successfully validated the model by modeling of the indentation test on aluminum, which has known properties. An initial verification modeling was first conducted for completely elastic response with comparison to analytical solutions. The analytical solution calculates the indentation depth considering the elastic properties of the sample (aluminum) and the indenter (tungsten carbide). The numerical modeling agrees exactly with the analytical solutions providing a verification of the model and the model setup using the different model components shown in Figure 3-18. After verification of the elastic modeling, a modeling of the actual indentation experiment on aluminum was conducted with very good agreement as shown in Figure 3-19.

Next simulation was done on a few shale samples as an initial evaluation of indentation tests using elasto-plasticity with the Mohr-Coulomb strength criterion. Figure 3-20 shows the comparison of experimental and numerical simulation results for dry Barnett sample. The simulation was conducted with E = 16.2 GPa, Poisson's ratio of 0.33, cohesion = 8.5 MPa, and coefficient of friction of 25°. The results are in good agreement for both loading and unloading, though some deviation during unloading below 2,000 gf.

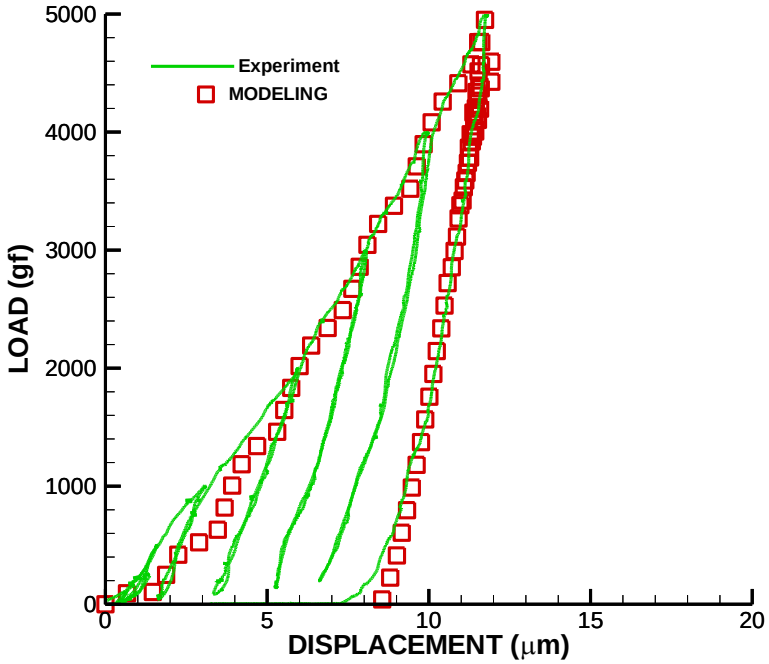

Figure 3-19. Comparison of modeling and experiment results of load-displacement curves for aluminum sample.

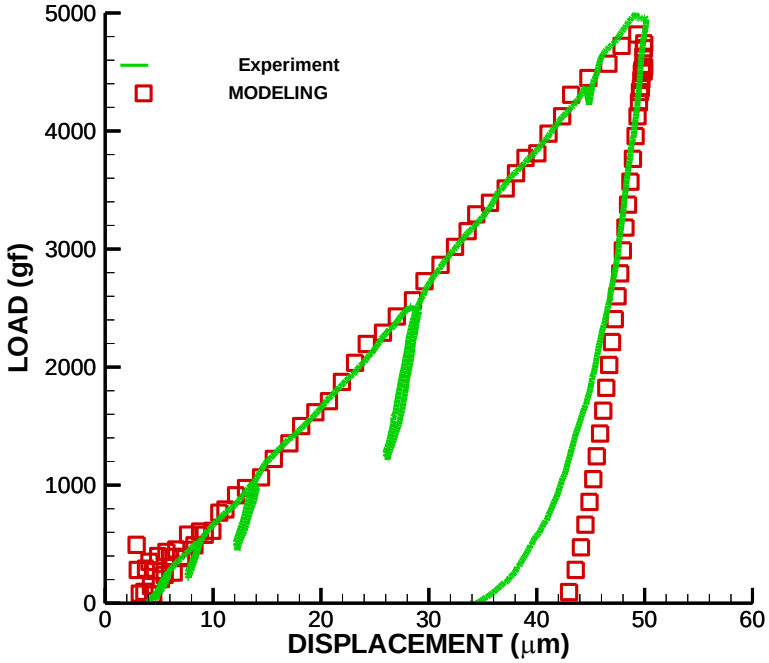

Figure 3-20. Comparison of modeling and experiment results of load-displacement curves for dry Barnett sample.

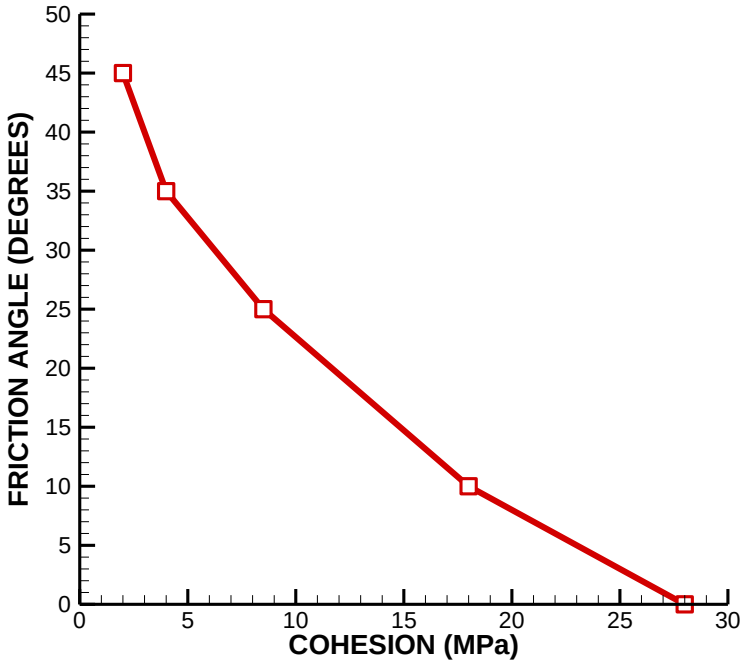

Figure 3-21. Combinations of friction angle and cohesion matching the laboratory load/displacement curve for dry Barnett shale sample.

The simulation with variable friction angle and cohesion showed that multiple values could be used to match total indentation displacement for a peak load of 2,000 gf (Figure 3-21). The simulations resulted in close to identical load/displacement curves similar to that shown in Figure 3-21. Therefore, unique pair of friction angle and cohesion values could not be determined from looking at the load/displacement curves.

Figure 3-22 presents the permanent indentation patter for the two end member of the friction angel and cohesion that matched the load/displacement curve. There is a significant difference in the indentation patter. In the case of low cohesion and high friction angle (C = 2 MPa, $\phi = 45°$), the permanent displacement is mostly vertical and there is a negligible heave at the indentation boundary (Figure 3-22a). In the case of high cohesion and low friction angle (C = 28 MPa, $\phi = 0°$) there is a significant permanent heave; is about 13 μm which is quite significant compared to the maximum permanent indentation depth of 44μm (Figure 3-22b). In the case of low cohesion and high friction angle (C = 2 MPa, $\phi = 45°$) the uniaxial compressive strength is only 9.6 MPa, whereas in the other extreme case of high cohesion and low friction angle (C = 28 MPa, $\phi = 0°$), the uniaxial compressive strength is 56 MPa.

In Q3 of FY2018, we made test simulations of creep deformation during indentation. In order to speed up the simulations, an axiymmetric model geometry were constructed (Figure 3-23). The axisymmetric model were constructed as a 3D piece-of-a-cake model, leading to a reduce number of elements and enhanced simulation speed.

The initial creep deformation tests on shales were relatively short-term (30 minutes) at a constant load corresponding to the maximum indentation load (1,000 gf for wet Barnett sample. 5,000 gf for all the other samples). All five shales exhibited some increases in the viscoelastic deformations after exposed to water. Barnett Shale samples exhibited by far the most rapid increases in the viscoelastic deformations for both dry and wet samples, indicating a strong impact of the large clay content.

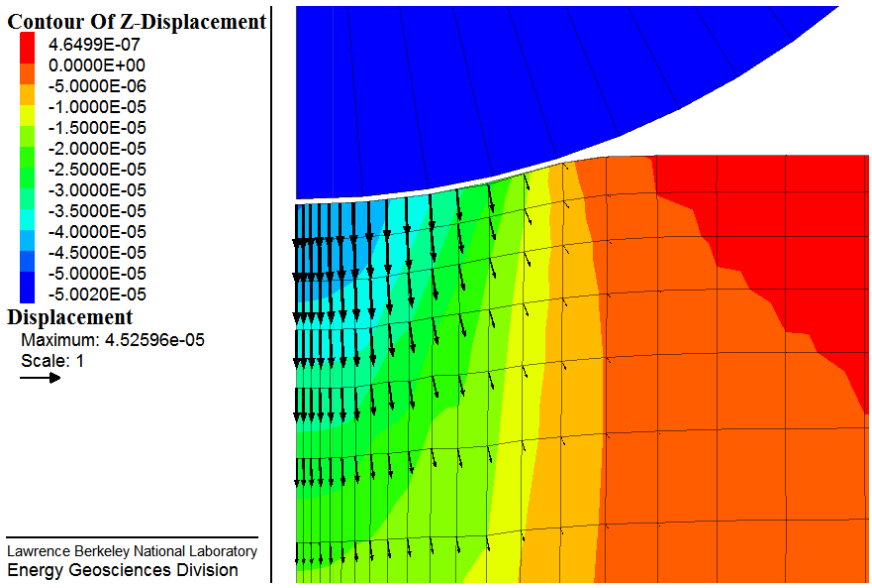

(a) Cohesion = 2 MPa, Friction angle = 45°

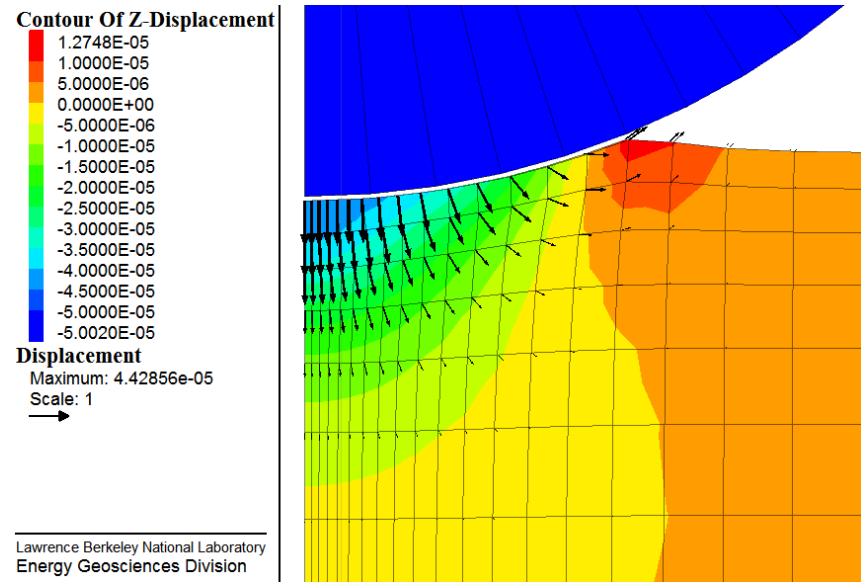

(b) Cohesion = 28 MPa, Friction angle = 0

Figure 3-22. Permanent indentation after unloading displayed by deformed mesh, vertical displacement contours and total displacement vectors for two end members of cohesion/friction angel pairs that matches the loading/displacement curves.

The creep simulations were conducted with Burger creep model, which we have employed in some previous generic grain-scale models of proppant embedment. The modeling of creep during indentation tests turned out to be challenging as we consider very small displacement and contact evolution, but at highly concentrated stress. The input parameters for the Burger model encompass both primary and secondary creep, and include the elastic bulk modulus, Kelvin shear modulus and viscosity, and Maxwell shear modulus and viscosity. We conducted a sensitivity analysis and calibration of model parameters to match the observed time-dependent response. The modeling shows that we should be able to match reasonable well any of the experiments have been conducted by calibrating the four creep parameters involved in the Burger model.

Figure 3-24 presents the experimental data for wet samples together with on overlay of two new creep simulation results (square symbols). One simulation broadly matches the more extensive deformations observed for Barnet 1&2 samples, whereas the other simulation broadly matches the observed deformations for Mancos & Eagleford samples. The creep parameters for these two simulations are listed in Table 3.1. Among those four parameters, the Maxwell viscosity is important for matching the slope of the latter part of the deformation curve supposedly related to secondary steady creep. The Kelvin shear modulus is important for matching the initial slope with its curvature affected by the Kelvin viscosity. However, although the Burger creep parameters could be back-calculated based on these experiments, a 30-min experiment might be too short to determine parameters for longer term creep behavior. If the experiments were kept longer, the back-calculated parameters might be different. Anyway, the modeling of the current 30-min creep experiments shows that indentation creep experiments can be useful and that creep parameters can be back-calculated. More studies and experiments, especially longer-term experiments would be recommended to further investigate the applicability of these creep indentation tests on predicting long-term proppant embedment.

Table 3.1 Burger model parameters used for modeling creep indentation tests.

	“Barnet 1&2”	“Manco & Eagleford”
Kelvin Shear Modulus (Pa)	7e9	8e10
Kelvin Viscosity (Pa·s)	2e12	1e13
Maxwell Shear Modulus (Pa)	7e12	3e12
Maxwell Viscosity (Pa·s)	5e12	7e13

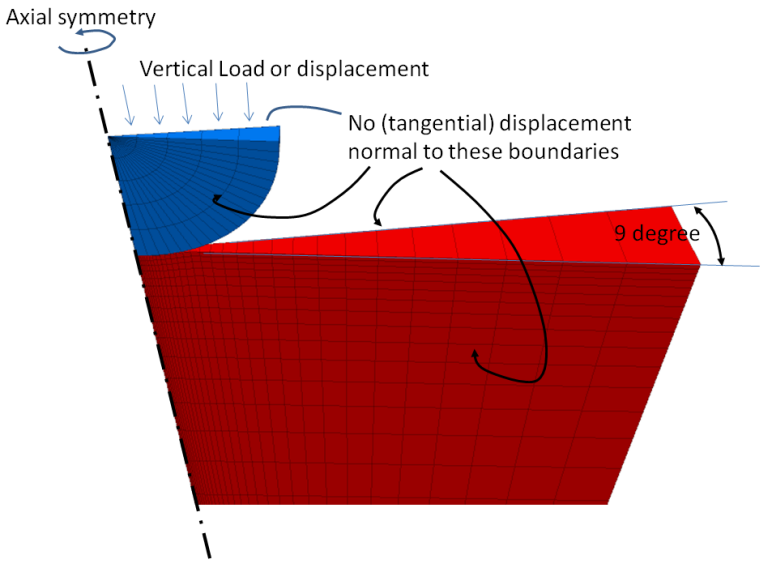

Figure 3-23. Axisymmetric model for numerical simulations of indentation tests.

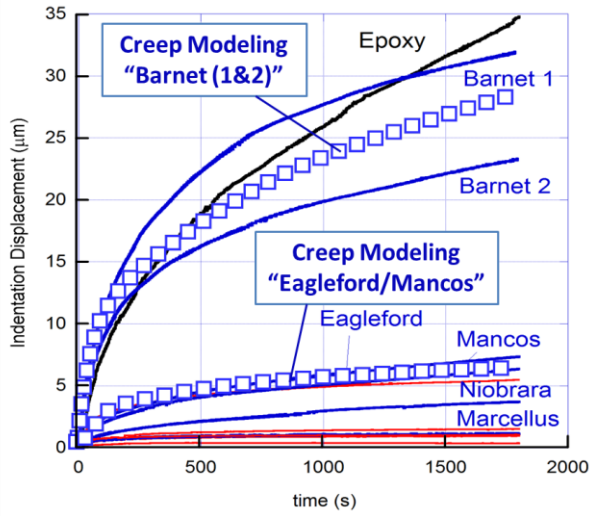

Figure 3-24. Axisymmetric model for numerical simulations of indentation tests.

2.2.4 Subtask 3.4 — Modeling fracture closure experiments I: w/o proppant

In this subtask, we model shale fracture compaction/permeability measurements conducted under Subtask 2.4 on an open, brine-filled fracture containing no proppant. The impact of the shale properties on the time-dependent deformation of the rock and the resulting changes in the fracture permeability was modeled.

Here we utilize the block-scale model developed and tested in FY2017, under Task 3.2 (Figure 3.15). In this particular experiment, a sample of Barnett shale (0.5 inch thick) with high clay content was compressed against a glass sample (0.5 inch thick) with a sandblasted surface. In the experiment, the glass sample is located below a Sapphire window, which is very stiff having a Young's modulus of more

than 5 times that of glass and shale. The model is mechanically fixed on top for vertical displacement and restricted from lateral displacements on the lateral boundary. In the model, the sample can be loaded from the bottom either by applying a constant stress or by applying a constant vertical velocity signifying a displacement controlled loading. In the simulation, the normal closure of the fracture and stress normal to the fractures is monitored.

In these simulations we were not representing the fact that the initial fracture aperture is much larger at the center. The topographic surface contour indicates that the surface is about 50 microns deeper in the center of the sandblasted glass surface. This implies that the center part of the fracture is likely initially completely open without any contacts, whereas the two surfaces are initially in mechanical contact at the periphery of the glass sample. With loading, it is expected that the center part will close relatively rapidly as until asperities of the glass surface comes into contact with the smooth shale surface. This is well illustrated in Figure 3-25 where the hydraulic aperture is initially about 50 microns, but then closes significantly during the first 250 psi of loading. Note that the hydraulic conducting aperture calculated from the flow rate by injection into the center borehole will be predominantly dependent on the fracture aperture just around the injection hole.

The results of loading and unloading simulations are shown in Figure 3-25 with comparison to the experimental data. The model simulations were conducted with a Young's modulus of the Barnett shale sample of 71 GPa, which is a value measured on cores samples as documented in previous quarterly reports. The same value of 71 GPa was applied to the glass sample, which is a reasonable value for glass. Fracture closure was modeled with Bandis joint model. The Bandis fracture closure model is defined by two parameters; the fracture normal stiffness at zero stress (kn0) and the maximum fracture closure, or maximum mechanical aperture, Bmax. Here we found reasonable match between modeling and experimental data using Kn0 = 101 GPa/m and Bmax = 35 microns for the loading, and Kn0 = 36 GPa/m and Bmax = 30 microns for the unloading.

A number of relevant observations can be made from comparison in Figure 3-25:

1) In general there is a reasonable good agreement regarding the hydraulic aperture for loads above 250 psi. Below 250 psi the experimental data is strongly affected by the initially non-uniform aperture distribution, which is not considered in the model. For the loading part there is a sign of increasing closure rate at high stress that is not captured for the current non-linear elastic fracture model.

2) The apparent mechanical aperture changes show reasonable good agreement for the loading, until a loading stress of about 1000 psi. For stress above 1000 psi, the experimental data shows a significant increase in deformation that deviates from the non-linear elastic behavior. This is probably caused by plastic deformations in stress-relieving metal (tin) shim at the interface between the sapphire window and the top flange of the equipment. This is consistent with the fact that the compressive strength of tin is about 1000 to 2000 psi.

3) During unloading the apparent mechanical aperture changes are in good agreement with experimental results, for loads above 250 psi. The slope here reflect elastic deformation in the shale and glass samples, which are both have a Young's modulus of 71 GPa in the model.

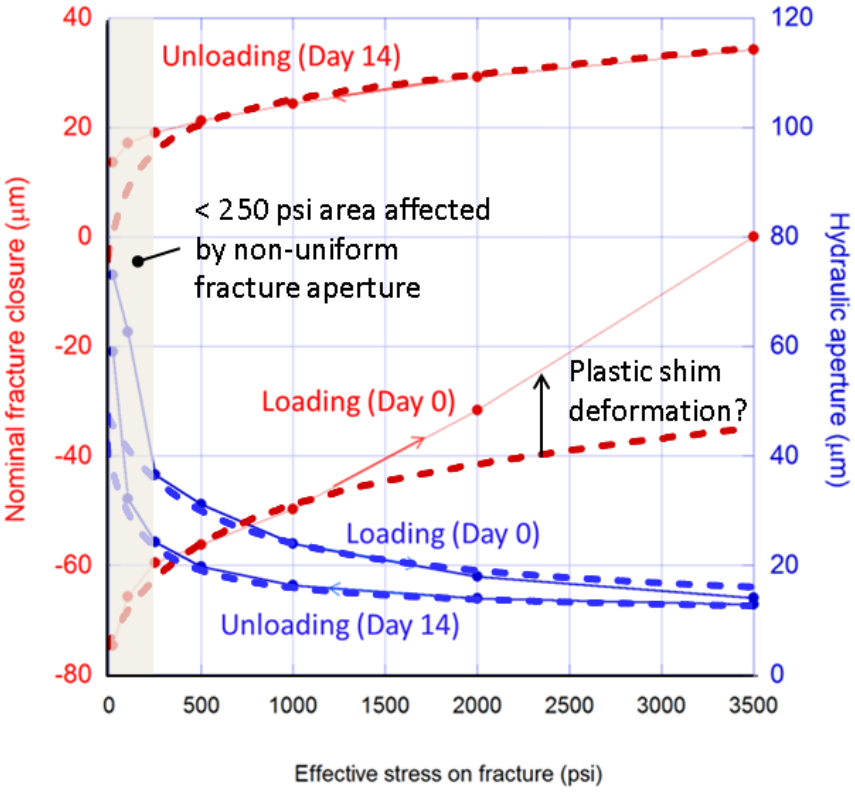

Figure 3-25. Comparison of numerical and experimental results for the experimental data in Figure 2-6 related to the first fracture compaction experiment without proppants. Numerical results are shown by thicker dashed lines. The grey area marks effective stress below 250 psi when the fracture is completely open at its center due to non-uniform fracture surface in the glass sample.

2.2.5 Subtask 3.5—Modeling fracture closure experiments ll: w/ proppant

In this subtask, we model shale fracture compaction/permeability measurements conducted under Subtask 2.5 on an open, brine-filled fracture containing proppants. The impact of the shale properties on the time-dependent deformation of the rock and the resulting changes in the fracture permeability were modeled.

Here we present modelling of a particular experiment for a flat, circular fracture surface in a Barnett Shale core with the fracture is perpendicular to the bedding. The proppant was monodispersed round silica sand with an average grain diameter ~1mm. In total 1.25 g of sand was dispersed on the fracture, which corresponds to about 901 grains. In our current model it is not possible to explicitly model all those 901 grains explicitly, but we are here utilizing the block-scale model developed and tested in FY2017, for Task 3.2, with the model geometry shown in Figure 3-15. A Burger creep model was used and the input parameters were adjusted until reasonable good match was obtained with the laboratory results (Figure 3-26). For this particular set of input parameters, the match with the longer-term creep deformations is good, while the early time modeling deviates somewhat from the laboratory results. The Burger creep model parameters used in this case are listed in Table 3-2. Some parameters are very

different from those used in the indentation test in Table 3-1. However, in the block scale model, the effects of the proppant embedment are implicitly accounted for so the effective parameters used should likely be different. A grain scale model of the experiment could also be conducted considering the effective load on one grain.

Table 3.2 Burger model parameters in a block-scale modeling of compaction experiment of a fracture filled with proppants.

Parameter (unit)	Value
Kelvin Shear Modulus (Pa)	1e9
Kelvin Viscosity (Pa·s)	5e13
Maxwell Shear Modulus (Pa)	7e8
Maxwell Viscosity (Pa·s)	5e17

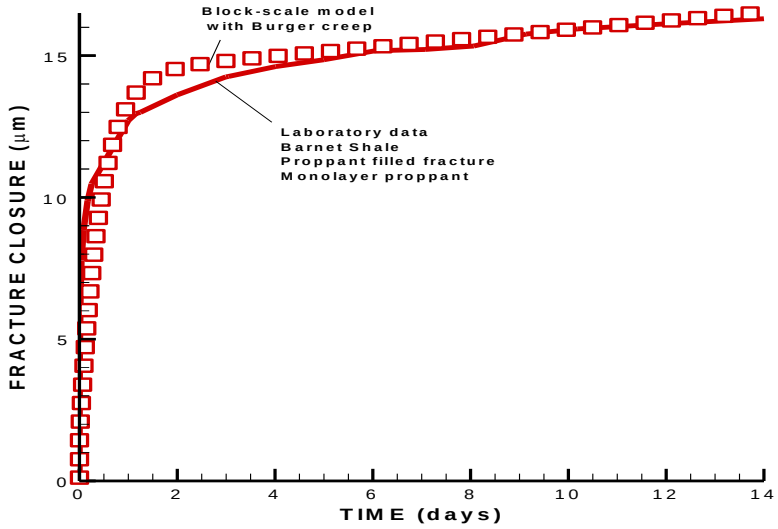

Figure 3-26. Results of numerical modeling of time-dependent fracture closure of a proppant filled fracture in wet Barnet shale.

2.2.6 Subtask 3.6—Modeling Gas/liquid transport experiment

This task was of the last quarter of project was intended for modeling near-fracture shale-matrix multiphase flow as evaluated from gas injection experiments under Subtask 2.6. These simulations would not involve any of the geomechanical fracture models developed under this project, but would involve multiphase flow simulations using the existing TOUGH2 code. The experiments were performed during last quarter of this project and eventually at the end of the quarter we found that there was not time enough to make high-quality useful simulations for interpretation of these experiments. Such modeling could be done in the future when there is a clear purpose defined for such modeling and sufficient time to complete them. The modeling efforts in the last quarter were instead focused on some of the other tasks such as the TOUGH-FLAC and TOUGH-RBSN grain-scale modeling, including multi proppant modeling with proppant crushing in harder clay and creep deformations in softer clay.

2.2.7 Final Remarks on the Numerical Modeling

Based on the numerical modeling in this project, the following final remarks are made:

1. Related to grain-scale modeling with TOUGH-FLAC, we found that the numerical modeling approach of using solid elements for shale and proppants and special interfaces for interaction between shale and proppants as available in FLAC3D, worked very well for modeling of proppant embedment in soft shale. Alternative approach of diskretizing rock, proppants and open fracture space with solid elements did not work as elements tend to become too distorted with large deformation. The approach with solid elements for shale and proppants and special interfaces for interaction between shale and proppants worked well for both elasto-plastic and creep deformation modeling.

2. Related to grain-scale modeling with TOUGH-RBSN, we demonstrated possible scenarios of proppant crushing and partial matrix failure in the parametric studies. The location of dominant failure is dependent on the relative strength contrast of proppant and matrix materials. With the new type of interface elements, more realistic representation of interaction between the proppant and matrix was facilitated. Especially in the simulations of multiple proppant grains embedded into the matrix, the extent of local failure differs from grain to grain, which might be attributed to the non-uniform distribution of the grains on the matrix block.

3. Indentation test modeling done with FLAC3D grain-scale approach turned out to be much more challenging than the previous multiple proppant embedment modeling. Very fine mesh diskretization was required for achieving accurate numerical solution of experiment of aluminum sample used for model validation due to very small deformations and contact changes for each loading cycle. Moreover, from the simulations of indentation tests, we found that the Mohr-Coulomb criterion could be adopted to parameterize material strength for modeling proppant embedment. There is a potential for determining a unique pair unique pair of Mohr-Coulomb strength parameters (friction angle and cohesion) if one can observe and quantify the degree of upheaving near the boundary of the indentation bowl.

4. Block-scale modeling was successful for modeling fracture closure with and without proppants. The elastic non-linear compression behavior as observed in laboratory tests could be captured in the block-scale model, and creep deformations of proppant filled fractures could be modeled as well using a Burger creep model. The creep parameters for a block-scale model of a proppant filled fracture were different from those used in the indentation tests. This is because in the block-scale model, the effects of the proppant embeddment are implicitly modeled so the effective parameters used should likely be different. Thus, there are questions on how to upscale from the indentation tests data macroscopic properties representing the behavior of a proppant filled fracture.

As final remark we can conclude that the numerical tools have been developed and demonstrated to be very useful for studies of proppant embedment in brittle and soft shales, including plastic and viscous mechanical behavior. These tools will in the future be used for further studies with the objective of contributing to the understanding of proppant filled fractures in soft shale that are barely producible, but could be enhanced with proper proppant treatment.

3. Publications and presentations (planned and submitted)

Nakagawa, S. and S. Borglin. 2019. Laboratory in-situ visualization of long-term fracture closure and proppant embedment in brittle and ductile shale samples, an abstract submitted to ARMA 2019 Meeting.

Kunhwi, K. and J. Rutqvist. 2019. Discrete lattice-based numerical modeling of proppant-matrix interaction in hydraulic fractures within brittle shale, an abstract submitted to ARMA 2019 Meeting.

Nakagawa, S., S. Borglin, T.J. Kneafsey, and M. Voltolini, Laboratory visualization of fracture closure and permeability loss in fractures in ductile shales with and without proppant, to be submitted to Int. J. Rock Mech.

Rutqvist, J. and K. Kim, Grain-scale modeling of proppant embedment and fracture closure in soft shale, to be submitted to JSPE.

4. Budget summary

Below is the spending for the entire period of the project for FY2017 and FY2018

FY17 Nakagawa/Rutqvist: Sustainability of Hydraulic Fracture Conductivity in Ductile and Expanding Shales

LBNL PID	Activity	Activity Name	FY17-18 FWP Funding	Oct	Nov	Dec	Jan	Feb	Mar	Apr	May	Jun	Jul	Aug	Sep	Total Spent to Date	Total Received	Amount remaining
102971	001	ES_Laboratory Hydraulic Frac	315,946	3,427	7,597	5,578	6,558	10,264	11,379	9,956	10,921	10,222	14,062	43,578	21,594	155,136	315,946	160,810
		Labor		3,427	6,542	4,906	6,542	8,637	10,644	9,579	8,076	10,078	11,993	29,891	21,263			
		Procurement			1,055	672	16	1,627	32	377	2,845	144	2,069	13,687	333			
									703	-					(2)			
102971	002	ES_Modeling Hydraulic Frac	206,571	6,905	6,625	6,626	11,126	9,762	6,336	2,336	8,489	4,374	4,582	14,276	16,053	97,490	206,571	109,081
		Labor		6,905	6,625	6,626	11,126	9,762	6,336	2,336	8,489	4,374	4,582	14,276	16,053			
		Procurement																
102971	003	ES_Admin Hydraulic Frac	57,483	-	530	530	265	292	739	-	-	-	417	2,331	387	5,491	57,483	51,992
		Labor			530	530	265	292		-			417	485	393			
		Travel/Procurement							739	-				1,846	(6)			

FY18

LBNL PID	Activity	Activity Name	Carryover from FY17	Oct	Nov	Dec	Jan	Feb	Mar	Apr	May	Jun	Jul	Aug	Sep	Oct	Total Spent to Date	Total Received	Amount remaining
102971	001	ES_Laboratory Hydraulic Frac	160,810	9,011	10,650	10,052	11,194	10,905	9,626	17,949	15,111	11,093	11,764	17,912	25,543	-	160,810	160,810	-
		Labor		7,841	10,354	9,968	9,620	10,006	9,626	15,361	14,045	8,652	11,533	17,912	25,582				
		Procurement		1,170	296	84	1,574	899	-	2,588	1,066	2,441	231		(39)				
102971	002	ES_Modeling Hydraulic Frac	109,081	2,134	9,155	7,154	4,307	7,511	6,829	4,716	4,307	2,236	30,449	26,155	4,128	-	109,081	109,081	-
		Labor		2,134	9,155	7,154	4,307	7,511	6,829	4,716	4,307	2,236	30,449	26,155	4,128				
		Procurement																	
102971	003	ES_Admin Hydraulic Frac	51,992	-	1,115	298	-	-	-	5,746	545	9,278	3,707	29,172	1,097	1,029	51,987	51,992	5
		Labor		-	1,115	298				5,746	545	9,278	3,707	2,094	(117)	1,029			
		Travel/Procurement												27,078	1,214				

5. References

Griggs, D. (1939).” Creep of rocks,” *J. Geol.,* **47,** 225–251. Doi: 10.1086/624775

Hay, J., C.H. Sondergeld (2010) “Mechanical testing of shale by instrumented indentation,” Agilent Technologies Application Note.

Hornby, B.E. (1998) “Experimental laboratory determination of the dynamic elastic properties of wet, drained shales,” *J. Geophys. Res*., **103**(B12), 29945-29964, doi.org/10.1029/97JB02380

Knight, J., C. Fandrich, C. Lau, H. Jaeger, and S. Nagel, S. (1995) “Densitrelaxation in a vibrated granular material,” *Phys. Rev. E,* **51,** 3957–3963.

Lo, T.-W., K. B. Coyner, and M. N. Toksöz (1986) ”Experimental determination of elastic anisotropy of Berea sandstone, Chicopee shale, and Chelmsford granite.” *GEOPHYSICS*, **51**(1), 164-171. , doi.org/10.1190/1.1442029

Oliver, W.C. and G.M. Pharr (2004) “Review: Measurement of hardness and elastic modulus by instrumented indentation: Advances in understanding and refinements to methodology,” *J. Mater. Res.,* **19**(1), 3.20.

Snieder, R., C. Sens-Schönfelder, and R. Wu (2017) “The time dependence of rock healing as a universal relaxation process, a tutorial,” *Geophys. J. Int.* (2017) **208,** 1–9 doi: 10.1093/gji/ggw377

Ten Cate, J. (2011) ”Slow dynamics of earth materials: an experimental overview,” *Pure appl. Geoph.,* **168,** 2211–2219.

Thomsen, L. (1986). ”Weak elastic anisotropy.” *GEOPHYSICS*, **51**(10), 1954-1966, doi.org/10.1190/1.1442051